Mechanics of mitotic spindle poles and polymerization dynamics of microtubules

by

Blake D. Charlebois

A dissertation submitted in partial fulfillment
of the requirements for the degree of
Doctor of Philosophy
(Biomedical Engineering)
in The University of Michigan
2011

Doctoral Committee:

Professor Alan J. Hunt, Chair
Professor Edgar Meyhöfer
Associate Professor David S. Sept
Associate Professor Kristen J. Verhey
Assistant Professor Sivaraj Sivaramakrishnan

To my parents and grandparents,

who were my first teachers

in matters academic and otherwise.

ACKNOWLEDGEMENTS

It is difficult to adequately express my thanks to the many people involved, directly or indirectly, in the completion of this work.

I first thank my advisor, Alan Hunt, for his support, patience, insightful intellectual contributions, and persistent effort, none of which can be overstated.

I am tremendously fortunate to have a committee with extensive depth and breadth of knowledge within and outside my field of study. Each committee member is encouraging, engaged, and generous with his or her time and advice. I recall specific enlightening interactions with Edgar Meyhöfer that stimulated my excitement about science, and I note that I have indirectly benefited from his mentorship of Trey Schek and Damon Hoff.

I have benefited a great deal from early mentorship by Henry (Trey) Schek and ongoing mentorship from J. Damon Hoff. Damon is consistently generous with his time, intellect, and friendship, assisting me and others in the department with a wide range of problems from the intellectually or emotionally overwhelming to the mundane. I suspect he is also the fastest aliquoter in the midwest. I thank members of the Hunt lab, past and present, for their support and assistance including Kevin, David, Jeff, Jun, Ran, Seth, Aghapi, John, Ophelia, and Hong. I also thank Meyhöfer lab members Troy and Neha, as well as Ajit Joglekar, for their encouragement. I acknowledge my M.A.Sc. advisor, C. Ross Ethier, who was highly influential in my intellectual development, as was his student Khosro Shahbazi. Department staff, including Chuck, Maria, and Dana, have been remarkably patient and helpful.

I thank my collaborators for their extensive efforts. Chapter III is the product of a collaboration that resulted in a shared first-authorship publication [Charlebois, Kollu, Schek, Compton, and Hunt, 2011]. Swapna Kollu and I attempted to divide the required effort equally between us, working side by side in many stages of the work and allocating some tasks based on expertise. I therefore operated the optical tweezers, performed data analysis, and drafted an initial typescript in which data interpretation required expertise on mechanics and on the instrument used. Chapter VI is the product of a collaboration that resulted in a paper on which I am second author [Gardner, Charlebois, Jánosi, Howard, Hunt, and Odde, 2011]. The data I collected using the optical tweezers assay of Chapter V confirmed our hypothesis, which had been suggested by computational results Melissa Gardner obtained while working in the Odde lab, and which Melissa further confirmed with TIRF microscopy after joining the Howard lab. Figures shown in Chapter VI were prepared by Melissa, but for those corresponding to the data I collected I performed independent parallel analysis.

I am grateful my wonderfully supportive partner Areeta, who helps me see the forest for the trees. My life would not be right without her.

I also have the good fortune of having a supportive family whose company I've always very much enjoyed, including my Father, late Mother, grandparents (one of whom taught me about polar and azimuthal angles in my youth, though I appreciated this only much later), sister, aunts, uncles, cousins, and their significant others. Many friends deserve my thanks for their support and for tolerating my disappearances into the library or lab, and I will not try to name them here for fear of forgetting even one.

The present work was written using TEXnicCenter, JabRef, and the the LaTeX template from the University of Michigan AOSS website, all of which have been made available by their authors free of charge.

TABLE OF CONTENTS

LIST OF FIGURES

Figure

LIST OF TABLES

Table

LIST OF APPENDICES

Appendix

ABSTRACT

Mechanics of mitotic spindle poles and polymerization dynamics of microtubules

by

Blake D. Charlebois

Chair: Alan J. Hunt

During cell division, chromosomes must faithfully segregate to maintain genome integrity, and this dynamic mechanical process is driven by the macromolecular machinery of the mitotic spindle. However, little is known about spindle mechanics. For example, spindle microtubules are organized by numerous cross-linking proteins yet the mechanical properties of those cross-links remain unexplored. To examine the mechanical properties of microtubule cross-links we applied optical trapping to mitotic asters that form in mammalian mitotic extracts. These asters are foci of microtubules, motors, and microtubule-associated proteins that reflect many of the functional properties of spindle poles and represent centrosome-independent spindle-pole analogs. We observed bidirectional motor-driven microtubule movements, showing that microtubule linkages within asters are remarkably compliant (mean stiffness 0.025 pN/nm) and mediated by only a handful of cross-links. Depleting the motor Eg5 reduced this stiffness, indicating that Eg5 contributes to the mechanical properties of microtubule asters in a manner consistent with its localization to spindle poles in cells. We propose that compliant linkages among microtubules provide a mechanical architecture capable of accommodating microtubule movements and distributing

force among microtubules without loss of pole integrity—a mechanical paradigm that may be important throughout the spindle.

Microtubule assembly and disassembly are vital for many fundamental cellular processes. Our current understanding of microtubule assembly kinetics is based on a one-dimensional assembly model, which assumes identical energetics for subunits exchanging at the tip. In this model, the subunit disassociation rate from a microtubule tip is independent of free subunit concentration. Using total-internal-reflection fluorescence (TIRF) microscopy and an optical tweezers assay to measure *in vitro* microtubule assembly with nanometer resolution, we find that the subunit dissociation rate from a microtubule tip increases at higher free subunit concentrations. This is because, as predicted by Hill, there is a shift in microtubule tip structure from relatively blunt at low free subunit concentrations to relatively tapered at high concentrations, which we confirmed experimentally by TIRF microscopy. Because both the association and the dissociation rates increase with free subunit concentrations, we find that the kinetics of microtubule assembly are an order of magnitude faster than currently estimated in the literature.

CHAPTER I

Introduction

The present work can be divided into chapters on mitosis (II and III) and chapters on microtubule polymerization (IV to VI). The present chapter provides background and motivation with a brief introduction to the cytoskeleton, microtubules, and mitosis, but with most emphasis on microtubules due to their relevance to all chapters. Additional background is left to later chapters (Chapter II for mitosis, Chapter IV for microtubules). The present chapter concludes with a summary of the contents of the present work.

1.1 The cytoskeleton

Animal cells may contain three types of cytoskeletal fibers: F-actin (microfilaments), intermediate filaments, and microtubules [Lodish et al., 2004]. These fibers are long, thin, unbranched protein polymers, and they interact with proteins that affect their polymerization dynamics, cross-link them into various structures (e.g., Fig. 1.1), and exert force upon them. Together, these fibers and associated proteins are a major determinant of cell mechanics and morphology [Howard, 2001].

Cross-linking proteins commonly arrange cytoskeletal fibers into bundles or into two- or three-dimensional networks with various cellular localizations. For instance, in the mitotic spindle microtubles are cross-linked into a structure that orchestrates

chromosome movement (Chapter II).

Of the three types of cytoskeletal fibers, intermediate filaments are perhaps the least well understood. They are encoded by numerous genes with complex expression patterns [reviewed by Herrmann et al., 2007], and they differ markedly in many respects from F-actin and microtubules. F-actin and microtubules have several similarities: they are composed of highly conserved globular subunits; they have a fast-growing plus end and a slow-growing minus end (they are "polar"); they are nucleoside triphosphatases; they are often highly dynamic; they generate force by polymerization; and they are substrates against which molecular motors exert force [Howard, 2001; Lodish et al., 2004].

1.2 Microtubules

Microtubules are key structural elements in mitosis, and microtubule assembly is crucial to mitosis and other cellular processes (e.g., see Fig. 1.2). The structures of these tube-shaped polymers and also of the subunits from which they are composed are intimately related to their mechanical and polymerization properties and, in turn, their biological functions.

1.2.1 Microtubule structure and function

Microtubules [Amos, 2004; Amos and Schlieper, 2005; Desai and Mitchison, 1997; Howard and Hyman, 2003, 2009] form by the assembly into a tube of 8-nm long $\alpha\beta$-tubulin heterodimers (Fig. 1.3), referred to throughout this thesis as subunits. α and β tubulins have roughly 50% identical sequences and are roughly 50 kDa each [Desai and Mitchison, 1997]. Tubulin isoforms in addition to α and β have been identified, including several relevant to centrioles [Pearson and Winey, 2009], as well as γ-tubulin, which is implicated in microtubule nucleation by centrosomes.

Microtubule functions include providing structural support to the cell and or-

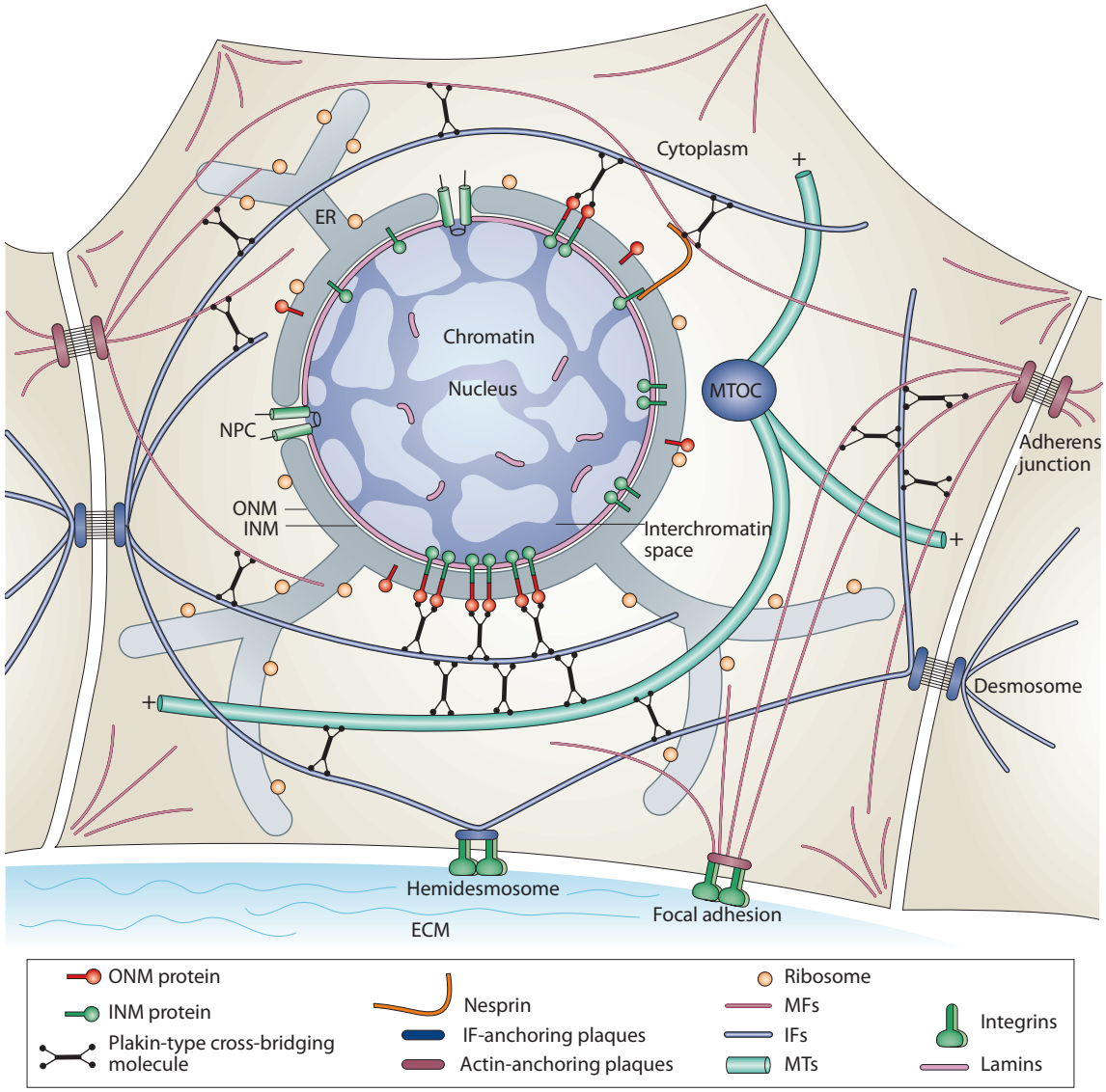

Figure 1.1: Interconnection of cytoskeletal fibers. In this hypothetical epithelial cell, F-actin (MFs), microtubules (MTs) and intermediate filaments (IFs) are interconnected by plakins and are connected to other cells, the extracellular matrix (ECM), and outer nuclear membrane (ONM) and inner nuclear membrane (INM) proteins. Also shown are nuclear pore complexes (NPCs) connected to lamins. Figure from Herrmann et al. [2007].

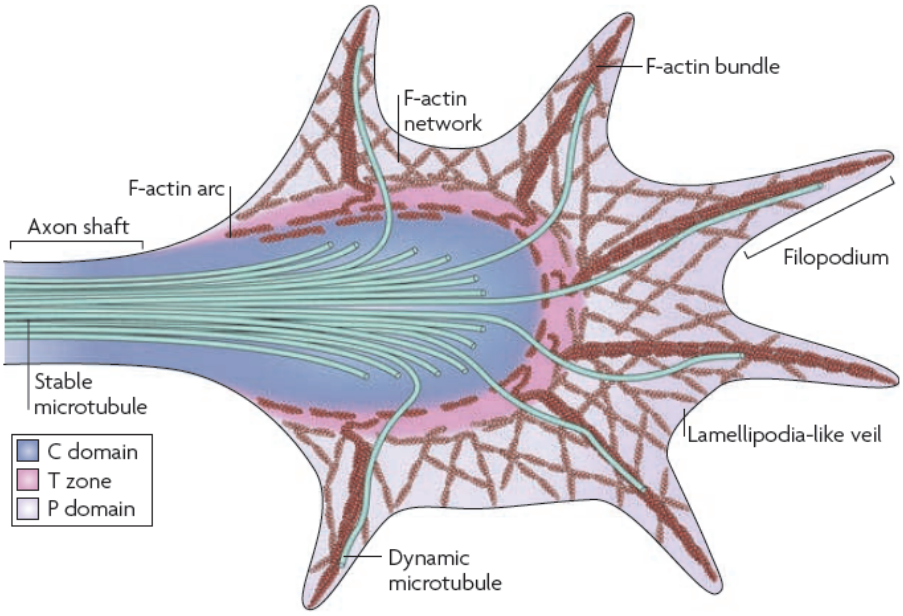

Figure 1.2: F-actin and microtubules in growth cones. At the tip of a growing axon, the growth cone, based on several spatial cues, guides growth. Retrograde movement of F-actin is believed to be driven by actomyosin-generated force in the T (transition) zone (F-actin arcs) and polymerization of actin in the P (peripheral) domain. In the P domain, F-actin bundles and networks are present in, respectively, filopodia and lamellipodia-like veils. Dynamic microtubules are present in the P domain, usually along F-actin bundles. In the C (central) domain, stable microtubules extend from the axon shaft, and various other components are present. P-domain microtubules are thought to act as "guidance sensors" that affect signalling components, and C-domain microtubules are important to advance the growth cone [reviewed by Lowery and Vactor, 2009]. Figure from Lowery and Vactor [2009]

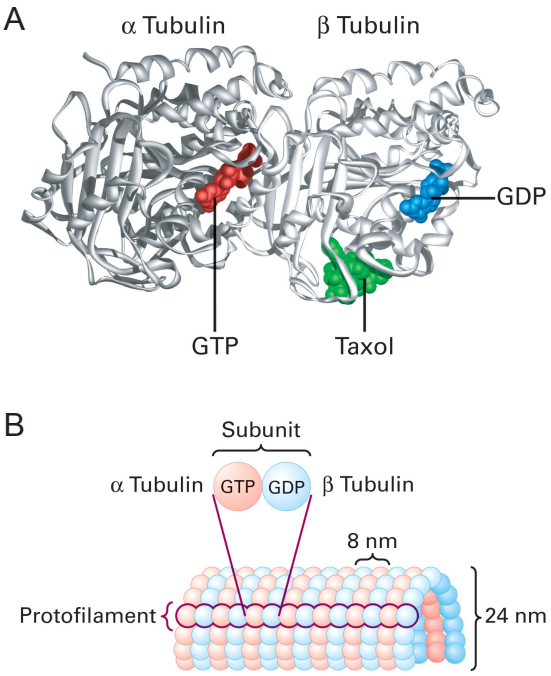

Figure 1.3: Microtubules assemble from heterodimeric $\alpha\beta$-tubulin subunits. (A) The tubulin heterodimer binds guanine nucleotides. (B) Subunits stacked end to end (α-β-α-β...) constitute a protofilament, and typically 13 protofilaments constitute a microtubule. The ends of the microtubule with α- and β-tubulins exposed are respectively termed the minus and plus ends. Figure from Lodish et al. [2004].

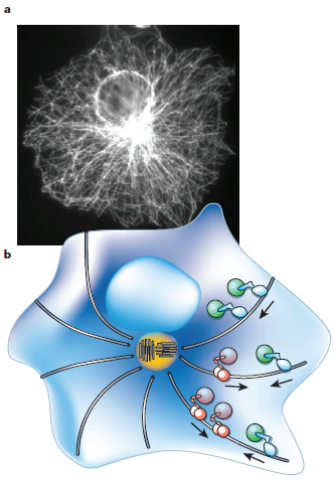

Figure 1.4: Microtubules in an interphase cell. (a) Microtubules in an interphase cell labeled by antibody-based staining. (b) Prototypical microtubule organization and microtubule-based intracellular transport. The centrosome (yellow) is the microtubule organizing center (MTOC). It contains centrioles, which are formed from specialized microtubules. It also nucleates microtubules with their plus ends oriented toward the cell periphery. Molecular motors, either plus- or minus-directed, transport vescicles. Figure from Howard and Hyman [2003].

ganelles and providing the tracks on which molecular motors walk for intracellular transport (Fig. 1.4). Microtubules are enriched in neural tissue, and play important roles in the function of growth cones (Fig. 1.2). Among the best known functions of microtubles is orchestrating movement of chromosomes in mitotis and meiosis (Chapter II), in which microtubules arranged in a fusiform array grow and shrink in order to capture chromosomes, arrange them at the metaphase plate, and pull them to opposite ends of the cell during anaphase. This process is fundamental to life and its misregulation is implicated in cancer.

The microtubule can be viewed as a motor, as it stores the energy of GTP hydrolysis in its lattice and can use this stored energy to perform work [Grishchuk et al., 2005]. In addition, two types of molecular motor, dynein and kinesin, use the energy of ATP hydrolysis to exert force on microtubules. Axonemal dynein brings about the beating of cilia and flagella, while cytoplasmic dynein, usually if not always bound to

dynactin, has many functions. Dynactin is a megadalton multi- (>20) subunit protein complex, and this composition determines the properties of dynein [Schroer, 2004]. The kinesin superfamily family includes motors that can walk along microtubules for varying distances, generally toward the plus or minus end, against an opposing load [Miki et al., 2005]. This superfamily also includes members that can depolymerize microtubules at their ends after either diffusing or walking along the lattice. Other microtubule-associated proteins act as polymerases [Howard and Hyman, 2007].

1.2.2 GTP hydrolysis and dynamic instability

α-tubulin contains GTP in its "N-site" where exchange and hydrolysis rates are taken to be negligible. In contrast, β-tubulin contains GTP or GDP in an exchangeable site (E-site) in which hydrolysis occurs. Microtubule polymerization occurs by addition of tubulin subunits containing GTP in the E-site (GTP-tubulin), and upon incorporation into the microtubule the rate of E-site GTP hydrolysis increases, so that the lattice contains predominantly GDP-tubulin.

Microtubules exhibit an unusual behavior, termed dynamic instability, in which they alternate between phases of steady growth and rapid shortening. Transition from growth to rapid shortening is termed catastrophe, while transition from rapid shortening to growth is termed rescue. In the textbook explanation for this phenomenon, GTP-tubulin subunits add to the end of the microtubule (Fig. 1.5). Once incorporated into the microtubule, the GTP contained in the β-tubulin can be hydrolyzed to GDP, so that subunits far from the tip are predominantly GDP-tubulin. The GDP-tubulin lattice is unstable, but the GTP-tubulin at the tip stabilizes the microtubule. Catastrophe occurs when the cap of GTP-tubulin at the tip is lost. [Desai and Mitchison, 1997; Lodish et al., 2004; Mitchison and Kirschner, 1984] The instability of the GDP-tubulin lattice is thought to result from GDP-tubulin preferring a curved conformation, so that it must be strained while in the lattice. Dynamic

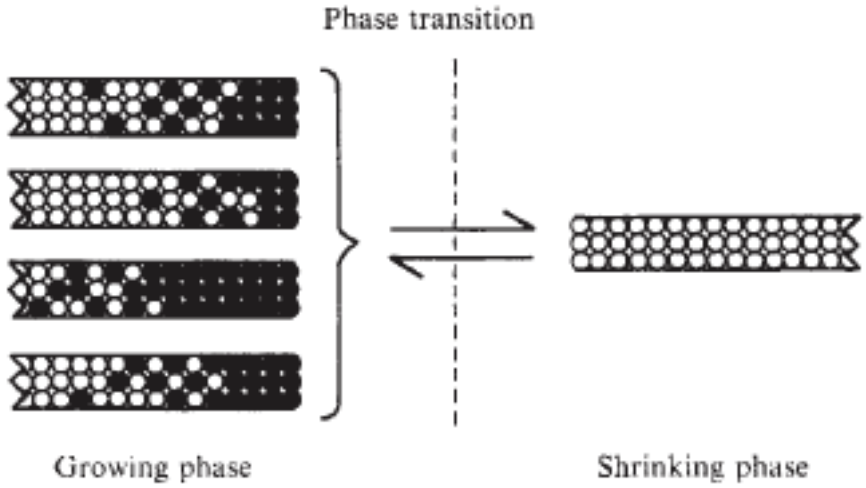

Figure 1.5: The GTP cap. In the growth phase (left), the microtubule tip has a stabilizing cap of GTP-tubulin (black) while much of the bulk of the lattice is composed of GDP-tubulin (white). Addition of new GTP-tubulin from solution maintains this cap, while hydrolysis of GTP by tubulin in the lattice shortens the cap. Loss of the cap triggers a phase transition (catastrophe) to rapid shortening (right). Figure from the original proposal of the GTP cap hypothesis by Mitchison and Kirschner [1984].

instability allows the cell to bring about rapid microtubule length changes as needed.

1.2.3 Growth-phase polymerization

Transitions between growth and shortening phases, as well as the effects of microtubule-associated proteins, are determined in part by growth-phase microtubule assembly. The established view is that this assembly is occurs by association of tubulin at a rate proportional to the free tubulin concentration, with tubulin dissociation occurring at a constant rate. Association has been estimated to be well below the diffusion limited rate, while dissociation has been estimated to be much slower than association in the practical range of tubulin concentrations. As detailed in section 4.3 (p. 61), there are several reasons to believe this established view should be revised: briefly, net microtubule growth rate is far more variable than the established view would pre-

dict, and this may be explained by association and dissociation occurring far faster than is currently believed [Howard and Hyman, 2009], but this would require dissociation rate to increase with tubulin concentration; theory predicts that dissociation rate may, depending on the magnitude of the lateral interaction energy, increase with tubulin concentration due to increased incidence of tubulin subunits at the tip having less than two stabilizing lateral neighbors [Hill, 1986]; and cryoelectron microscopy data indicate that microtubule tips that are tapered, and therefore have more unstable subunits, are favored with increasing tubulin concentration [Chrétien et al., 1995]. Chapter VI tests the hypotheses that subunit exchange at the tip is far faster than has been appreciated and that the dissociation rate increases with free tubulin concentration.

1.3 Mitosis

Mitosis is a precisely orchestrated process in which dynamic microtubules capture chromosomes and the sister chromatids of each chromosome are pulled to opposite ends of a dividing cell (further reviewed in Chapter II). The forces driving chromosome movement are transmitted via microtubules, which are arranged into a structure termed the mitotic spindle in which microtubule minus ends converge at each of the two spindle poles. The connection of these minus ends is dynamic; microtubules exhibit poleward flux, which requires that they depolymerize at their minus ends while maintaining load-bearing connections to the pole. Despite the mechanical nature of mitosis, we have relatively little quantitative data on the mechanics of mitosis, particularly on the connection of microtubules to the pole. This motivates Chapter III, which investigates the mechanical connection of microtubules in an analog of the mitotic spindle pole.

1.4 Summary of dissertation contents

Chapter II briefly reviews mitosis literature, focusing on the mechanics of mitosis. Chapter III is a study of the mechanics of mitotic spindle pole analogs termed mitotic asters.

Chapter IV briefly reviews microtubule literature. Chapter V describes an optical-tweezers based assay developed by Henry T. Schek III for measuring microtubule length changes with high spatiotemporal resolution. Chapter VI combines the assay of Chapter V with a light-microscopy assay and simulations to obtain evidence against the classical model for microtubule growth.

Chapter VII summarizes the conclusions of this thesis and recommends future work.

CHAPTER II

Background: Mitosis

This chapter* reviews mitosis with an emphasis on the mechanics of the mitotic spindle.

2.1 Introduction

Mitosis requires that genetic material be segregated to the two daughter cells with consistent fidelity. Incorrect segregation may result in cell death or in diseases such as cancer. Correct segregation is achieved by a precisely orchestrated multi-phase process.

Mitosis is normally divided into several phases (Figs. 2.1 and 2.2). In prophase, centrosomes separate and chromosomes begin to condense. In prometaphase, the nuclear envelope breaks down, the spindle microtubules are present in what was the nucleus, and the chromosomes have fully condensed. At metaphase, chromosomes move to the equatorial plane or metaphase plate. At anaphase, the sister chromatids separate in synchrony to opposite poles (anaphase A) and the distance between the poles increases (anaphase B). (Upon separation, the sister chromatids are considered chromosomes.) Telophase is marked by the return of interphase features: spindle

*Portions of this chapter are taken verbatim my qualifying exam written proposal and from Charlebois et al. [2011].

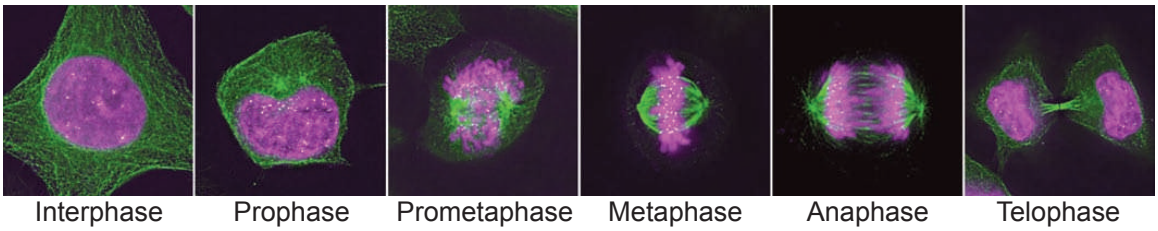

Figure 2.1: Fluorescence images of the phases of mitosis. Microtubules (green) and DNA (purple) are stained in a dividing HeLa cell proceeding (left to right) from interphase to prophase, prometaphase, metaphase, anaphase, and telophase. Figure adapted from Yanagida [2009]

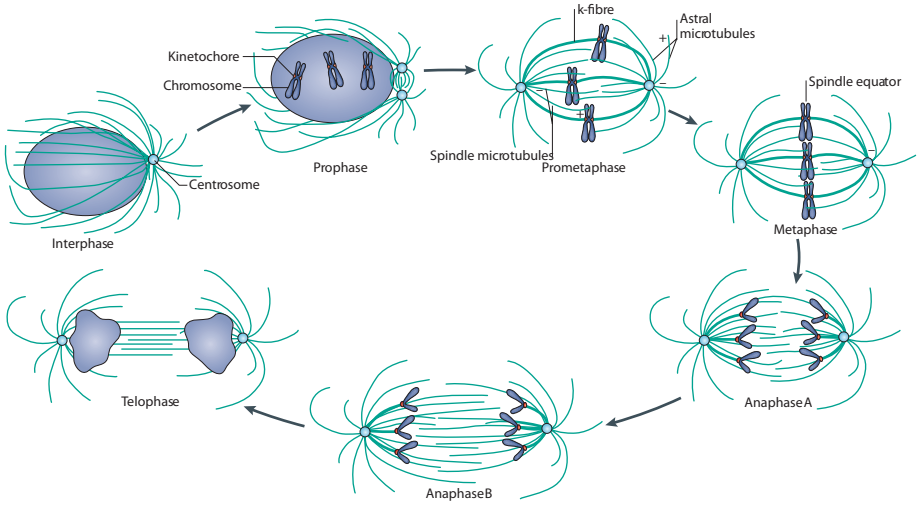

Figure 2.2: Schematic of the phases of mitosis. Figure from Walczak et al. [2010]

disassembly, decondensation of chromosomes, and reformation of the nuclear envelope. Cytokinesis is the final division into two daughter cells with separate cytoplasm. [Lodish et al., 2004] (Final separation of cytoplasm, termed midbody abscission, may be considered separate from near division of the daughter cells, cytokinesis [Walczak et al., 2010].)

2.2 The spindle

The central purpose of mitosis is segregation of chromosomes, and the mechanical apparatus responsible for this segregation is the spindle, a macromolecular ensemble

of microtubules, motors, and nonmotor microtubule-associated proteins. Spindle microtubules extend from the two opposing spindle poles toward the metaphase plate, forming a highly dynamic structure in which microtubule polymerization dynamics and motor-generated forces orchestrate the movement of chromosomes. Spindle microtubules must cause chromosomes to congress at the metaphase plate with pairs of sister kinetochores attached to opposite poles (amphitelic attachment) in order to satisfy the spindle assembly checkpoint. In anaphase, spindle microtubules must pull sister chromatids to opposing poles.

2.2.1 Dynamic phenomena and spindle forces

Spindle forces result in dynamic phenomena including chromosome directional instability, in which chromosomes move at roughly constant speed in alternating directions with abrupt transitions [Skibbens et al., 1993]; poleward microtubule flux, in which spindle microtubules depolymerize at their minus ends and translate poleward, which implies microtubules must be detached from their nucleation sites [Mitchison, 1989]; and kinetochore capture by microtubules.

The spindle can exert force on a chromosome via a kinetochore fiber (k-fiber; a bundle of microtubules) that connects end-on to a kinetochore. Lateral kinetochore-microtubule interactions are also implicated in chromosome movement. Furthermore, interaction between chromosome arms and non-kinetochore microtubules causes polar-ejection forces, which push chromosome arms away from the poles [Walczak et al., 2010]. Microtubule polymerization and depolymerization forces, as well as motor-mediated forces (summarized by Loughlin et al. [2008]), are implicated in force generation.

Spindle poles are mechanical hubs; they can be connected directly or indirectly to each other, to chromosome arms and kinetochores, and to the cell cortex via microtubules, cross-linkers, and molecular motors [reviews include Cheeseman and Desai,

2008; Gatlin and Bloom, 2010; Mogilner and Craig, 2010]. At the cell cortex, cytoplasmic dynein is implicated in exerting force on astral microtubules to control spindle position, which is important for asymmetric division (additional microtubule-cortex interactions have been demonstrated in yeast) [reviewed by Moore and Cooper, 2010; Siller and Doe, 2009]. At the chromosome, spindle microtubules can interact with chromosome arms, generating polar ejection forces, and also connect to a kinetochore, which is composed of an array of proteins including MAPs and molecular motors [Cheeseman and Desai, 2008]. Near the metaphase plate, interdigitating antiparallel microtubules emanating from opposite poles experience forces due to molecular motors such as kinesin-5 (Eg5), which is implicated in separation of spindle poles and, in some systems, polward flux [e.g., reviewed by Ferenz et al., 2010; Gatlin and Bloom, 2010]. Molecular motors, including kinesin-5, are also present at poles [Ferenz et al., 2010]. Minus-directed motors dynein and kinesin-14 (HSET, Ncd) are implicated in focusing microtubules into a pole [Gatlin and Bloom, 2010].

2.2.2 Centrosomal and acentrosomal spindle formation pathways

Chapter III investigates a model system representing the acentrosomal pathway. A discussion of these pathways is therefore required.

> "The chromosomal spindle fiber which is based on the kinetochore has naturally been regarded as the spindle element most intimately involved in chromosomal movement. Hence from the first, it has been the subject of special attention, and many hypotheses concerning its nature and origin have been broached, discarded, and advanced anew.
>
> ...hypotheses simmer down to three: the chromosomal fibers arise from the pole, grow toward the chromosome and connect with it; or they arise from the chromosome and grow toward the pole; or they are formed as the result of an interaction between the pole and the chromosome." Schrader

[1953]

Explaining formation of the canonical (centrosomal) spindle is the search and capture model [Kirschner and Mitchison, 1986], in which microtubules nucleated by the centrosome grow and shrink, exploring space randomly until they encounter and attach stably to a kinetochore. Centrosomes were thus long believed to be "responsible for mitotic-spindle assembly" [Wadsworth et al., 2004], while spindle assembly in acentrosomal animal cells, which involves nucleation of microtubules at chromosomes and organization of microtubules by molecular motors and cross-linkers [O'Connell and Khodjakov, 2007], was viewed as an anomaly [Gadde and Heald, 2004].

Early calculations concluded that the search and capture model could predict physiological chromosome alignment times [Hill, 1985; Holy and Leibler, 1994]. However, modeling using more realistic geometry and number of chromosomes [Wollman et al., 2005] determined that the search and capture approach alone does not predict chromosome congression on timescales as short as those observed experimentally, particularly in large cells. Acceleration of spindle formation is required, possibly by the acentrosomal pathway of spindle formation, in which microtubules nucleated at chromosomes become focused into a spindle. Underscoring the importance of this pathway, several microtubule cross-linkers and motors that organize and anchor microtubules during acentrosomal cell division are also important in centrosomal cell division [Compton, 1998]. Furthermore, elements of acentrosomal spindle assembly occur in PtK (potoroo) [Khodjakov et al., 2003] and Drosophila S2 [Maiato et al., 2004] cells, both of which have centrosomes. The acentrosomal pathway presumably compensated for the absence of centrosomes in a study in which *Drosophila* larvae lacking centrosomes developed into morphologically normal adults, though they died shortly after birth, apparently due not to mitotic errors but to lack of cilia [Basto et al., 2006]. At minimum, this study casts doubt on the importance of centrosomes to mitosis. Evidence consistent with the importance of the acentrosomal pathway has

been extensively reviewed [e.g., Compton, 1998; Gadde and Heald, 2004; O'Connell and Khodjakov, 2007; Rieder, 2005; Wadsworth et al., 2004], and centrosomal and acentrosomal pathways are believed to occur simultaneously in cells with centrosomes. Of interest, therefore, are acentrosomal spindles and the motors and cross-linkers involved in their formation. Some of these motors and cross-linkers have roles in multiple mitotic phenomena, such as chromosome movement, spindle bipolarity control, and microtubule focusing. Experimental investigation of, for instance, spindle-pole-specific functions of motors and cross-linkers requires a structure analogous to a single pole.

An acentrosomal spindle pole analog is the focus of Chapter III. The remainder of this chapter provides a brief review of spindle mechanics and of this spindle pole analog.

2.3 The mechanics of mitosis

The mechanical nature of mitosis was evident to early cytologists who attempted to mechanically probe the spindle. That post-metaphase chromosome attachment is mechanically robust was established by using a fine glass needle to move insect-cell contents:

> "When once the chromosomes have separated in metaphase, no interference short of total destruction of the cell will prevent the passage of the daughter chromosomes to their respective poles." [Chambers, 1914]

Consistent with this, later attempts to detach a half-bivalent during insect anaphase I, often "designed to try every conceivable mode of punishment until detachment was obtained or death intervened," killed about 70 % of cells [Nicklas and Staehly, 1967] and no early- to mid-anaphase detachment was obtained except with the X chromosome. The nature of mechanical connections was explored by attempting to move

bivalents (tetrads), for instance, laterally (parallel to the metaphase plate). Mechanical attachment fibers could not be observed, and their existence of was inferred based on the direction-dependent resistance to movement of bivalents. Later micromanipulation studies in which the fibers could be observed supported the view that spindle poles and bivalents were mechanically connected by birefringent chromosomal fibers, which were relatively flexible but relatively inextensible and which buckled under compression [Begg and Ellis, 1979a,b]. In a more recent investigation of interconnections among spindle microtubules, Gatlin et al. [2010] skewered *Xenopus* extract meiotic spindles with glass microneedles, observing that the spindle moved such that the needle approached and passed through the pole slightly slower than speeds typically reported for poleward flux. Motion slowed as the needle approached the pole, and the pole (based on NuMA staining) split to allow the needle to pass through it, suggesting weak or dynamic cross-links at the pole, though the slowing may have simply been due to slowing of flux at the pole. Inhibition of dynein, which is implicated in transport toward poles, caused pole splaying, lengthened the spindle, and eliminated the slowing of needle-spindle translocation as the needle approached the pole. The authors also skewered spindles with a pair of needles positioned on opposite sides of the metaphase plate and pulled the needles toward opposite poles, finding that spindle lengthening by deformation began only when the needles were separated by roughly 80 % of the spindle length. These studies suggest that chromosomes are attached to poles by microtubules that in much of the spindle are not laterally connected by mechanically strong cross-links.

The remainder of this section focuses mainly on recent quantitative studies of the response of mitotic entities to mechanical perturbations.

2.3.1 Spindle deformation

The overall distortion of the spindle when subjected to experimentally applied forces has been investigated. For instance, Dumont and Mitchison [2009] compressed mitotic Ptk2 cells using an agarose pad, causing widening and elongation of the spindle, with elongation occurring on a longer timescale and resulting from lengthening of kinetochore fibers. The authors concluded that this elongation was due to slowing of microtubule depolymerization at the poles with no apparent effect at kinetochores, so that kinetochore fibers were under tension near kinetochores and under compression near poles. Itabashi et al. [2009] used a piezo-controlled dual cantilever system to mechanically perturb *Xenopus* meiotic spindles. Spindles were compressed between the cantilevers either parallel to or perpendicular to the pole-pole axis. For small (less than 10 %) perpendicular compression, spindles were viscoelastic, returning to their original shape over multiple compression cycles. Stiffness was (1.2 ± 2.2) pN/nm (mean±s.d.). Small pole-to-pole compression was also viscoelastic, with stiffness (2.7 ± 3.3) pN/nm (mean±s.d.). Large (tens of %) perpendicular compression had relatively complex effects, including spindle elongation and apparent disruption of spindle architecture. The spindle partially recovered from this disruption over minutes. Overall, the spindle appears to be viscoelastic under small deformation, yet it adapts its architecture in response to large mechanical perturbations.

2.3.2 Chromosome deformation

The bending rigidity of chromosomes due to thermal forces, as well as the Young's modulus of chromosomes as measured when stretched lengthwise by a pipette have been estimated and found to be consistent with a model of the chromosome as a homogeneous elastic rod [Poirier et al., 2002]. The mechanics of interactions between microtubules and both chromosome arms and kinetochores have also be investigated.

2.3.3 Microtubule-chromosome interactions

The load-bearing mechanical coupling used by kinetochores to harness microtubule depolymerization forces for poleward movement has been investigated in several studies. The stall force for anaphase chromosome movement during insect meiosis was measured to be 4 orders of magnitude more than would be required to overcome viscous drag [Nicklas, 1983]. In a later study of isolated Chinese hamster ovary chromosomes [Hunt and McIntosh, 1998], the link between kinetochores and growing or rapidly-shortening microtubules was maintained without a need for ATP. The microtubule-kinetochore coupling decreased the frequency of catastrophe and slowed rapid shortening. Furthermore, when an optical trap held a microtubule connected to a kinetochore moving away at roughly 2 µm/s, the microtubule-kinetochore connection supported a tension of 15 pN while allowing microtuble growth. (For reference, the tension for microtubule-kinetochore attachment *in vivo* has been estimated to be in the range 0.4 to 8 pN per microtubule [Powers et al., 2009, references therein]. The stall force measured by Nicklas [1983] has been computed to correspond to 8 to 210 pN per microtubule [Hunt and McIntosh, 1998].) Akiyoshi et al. [2010] examined the interaction of microtubules and bead-linked purified yeast kinetochore particles lacking motor proteins and the Aurora B protein kinase. They found that single particles formed remarkably robust attachments, consistent with *in-vivo* attachments. This robustness increased with tension due to a combination of effects. The rate of microtubule-kinetochore detachment was lower for growing than for shortening microtubules, and increasing tension promoted growing microtubules by promoting rescue and markedly suppressing catastrophe. Furthermore, although shortening microtubules detached at a relatively high rate, this rate decreased with tension. The authors interpreted their data in terms of a two-state catch-bond model in which a polymerizing microtubule corresponds to the more strongly-bound state. Rupture force was consistent with other studies; when the force was increased at 0.25 pN/s,

the mean rupture force was 9.1 pN. The microtubule-kinetochore connection is thus strong yet able to accommodate exchange of tubulin subunits. The molecular basis of this connection is of interest.

Among molecular components implicated in kinetochore-microtubule connection are KNL1 (Spc105 in budding yeast) and the Ndc80 complex [reviewed by Cheeseman and Desai, 2008]. The latter is a rod-shaped heterotetramer with globular domains at its ends [Wei et al., 2005]. Two components of this complex, Ndc80 and Nuf2, are oriented in the kinetochore toward microtubules [Cheeseman and Desai, 2008]. The budding-yeast Ndc80 complex has been observed to be longer during metaphase, when it is presumably under higher tension, than in anaphase [Joglekar et al., 2009]. Powers et al. [2009] found that beads coated with this complex can diffuse on the microtubule lattice and track the tip of a rapidly shortening microtubule, with on the order of 10 complexes being sufficient to maintain attachment against an optical-trap load on the order of 1 pN. For particles of 1 or 2 GFP-labeled complexes not attached to beads, interactions with microtubules were found to be sensitive to ionic strength, suggesting the importance of electrostatic interactions. Results were consistent with diffusion that can be biased by microtubule shortening. Akiyoshi et al. [2010] found that the binding of kinetochore particles to microtubules was impaired upon mutation of Ndc80 or Spc105, which is consistent with binding observed for purified Ndc80 and KNL1 [Cheeseman et al., 2006]. Also present at kinetochores are microtubule tip trackers and depolymerizing kinesins, as well as molecular motors dynein and kinesin-7 (CENP-E) [roles reviewed by Cheeseman and Desai, 2008; Cheeseman et al., 2006].

Polar-ejection forces, which are mechanical interactions between microtubules and chromosome arms that push chromosomes away from the nearest pole, have been measured by optical trapping [Brouhard and Hunt, 2005]. These ATP-dependent unidirectional forces frequently exceeded 1 pN while rarely exceeding 2 pN and produced peak velocities in the tens of nm/s. Antibody inhibition implicated the chromokinesin

Kid (kinesin-10) in this movement and suggested the chromokinesin KIF4 (kinesin-4) may be less important, which is consistent with other results [Bieling et al., 2010, references therein].

Although our limited comprehension of spindle mechanics is aided by quantitative and qualitative studies [reviewed by Mogilner and Craig, 2010], we have limited mechanical data on spindles, particularly with high-resolution quantification of force and movement, and we know relatively little about the mechanical connection of microtubules to spindle poles. Spindle poles are sites of convergence of spindle microtubule minus-ends near centrosomes and are the regions of the spindle with the highest density of microtubule-crosslinking [Gatlin et al., 2010; Mastronarde et al., 1993; Nicklas et al., 1982]. It has been proposed that poles are key load-bearing structures essential for chromosome movement and generation of euploid cell progeny [Gordon et al., 2001]. Spindle poles are therefore the focus of Chapter III, and a review of experimental spindle pole analog systems is required.

2.4 Spindle pole analogs

Formation of microtubule asters has been demonstrated with only microtubules and a motor with a non-motor microtubule-binding domain [Hentrich and Surrey, 2010], yet mitotic aster constituents include microtubule cross-linkers and both plus- and minus-end directed motors. Based on experiments and simulations with purified systems of motors and microtubules, factors important to the pattern of microtubules formed include motor concentration, processivity, and microtubule-end residence time [Surrey et al., 2001]. Presumably, microtubule cross-linkers could reduce the need for long microtubule-end residence times in asters with more physiological relevance, such as those formed with mitotic and meiotic extracts.

Xenopus oocyte extracts [Itabashi et al., 2009; Karsenti and Vernos, 2001] provide a convenient system for the study of acentrosomal vertebrate spindles. Another

spindle-pole analog suitable for experimentation is an acentrosomal astral microtubule array from cell-free extracts from mitotic HeLa (human) cells [Gaglio et al., 1995]. Such mitotic asters have been characterized biochemically, and perturbing components yields various effects on microtubule organization [Chakravarty et al., 2004; Gaglio et al., 1995, 1996; Mountain et al., 1999]. Furthermore, due to reduced debris, HeLa extracts are likely better suited to optical trapping experiments than *Xenopus* extracts.

Emphasizing the physiological relevance of mitotic HeLa-extract asters are several experimental results in which perturbing extract components has a similar effect in cultured cells or HeLa or *Xenopus* extracts [reviewed by Compton, 1998]. For instance, NuMA (Nuclear protein that associates with the Mitotic Apparatus), which in PtK1 mitotic spindles forms part of an insoluble matrix distinct from centrosomal material [Dionne et al., 1999], is important for the formation of spindle poles. Immunogold electron microscopy images of HeLa spindle poles and HeLa extract asters show similar NuMA-containing matrices that appear to anchor microtubule minus ends and, in extract asters, make portions of microtubules nocodazole resistant [Dionne et al., 1999]. Gaglio et al. [1995] found that perturbing NuMA in monkey cells resulted in disorganized spindles, while perturbing NuMA in HeLa extracts prevented formation of asters. However, this effect is reversed when kinesin-5 is also depleted from the extract [Gaglio et al., 1996]. In mitotic (i.e., fertilized) *Xenopus* egg extracts, NuMA is required for spindle formation but not aster formation [Merdes et al., 1996]. The effects of perturbing molecular motors have been further investigated. Perturbing kinesin-5 in extracts or monkey cells causes expansion of the pole, with microtubules less tightly focused and NuMA occupying a larger volume (in the case of cultured cells, the shape of the NuMA distribution was also different, presumably because the spindle is monopolar) [Gaglio et al., 1996]. Perturbing dynein disrupted NuMA localization and microtubule focusing in metaphase monkey

cells, which have centrosomes, and in mitotic asters [Gaglio et al., 1997]. Perturbing kinesin-14 impaired formation of acentrosomal asters in cells and HeLa extracts, but not in cells with centrosomes. Simultaneous inhibition of kinesin-14 and kinesin-5 resulted in aster formation, leading to the conclusion that (plus-directed) kinesin-5 has an antagonistic relationship with (minus-directed) dynein and kinesin-14 Mountain et al. [1999]. Taken together, the roles of NuMA, dynein, kinesin-5, and kinesin-14 are generally similar in extract asters and in mitotic cells.

Based on simulations with components important to HeLa extract asters [Chakravarty et al., 2004], major factors affecting aster formation include the orientation (parallel or antiparallel) of microtubule cross-links by motors and cross-linkers, as well as the net minus-end directed force (a measure of the balance of minus- and plus-end directed motors). Factors that affect other aster properties, such as aster mechanics, may differ from those affecting microtubule organization, and such properties may be relevant to the ability of spindle poles to sustain forces while allowing tubulin subunit exchange at microtubule minus ends (this requirement is discussed by Dionne et al. [1999]).

These asters are therefore assumed to be acentrosomal analogs of mitotic spindle poles. Chapter III investigates their mechanics.

CHAPTER III

Mechanics of mitotic asters

We examine* the mechanical properties of mitotic asters that recapitulate the properties of spindle poles in a mammalian mitotic cell extract. These asters are composed of microtubules and numerous motor and nonmotor microtubule-associated proteins, and serve as surrogates for mitotic spindle poles. We have previously extensively characterized the biochemical properties of these microtubule asters and have shown that they faithfully recapitulate functional aspects of spindle poles. For mechanical analysis, we have applied optical trapping techniques to this experimental system to study mechanical events at the nanometer scale. With these high-resolution tools, we confirm that asters are steady-state assemblies and show that the linkage of microtubules to the asters is highly compliant. Finally, we combine this approach with molecular manipulation to explore the contribution of the homotetrameric motor Eg5 to the mechanical properties of spindle poles.

*Most of this chapter is published as Charlebois et al. [2011], a shared-first-authorship collaboration described in the acknowledgements (p. iv).

3.1 Materials and methods

3.1.1 Cell culture

HeLa cells were maintained in Dulbecco's modified Eagle's medium containing 10% bovine growth serum, 50 IU/mL penicillin, and 50 µg/mL streptomycin. Cells were grown at 37 º C in a humidified incubator with a 5% CO_2 atmosphere.

3.1.2 Mitotic aster preparation and assay execution

Mitotic extracts from HeLa cells were prepared according to Gaglio et al. [1995]. HeLa cells were arrested in mitosis by a double block with 2 mM thymidine followed by nocodazole treatment (10 ng/mL) for 10–12 h. Mitotic cells were collected by shake-off and incubated for 30 min at 37 ºC with 20 µg/mL cytochalasin B. The cells were then collected by centrifugation at 1500 rpm and washed twice with cold PBS containing 20 µg/mL cytochalasin B. Cells were washed one last time in cold KHMM (78 mM KCl, 50 mM HEPES, 4 mM $MgCl_2$, 1 mM $MnCl_2$, 2 mM EGTA, 1 mM dithiothreitol, pH 7.0) buffer containing 20 µg/mL cytochalasin B, and finally dounce-homogenized (tight pestle) at a concentration of ~3×10^7 cells/mL in KHMM buffer containing 20 µg/mL cytochalasin B, 20 µg/mL phenylmethylsulfonyl fluoride, and 1 µg/mL each of chymostatin, leupeptin, antipain, and pepstatin.

The crude cell extract was then subjected to sedimentation at 20 psi for 20 min at 4º C in an Airfuge (Beckman Coulter, Brea, CA). The supernatant was recovered and supplemented with 2.5 mM ATP (prepared as Mg^{2+} salts in KHMM buffer), 20 µM taxol and 0.075–0.1 mg/mL biotin-tubulin (Cytoskeleton, Denver, CO). For immunodepletions, the supernatant recovered was incubated with antibody-coated agarose beads as described in Gaglio et al. [1996] and depletion confirmed by immunoblotting. Where indicated, monastrol was added at this stage at a final concentration of 100 µM. This supernatant was stored on ice up to a maximum of 4 h. To stimulate

assembly of mitotic asters, this supernatant mix was incubated at 30 ºC for 40 min.

After incubation, the extract containing asters was flowed into an experimental chamber with aluminum foil spacers maintaining a chamber depth of ~70 µm, and then sealed with VALAP (a 1:1:1 mixture by mass of Vasoline, lanolin, and paraffin, though we increased the paraffin content by ~8%). Asters were nonspecifically adhered to the coverglass by centrifuging the chamber at 270g for 3 min. The VALAP was removed and a solution of KHMM containing 2.5 mM adenine nucleotide, NeutrAvidin-coated beads (prepared as described in Charlebois et al. [2010], but with final rinse with and resuspension in KHMM, and with dilution by ~3:100) was flowed in. For monastrol experiments, 100 µM monastrol was also added to this solution. The chamber was then resealed.

With the experimental chamber on the microscope stage (our optical tweezers apparatus is described elsewhere [Brouhard et al., 2003; Schek et al., 2007]), a bead was trapped and brought to microtubules at the aster periphery. Because of the limits of light microscopy, it was not possible to determine unequivocally the exact number of microtubules with which a bead interacted, but the contrast was consistent with one or a few microtubules, and thicker, higher-contrast bundles were avoided. After attachment, an antipoleward force (see Figs. A.2-A.3 on pp. 143-144; typically 2–4 pN, sufficient to maintain the microtubule under tension but generally not large enough to detach the microtubule) was applied using the force-clamp. Experiments were performed with the top of the bead 1–15 µm below the coverglass, typically 2.5–10µm, with the bead attached to a microtubule or bundle in the plane of focus.

3.1.3 Tracking movements of microtubules in the aster

Bead and aster-focus position were tracked using LabView Vision software (National Instruments, Austin, TX). A rectangular region of interest surrounding the bead or aster focus was chosen and the Vision VI "IMAQ Match Pattern 2" was used

to find this pattern in all images for the trace in question. For a given trace, this was repeated with patterns taken from different time points, generally 20–80 s apart, and these resulting image-based traces were averaged. Bead and aster-focus positions were then subtracted, yielding changes in bead position relative to the aster focus at ~5 or ~28 Hz. The ~28-Hz traces of aster movement were filtered with a three-point median filter. The uncertainty in bead position relative to the aster focus appears, based on the limited movement in our AMP-PNP data (in which the motors are in rigor, severely restricting microtubule movement; see Fig. 3.2), to have been small relative to excursions observed in the presence of ATP.

3.1.4 Algorithm identifying excursions of roughly constant velocity

Position versus time traces were analyzed using an algorithm that performs least-squares linear fits to successive time intervals of variable length. Initially a line is fit over a time interval $\tau_{\min}$ =2 s at the beginning of a trace. The algorithm then extends this line forward 1 s. If at least 90% of the residuals (data minus fit) are >10 nm, or if at least 90% of them are <-10 nm, the algorithm rejects the extension and, from the last point of the current (preextension) interval, begins a new fit. Otherwise, the algorithm accepts the first 10% of the data points of the extension, and attempts a new extension.

3.1.5 Computing κ_{a} from changes in stiffness experienced by the bead

Before attachment to the aster, the stiffness experienced by the bead is due to the known trap stiffness, κ_{trap}. Attachment to an aster increases stiffness to $\kappa_{\mathrm{trap}} + \kappa_{\mathrm{a}}$, where κ_{a} is the effective stiffness experienced by the bead due to its attachment to the aster. Factors contributing to κ_{a} are the compliance of the bead-microtubule connection (bead rocking) and microtubule-aster focus connection. The former was estimated to be 0.021 pN/nm in a previous study [Schek et al., 2007]. In addition,

the sensitivity to conditions under which asters are formed (Fig. 3.3 A), and the consistency with compliances estimated from cross-link breaking events (Fig. 3.3 B), indicate that the compliance is dominated by the microtubule-aster focus connections. By the equipartition theorem, we expect

$$\kappa_{trap} = k_B T / var(x_{pre}) \tag{3.1}$$

$$\kappa_a + \kappa_{trap} = k_B T / var(x_{post}) \tag{3.2}$$

where k_{B} is Boltzmann's constant, T is the absolute temperature, x_{pre} and x_{post} are the bead position relative to the trap center (x_{bead} in Fig. 3.1 C) before and after attachment, respectively, and var(x) is the variance of x. From Eqs. (3.1) and (3.2), we can obtain either of the following:

$$\kappa_a = \kappa_{trap} \left(\frac{var\left(x_{pre}\right)}{var\left(x_{post}\right)} - 1 \right) \tag{3.3}$$

$$\kappa_a = k_B T \left(\frac{1}{var\left(x_{post}\right)} - \frac{1}{var\left(x_{pre}\right)} \right). \tag{3.4}$$

Equation (3.3) has the advantage of being independent of the sensitivity constant used to convert quadrant photodiode voltages to positions, whereas Eq. (3.4) is independent of the trap stiffness. We used both Eqs. (3.3) and (3.4) to compute each stiffness and averaged these values for each time interval analyzed, yielding Fig. 3.3 A (see later). Values obtained from Eqs. (3.3) and (3.4) were similar: the correlation coefficient is r = 0.94, and the mean difference is -0.001 pN/nm, SD 0.01 pN/nm.

The expression var(x) was calculated by computing the variance of successive 0.05-s windows (overlapping, with each window beginning 0.01 s after the preceding one) and averaging these variances. T was 307 K.

3.1.6 Computing κ and γ from exponential fits

For the decay toward mechanical equilibrium of a damped harmonic oscillator in low Reynolds number conditions, and under constant force (see free body diagram in Fig. 3.3 B, inset), the position, x, as a function of time, t, is

$$x(t) = \frac{F}{\kappa_a} - fe^{-\kappa_a t/\gamma} \tag{3.5}$$

where κ_{a} is as in Fig. 3.3 A, γ is the drag coefficient, F is the applied (force clamp) trap force, and $f \in \Re$ is a constant determined by the initial conditions. The values κ_{a}, γ, and f are fitting parameters. For curve fitting, the data were translated such that the initial time and position were zero. Origin software (OriginLab, Northampton, MA) fit the data to Eq. (3.5) with initial values $f = 50$ nm, $\kappa_{\mathrm{a}} = 0.03$ pN/nm, and $\gamma = 0.006$ pN/(nm/s). All parameters were restricted to be ≥ 0.

3.2 Results and discussion

To examine directly the mechanics of microtubule linkages at spindle poles we used cell-free mitotic extracts and optical trapping. Microtubule asters that form in the cell-free system have been extensively characterized, and have been shown to recapitulate accurately spindle-pole organization in cells, including: that they require the biochemical activities of the nonmotor microtubule cross-linking protein NuMA and minus-end-directed motor activity (cytoplasmic dynein, HSET); that they become less tightly focused after depletion of the plus end-directed motor Eg5; that they are sensitive to antagonistic functional relationships between motors with opposite directionality; and that they form in a centrosome-independent manner [Gaglio et al., 1995, 1996, 1997; Mountain et al., 1999].

Microtubule asters assembled under these conditions lack microtubule polymerization dynamics and poleward microtubule flux at spindle poles. Although the absence

of flux is less physiologic, this worked to our advantage in determining the mechanics of microtubule linkages within asters without the confounding influence of microtubule depolymerization at the poles.

For optical trapping, microtubules in the asters were assembled with extract tubulin supplemented with biotinylated tubulin, and the asters were gently centrifuged into contact with a flow-chamber coverglass (Fig. 3.1 A). An optical trap moved a 0.57-µm NeutrAvidin-coated bead into contact with the microtubules at a point far from the aster focus to minimize the number of microtubule attachments (Fig. 3.1, A and B). A force-clamp maintained a constant antipoleward force by frequently (10 Hz) repositioning the trap (black trace in Fig. 3.1 C) to maintain the displacement of the bead, x_{bead}, relative the to the trap center (Fig. 3.1 D). The positions of the aster focus and bead were tracked using video-enhanced differential interference contrast microscopy (green and cyan traces, respectively, in Fig. 3.1 C). Changes in bead position relative to the aster focus (red trace in Fig. 3.1 C) corresponded to microtubule movement toward or away from the aster focus.

3.2.1 Motor-driven microtubule movement

In the presence of ATP, aster microtubules made excursions in both the poleward and antipoleward directions relative to the aster focus (Fig. 3.1C, Fig. 3.2A, and Figs. A.2-A.3 on pp. 143-144). Thus, motors at the pole were capable of generating bidirectional movements but these could have been biased poleward in the presence of dynamic microtubules, resulting in or accommodating poleward flux. Excursions corresponded to intervals of roughly constant velocity, identified by an algorithm (see Materials and Methods) that fit an initial window of the position versus time data trace, and projected this fit forward in time until the position data became inconsistent with the constant velocity assumption.

The velocities, v_x, and run-distances, Δx, of these excursions were roughly sym-

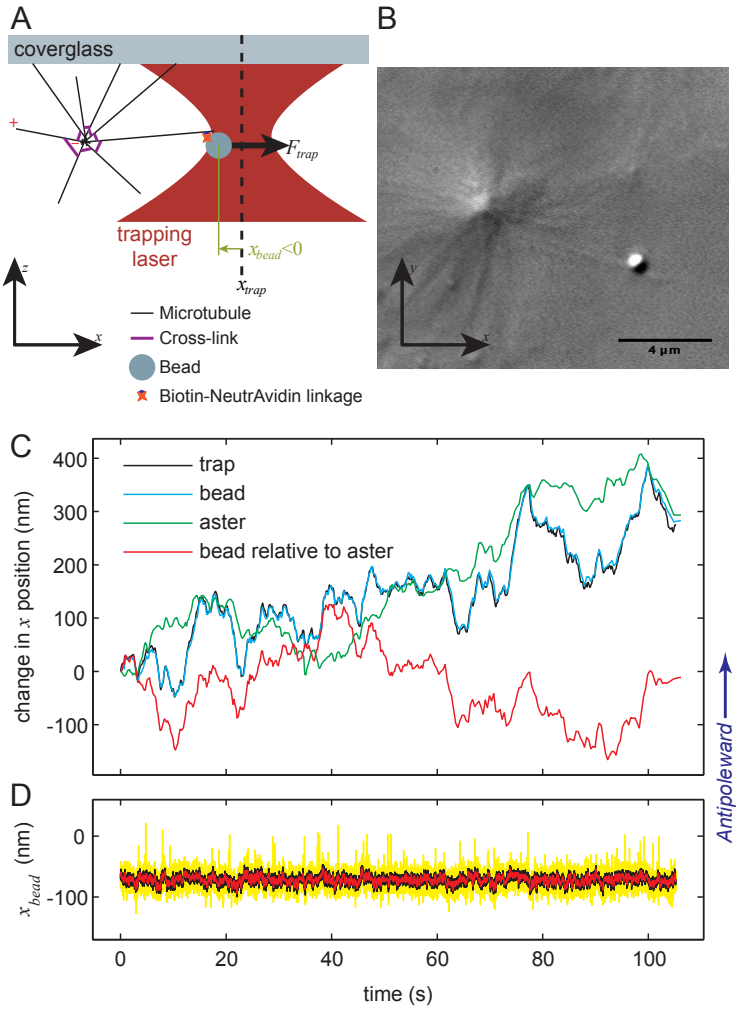

Figure 3.1: Experimental design and example of laser trap analysis of spindle poles. (A) Assay schematic: a bead is attached to an aster arm and pulled in the x direction. (B) Differential interference contrast image of an aster and attached bead. (C) Plot showing position changes versus time. The trap trace is a record of trap movement as controlled by the force clamp routine (10 Hz), whereas the other traces are based on tracking bead and aster movement in images (5 or 30 Hz). The red trace shows bead movement corrected for aster movement. The traces of Fig. 3.2, Fig. 3.3B, Figs. A.2-A.3 (pp. 143-144), and Fig. A.5A (p. 146) are corrected in the same manner. Positive direction corresponds to antipoleward direction. (D) Plot showing bead position relative to trap center (5 kHz), unfiltered (yellow) and low-pass filtered with a cutoff of 100 Hz (black) or 10 Hz (red) as described in Materials and Methods.

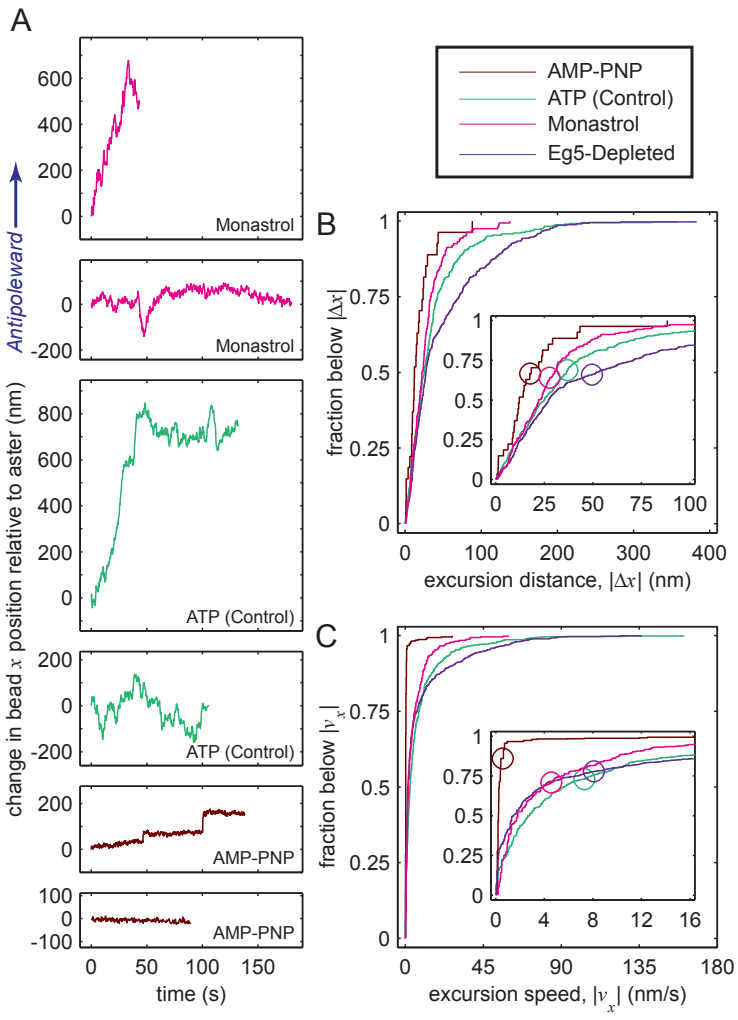

Figure 3.2: Run-lengths and velocities of microtubules anchored to spindle poles. (A) Example traces of changes in bead x position relative to the aster versus time (these correspond to the red trace of Fig. 3.1 C). Each trace is from a different aster. (B and C) Analysis of corrected bead movements versus time using an algorithm that fits straight lines to successive time intervals of variable length. Graphs are cumulative distribution function of (B) absolute run distance, $|\Delta x|$, and (C) time-weighted absolute speed, $|v_x|$. (Insets) The same plots zoomed to lower values and with mean absolute values marked with a circle. See also Figs. A.2-A.4 on pp. 143-145.

metrically distributed between poleward and antipoleward directions (Fig. A.4 on p. 145), although v_x displayed a modest antipoleward bias (roughly 2 nm/s) under the applied forces (typically 2–4 pN; see Table 3.1). Mean v_x near zero is expected for all conditions that produce asters, as consistent net movement of all microtubules in one direction would result in aster disassembly. Therefore, the range of magnitudes of Δx and of v_x between experimental conditions was compared by their variances (Table 3.2) and the cumulative distributions of $|\Delta x|$and $|v_x|$(Fig. 3.2, B and C).

Excursions were highly variable, with some movements persisting for hundreds of nanometers in either direction (Fig. 3.2B and Fig. A.5), consistent with molecular motors taking tens of steps [Toba et al., 2006; Valentine et al., 2006]. The absolute velocity of an excursion, $|v_x|$, was often tens of nm/s (Fig. 3.2C and Figs. A.2-A.4 on pp. 143-145). Microtubules sometimes moved hundreds of nm antipoleward before pausing, and could then resume antipoleward excursions or reverse to move poleward (Figs. A.2-A.3). Because the optical trap applied tension in these experiments, antipoleward movements may have been due to decreased poleward forces, due to disengaging motors for example, rather than active pushing forces. The nonhydrolyzable ATP analog AMP-PNP suppressed poleward and antipoleward microtubule excursions (Fig. 3.2A and A.2), and this was reflected by significantly lower ($p < 0.05$) variances for v_x and Δx (Table 3.2). Furthermore, the cumulative distributions of $|\Delta x|$and $|v_x|$were shifted toward lower values (Fig. 3.2B and C). These data indicate that bidirectional motion of microtubules in the asters required active microtubule motors.

However, it could be argued that the antipoleward movements observed in the presence of ATP would not occur in the absence of the tension applied by the optical trap. We provide two counterarguments. First, the applied tension (Figs. A.2-A.3) was usually modest relative to that expected to be developed by a few motors. Second, for motors to cause exclusively poleward movement, plus-directed motors would have

Table 3.1: Summary statistics for Δx and v_x

	n	Δt (s)	$\langle v_x \rangle$ (nm/s)	var(v_x) (nm^2/s^2)	p	$\langle \Delta x \rangle$ (nm)	var(Δx) (nm^2)	p
ATP	405	2045	2.2 ± 0.8	234	0.0037	11 ± 3	3160	7.3×10^{-5}
AMP-PNP	27	838	0.2 ± 0.4	5.26	0.61	7 ± 5	597	0.14
Eg5-depletion	423	2590	1.9 ± 0.9	334	0.037	11 ± 4	5220	0.0013
Monastrol	161	976	0.8 ± 0.7	71.1	0.22	5 ± 3	1340	0.088

Summary of analysis of v_x and Δx. n is the number of segments identified, Δt is the total time analyzed. v_x is time-weighted while Δx is not. p is for a 2-tailed t-test with the null hypothesis that the mean is zero. See also Fig. 3.2.

Table 3.2: Statistical comparison of Δx and v_x distributions.

			Difference in v_x distribution		Difference in Δx distribution	
			t-test (mean)	Bartlett test (variance)	t-test (mean)	Bartlett test (variance)
AMP-PNP	vs.	control	0.024	0	0.46	3.7×10^{-6}
AMP-PNP	vs.	monastrol	0.46	1.2×10^{-10}	0.7	0.015
AMP-PNP	vs.	Eg5-depleted	0.1	0	0.47	1.3×10^{-8}
control	vs.	monastrol	0.17	4.4×10^{-16}	0.12	1.3×10^{-9}
control	vs.	Eg5-depleted	0.76	0.00031	0.96	4.1×10^{-7}
monastrol	vs.	Eg5-depleted	0.35	0	0.15	0

p-values for t and Bartlett tests comparing means and variances (for v_x, tests were performed using time weighted values of mean and variance). See also Fig. 3.2.

to be linked to a static matrix whereas minus-directed motors would have to have their tails attached to moving microtubules while their heads walked on relatively static microtubules. This second argument does not exclude the possibility that there would be no motion in the absence of the optical-trap tension, but a perfectly static aster seems unlikely.

We also note that plus- and minus-end directed motors have been shown to participate in aster organization in this system [Gaglio et al., 1996, 1997; Mountain et al., 1999], and bidirectional movements have been observed in vitro in microtubule gliding assays where motors with opposite directionality act competitively [Tao et al., 2006], although we detected movement with much higher spatiotemporal resolution and the excursions we observed tended to be much shorter. The ATP-dependent microtubule movements suggest that motors play an important role maintaining the mechanical properties of the aster.

The effect of perturbing Eg5 is discussed on p. 41.

3.2.2 Compliance obtained from thermal motion of the bead

Microtubule movements will strain linkages that hold microtubules to the aster focus. Our assay measures the overall stiffness of the microtubule plus its anchoring by an unknown number of cross-links to the aster. Although the attached bead was located microns from the aster focus, the longitudinal microtubule compliance was negligible compared with the compliances we observed [Felgner et al., 1996; Gittes et al., 1993; Mickey and Howard, 1995; Tuszynski et al., 2005; Venier et al., 1994], so the observed compliance was dominated by compliance at the aster. We measured the stiffness, κ_{a}, of the bead-microtubule-aster linkages (Fig. 3.3 A, inset) by comparing the thermal fluctuations of the bead before and after attachment to an aster microtubule and applying the equipartition theorem.

Under control (ATP) conditions,we obtained κ_{a} =0.0255±0.005 pN/nm (mean

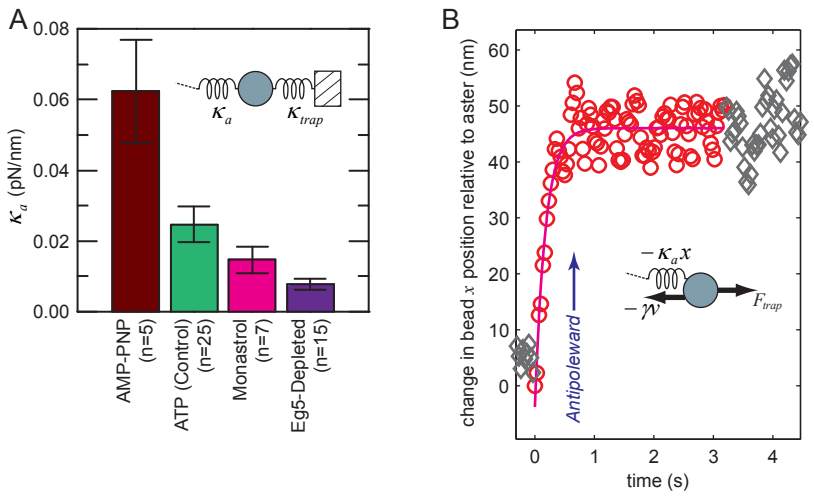

Figure 3.3: Analysis of stiffness of microtubule linkage to spindle poles. (A) Values obtained for κ_{a} under each experimental condition; for a linkage of stiffness κ_{a}, an applied load F will move the bead a distance F/κ_{a}. Error bars indicate standard error. The value n represents the number of traces under different experimental conditions including different forces or asters; between three and eight asters were examined for stiffness for each biochemical condition (see Figs. A.2-A.3 on pp. 143-144). (Inset) Physical model from which Eqs. 3.3 and 3.4 are derived: the bead is subject to forces from the trap stiffness, κ_{trap}, and the unknown stiffness, κ_{a}. (B) Fit of Eq. (3.5) to the first exponential jump. The spring force is $-\kappa_{\mathrm{a}}x$ and the drag force $-\gamma v_x$ where κ_{a} is the stiffness and γ is the drag coefficient. Position data are the corrected bead x positions (see red trace of Fig. 3.1 C, and note that aster moved little during this time, as evident in Fig. A.5B and C on p. 146). (Red circles) Data included in the fit. (Gray diamonds) Data points outside this range. (Magenta line) The fit. The position and time axes are shifted so the data involved in the fit begin at zero. (Inset) Physical model from which Eq. (3.5) is derived: the bead and aster arm are subject to the force applied by the optical trap in addition to forces equivalent to a Hookean spring of stiffness κ and a force proportional to velocity (dashpot) with drag coefficient γ.

±SE; Fig. 3.3 A). This is an order of magnitude less than the rabbit acto-myosin cross-bridge [Veigel et al., 1998] or of several domains of the structural protein titin [Rief et al., 1997]; and it is two orders of magnitude less than a frog extract spindle under gentle compression perpendicular to the metaphase plate (in which there are presumably far more entities acting in parallel against the applied force) [Itabashi et al., 2009]. However, it is an order of magnitude more than chromosomes [Poirier et al., 2002]. When ATP was replaced by AMP-PNP, the stiffness of the linkage increased (Fig. 3.3 A), probably due to more sustained binding of motors to microtubules.

3.2.3 Compliance and drag obtained from exponential fits

In the presence of AMP-PNP, we observed several abrupt jumps in the position of the bead relative to the aster focus (Fig. 3.2A and Fig. A.5 on p. 146) indicating failures in the mechanical structure. The force applied by our laser trap under these conditions was extremely unlikely to break the NeutrAvidin-biotin linkage between the bead and attached microtubule on the timescale of the experiment [Yuan et al., 2000]. Thus, these abrupt jumps most likely represented rupture of a load-bearing cross-link between the microtubule and the aster. These failure events provided a complementary approach to determine the stiffness of the linkage of microtubules to the aster. After each failure, the microtubule relaxed in the direction of the trap force to a new position, which was stable because motor activity was suppressed by AMPPNP. The exponential form of the jumps was consistent with decay toward mechanical equilibrium of an overdamped harmonic oscillator (i.e., Hookean spring with linear drag) under a constant force, F (Fig. 3.3 B, inset), where the low Reynolds number allows mass to be neglected (Eq. (3.5)).

Exponential fits (Fig. 3.3B and Fig. A.5) yielded κ_{a} =0.0587±0.0005 pN/nm for the first jump and 0.0339±0.0003 pN/nm for the second, consistent with estimates

from analysis of thermal motion (Fig. 3.3A) for the same aster. These exponential jumps, and the decrease in stiffness by roughly half after the first jump, are most directly explained by the loss of microtubule cross-links. As the trace shows no signs of breaks occurring in rapid succession, and because it is unlikely that several cross-links would break at the beginning of the jump simultaneously (within roughly 0.1 s of each other), it is reasonable to expect that each event corresponded to failure of a single microtubule cross-link. Assuming the cross-links had similar compliances, the 43% stiffness decrease after the second break suggests the breaking cross-link was 1 among 2–3, in which case there were 3–4 cross-links at the beginning of the trace. Although these estimates are from fortuitous observations of crosslink breaking, the consistency of the stiffness with other asters (Fig. 3.3 B) suggests they are not atypical.

Exponential fits to each jump (Fig. 3.3B and Fig. A.5) yielded drag coefficients, γ, of 10.4±0.9 pNs/µm for the first jump and 7.4±0.5 pNs/µm for the second. These values are three orders-of-magnitude larger than expected from viscous drag on the microtubule and bead (see Discussion A in the Supporting Material), presumably because relaxation also involved shifting of microtubules attached to the microtubule under consideration, with possible contributions from friction between moving components of the aster. High drag is likely to be physiologically important, as it will slow the movement of a microtubule that detaches under tension, and thereby allow more time for motors and cross-linkers to make new attachments. However, the drag was not so high as to overload mitotic motors; at typical ~10 nm/s speeds of microtubule flux [Cameron et al., 2006], the drag is well below the pN forces that are commonly developed by individual motor proteins.

An additional fit was performed on segments between the jumps (Fig. A.6 on p. 147), obtaining a stiffness and drag coefficient for non-breaking elements in series with those that broke. The stiffness was $\kappa_a = 0.062 \pm 0.002$ pN/nm. The drag

coefficient was large at $\gamma = 3.5 \pm 0.3$ pN s/nm. This suggests element(s) with a stiffness similar to others in the system but with severe damping of their speed. However, there is an important caveat. In short, it is difficult to assess whether the change in position observed over the long timescale of these segments is due to poor image-based tracking of the aster position resulting from changes in aster appearance over time. Tracking aster position over time and distance scales of the large, fast jumps (or excursions in the ATP traces) seems to be reliable considering that the jumps are large relative to any long-term movement in the AMPPNP traces. In contrast, we do not have such control data against which to compare the segments of Fig. A.6. Further data with this aster at higher force has similar net movement, and we do not know whether this is due to further change in bead position relative to the aster or due to poor aster tracking.

3.2.3.1 Expected drag on microtubule and bead

The viscous drag coefficient, γ_v, depends on the viscosity, η, and also on the size and shape of the bead and objects attached to it. Below, we give the relationship between expected viscous drag, γ_v, and viscosity, η, and, from this and the observed γ, we obtain the apparent 'viscosity.' We find it to be much larger than that of the buffer, suggesting that viscous forces on the bead and the microtubule contributed little to the observed drag, γ.

The viscous drag coefficient for a bead and microtubule is given by [Happel and Brenner, 1983; Howard, 2001; Tirado and Garciadelatorre, 1979]

$$\gamma_v = 2\pi\eta \left[3a \left(1 + \frac{9}{16}\frac{a}{h} \right) + \frac{L}{\ln\left(L/2r\right) - 0.20} \right] \tag{3.6}$$

where $a = 285$ nm is the radius of the bead, h is the distance from the bead center to the coverglass, and L and r are, respectively, the length and radius of the

microtubule. For the experiment in question, h =6 μm. From the image of the aster and bead, we likely had 5.3 μm$\leq L \leq$7.5 μm. We assume the microtubule or bundle radius was 14 nm$\leq r \leq$28 nm. Setting γ_v in equation (3.6) equal to the values of γ obtained from the fit (section 3.2.3 above; not the additional fit to segments between jumps), our data indicate that the apparent 'viscosity' experienced by the bead and microtubule was 0.46 pNs/μm^2 $\leq \eta \leq$0.87 pNs/μm^2, which is 3 orders of magnitude greater than the viscosity of water (at 34°C, $\eta = 7.34 \times 10^4$ pN s/µm^2). Because most of the surface of the bead-arm complex was in contact with buffer, the high drag coefficient must have been caused by interactions with the portion of the microtubule/bundle in the vicinity of the aster focus, where the effective drag must have been much higher. These interactions may have been relatively stable connections to numerous entities near the focus that moved when the bead and microtubule moved, in which case these would be equivalent to hundreds of beads and short (~5-µm) microtubules. Alternatively, these interactions may have been transient, similar to those observed for kinesin-8 [Bormuth et al., 2009].

3.2.4 Effect of perturbing kinesin-5 (Eg5) by depletion or monastrol treatment

The kinesin-5 motor Eg5, in addition to sliding antiparallel microtubules to promote spindle bipolarity, localizes strongly to spindle poles [Sawin et al., 1992] where it is presumed to cross-link microtubules. It is required for tight focusing of microtubules into asters in this cell-free system and in cells and other model systems [Gaglio et al., 1996; Sawin et al., 1992]. To examine the mechanical role of Eg5 within these microtubule asters, we inhibited its activity by immunodepletion or with the small molecule inhibitor monastrol. With either perturbation, there was no detectable change in mean microtubule excursion velocity or distance compared to controls (Fig. 3.2, B and C, and Table 3.2). However, the variance of excursion velocity and dis-

tance was higher in Eg5-depleted asters (Table 3.2), indicating that the microtubules exhibited a greater range of speed and displacement, in both directions, compared to control asters. This was likely a consequence of greater mechanical compliance, as analysis of thermal motion suggests control asters were stiffer than those formed under Eg5-depleted conditions (Fig. 3.3A, Table 3.3).

Table 3.3: p-values for comparison of κ_a

	control	monastrol	Eg5-depleted
AMP-PNP	0.059	0.029	0.020
control		0.12	0.0032
monastrol			0.12

p-values are for a 2-tailed t-test without assumption of equal variance. κ_a from each subtrace was weighted by the length of the subtrace. See also Fig. 3.3A.

The stiffness of monastrol-treated asters was less than controls and more than Eg5-depleted asters, though not reaching statistical significance from either (Fig. 3.3A, Table 3.3). This is consistent with the observation that monastrol has little effect on Eg5's binding affinity to microtubules [Cochran et al., 2005; Kwok et al., 2006], and suggests that cross-linking by Eg5 tetramers in the presence of monastrol contributes to aster stiffness even though motor activity is inhibited. Although monastrol does not affect Eg5's binding affinity, it still inhibits Eg5's catalytic activity, and thus may still impact the compliance of the asters. This is in agreement with our observation that the compliance of asters is slightly increased in the presence of monastrol, reflecting the contribution of Eg5's motor activity to the aster core's compliance. Taken together, our Eg5-perturbation results suggest that Eg5 imparts stiffness to poles where it cross-links parallel microtubules, which is consistent with the report that bipolar spindles formed in frog egg extracts lacking Eg5 are fragile [Mitchison et al., 2005].

3.2.5 The spindle pole cross-linked by compliant elements

Microtubules in the mitotic spindle converge as they approach the centrosomes at the spindle poles. Pole-focusing components such as motor (cytoplasmic dynein, Eg5, and HSET) and nonmotor (NuMA) proteins crosslink and focus microtubule minus-ends at the poles. Given their proximity, centrosomes may contribute to the mechanical properties of the spindle pole. The studies described here examine the mechanical properties of the acentrosomal asters assembled from cell-free extracts, and are thus most relevant for understanding the role of these cross-linkers. We found that connections between microtubules and the aster focus were very compliant. The source of this compliance is at least partially motor-based as inhibition of motor activity by AMP-PNP reduces the compliance. Nonmotor proteins such as NuMA that can oligomerize via its large coiled-coil region [Saredi et al., 1996] to provide a polymeric matrix may also be contributing to compliance.

We propose that this mechanical property is critical to preserve spindle architecture as individual microtubules experience poleward and antipoleward displacements. Highly compliant microtubule linkages increase the load any individual microtubule can bear by distributing forces among microtubules and motors, similar to a truss (Fig. 3.4 A). However, compliance must be low enough that significant force redistribution occurs before a microtubule under tension is pulled out of the pole. This is consistent with our compliance data showing that ~2 pN would be transmitted after ~80-nm movement, which is small compared to the micron-scale poles. On the other hand, compliance must not be too low, because rigid cross-links will resist relative sliding of adjacent microtubules, which is required for processes such as poleward flux and for changes in the positions of chromosomes (Fig. 3.4, B and C). The compliances we measured would allow a motor to take at least 10 steps before encountering a load that would induce, for instance, Eg5 detachment [Korneev et al., 2007; Valentine et al., 2006]. Thus, to support more extended movements as seen during poleward

flux, cross-links must periodically rearrange to relieve strain. If the compliance were lower such rearrangements would have to occur more frequently, thus diminishing their effectiveness transferring force between microtubules.

A simple model (section A.1 on p. 137) suggests an order-of-magnitude decrease in compliance would diminish the effectiveness of force transfer to the point where microtubules would be frequently lost from the pole if there was not a compensating shift in cross-link dynamics (i.e., an increase in the number of cross-links or in the rate that the new cross-links form). Conversely, an order-of-magnitude increase in the compliance would result in severe distortions in the spindle structure that are not observed in vitro. Furthermore, rigid microtubule crosslinking would fix the angles between microtubules, so that one motor walking along a microtubule would force another motor to disengage (Fig. 3.4 C, as opposed to Fig. 3.4 B).

Matos et al. [2009] have recently proposed that poleward flux-associated slipping of microtubule attachments at kinetochores combined with a visco-elastic coupling of microtubules to the poles comprises a system that can equilibrate tensions across chromosome kinetochores, thus coordinating their movement at the onset of anaphase. Our findings roughly support the model of Matos et al., but suggest that an effect similar to the drag force mediated in their model by passive dashpot elements in series with compliant elements may be mediated in part by ATP-hydrolyzing motors.

The implication of force transmission by compliant crosslinks is that a load on any particular microtubule or microtubule bundle is not borne entirely by the motors directly interacting with that microtubule (Fig. 3.4 A). A corollary is that loads are distributed among motors such that the speeds that microtubules move is relatively coordinated even if their pole-distal ends are attached to different structures and subject to different loads (Fig. 3.4 A). For example, a tension opposing poleward movement of a microtubule will slow not only that microtubule, but also the poleward movement of its neighbors. Likewise, the maximum force that can be sus-

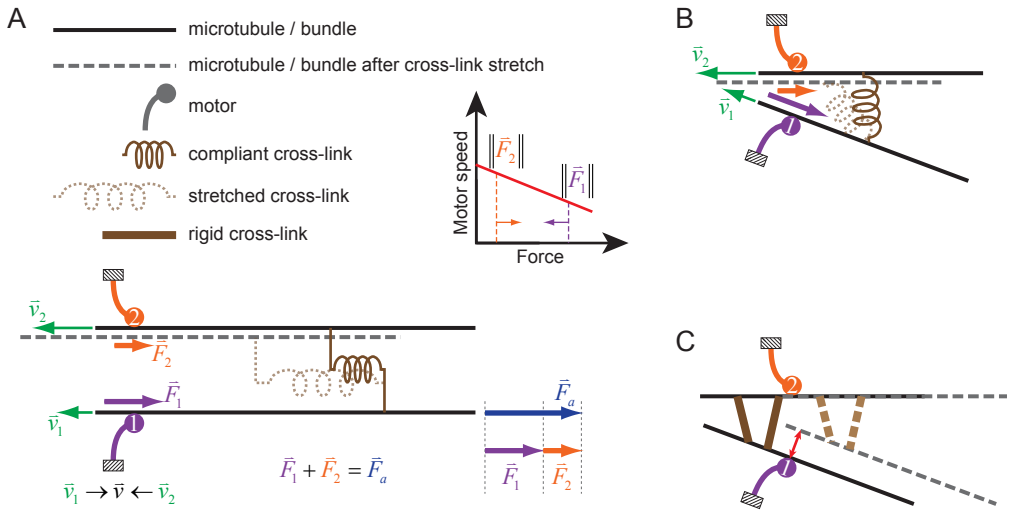

Figure 3.4: Model explaining the effect of cross-link stiffness on force distribution at spindle poles. (A) Force distribution and velocity coordination for parallel microtubules. When $\vec{F}_{\mathrm{a}}$ is applied, motor 1 (purple) must sustain initially $\vec{F}_1 \approx \vec{F}_{\mathrm{a}}$, slowing the motor as determined by its force-velocity relationship. The unloaded microtubule does not change speed, but as the cross-link stretches and therefore transmits more force, some of $\vec{F}_{\mathrm{a}}$ is distributed via the cross-link to motor 2 as $\vec{F}_2$, which relieves some of the load on motor 1: $\left\|\vec{F}_1\right\| < \left\|\vec{F}_{\mathrm{a}}\right\|$. This slows motor 2 and speeds motor 1 so that the two approach roughly the same speed. Motors and compliant cross-links are shown as distinct entities for simple depiction of force transfer; the concept is not changed if motors also act as cross-links. (B) Nonparallel microtubules. As in the parallel case, force is transmitted via the cross-link. The component of force transmitted parallel to the microtubule increases if the angles between the cross-link and microtubules decrease, which occurs with increasing load. Note that for clarity the angle is greater than would typically be observed for adjacent microtubules. However, the concepts depicted here and in panel C also apply for indirectly cross-linked microtubules, which are found at all angles across the spindle pole. (C) Rigidly cross-linked microtubules. With sufficient rigid crosslinking, the relative positions of all microtubules are fixed. Microtubules move with the same speed and direction, and geometric constraints prevent motors from walking along microtubules while remaining fixed. The structure cannot rearrange to accommodate mitotic phenomena such as flux unless the cross-links are transient relative to the rate at which motors move, in which case they transmit less force and therefore distribute a smaller amount of the load from one microtubule to another.

tained by one microtubule or bundle in a half-spindle is potentially augmented by motors on neighboring microtubules, with the amount of force transfer diminishing for microtubules more distantly separated in the spindle.

In this context, earlier estimates of spindle forces should be reconsidered. A maximum force of 750 pN (±50%) was estimated by Nicklas [1983] using a flexible glass microneedle to stall the poleward movement of an individual chromosome in anaphase in *Melanoplus* spermatocytes, which is 10,000 times that required to overcome viscous drag. Microtubule flux is the dominant mechanism for poleward movement of chromosomes during anaphase in *Melanoplus* spermatocytes [Chen and Zhang, 2004], so the slowing of chromosomes by an opposing load is most simply explained by slowing poleward flux. Because the forces on spindle microtubules will be distributed among the force generators responsible for flux, the numbers obtained by Nicklas [1983] may reflect an integrated force, perhaps reflecting the force that the half-spindle produces to move multiple chromosomes.

3.3 Conclusion

These findings describe microtubule attachments to asters in a mammalian mitotic extract as compliant and dynamic, with individual microtubules anchored by a small number of motors and nonmotors to maintain the overall structure while accommodating and driving microtubule movements. Such a structural framework is consistent with recent work from Gatlin et al. Gatlin et al. [2010] who found that although poles are densely cross-linked structures, they are compliant enough to let a spearing microneedle pass through them.

A similar theme is suggested at the spindle midzone in the proposal in Subramanian et al. [2010] that the protein PRC1 uses dynamic, compliant cross-linking of microtubules at the spindle midzone to balance structural rigidity with the flexibility needed to allow microtubule sliding by kinesin-5 motors. Thus, we envision that this

dynamic, compliant mechanical architecture may not be restricted to the polar region of spindles but is used throughout spindles to distribute forces needed for steady-state assembly and chromosome movement. We anticipate that future studies of the mechanics of spindle components, including poles containing centrosomes, may reveal dynamic compliant linkages as a central theme within the mitotic spindle, which must maintain mechanical integrity without impeding pervasive dynamic movements.

For further recommended future work, please see section 7.2.1.

CHAPTER IV

Background: Microtubule structure and polymerization dynamics

This chapter* provides background relevant the chapter on variability of microtubule growth rate (Chapter VI). Microtubules assemble from heterodimeric subunits; the present work takes monomer to mean either α or β-tubulin, discussing polymerization in terms of association and dissociation of subunits.

4.1 Introduction

As introduced in section 1.2, microtubules exhibit dynamic instability, in which they alternate between phases of slow growth and rapid shortening. According to the GTP-cap hypothesis, the transition from growth to rapid shortening, termed catastrophe, is due to the loss of a stabilizing cap of GTP-tubulin subunits (Fig. 1.5, p. 8). The phases and transitions of dynamic instability have profound biological significance, as reflected by their extensive regulation *in vivo* by numerous microtubule associated proteins (MAPs) that are implicated in various diseases [reviewed by Amos and Schlieper, 2005; Howard and Hyman, 2007]. Rapid microtubule length

*Small portions of this chapter are taken nearly verbatim from Charlebois et al. [2010] and from a typescript that was accepted for publication and corresponds to Gardner et al. [2011] and Chapter VI.

changes allow tasks such as cytoskeletal reorganization and mitosis. Underscoring their importance to mitosis, microtubule polymerization dynamics are the target of important anticancer drugs [reviewed by Jordan and Wilson, 2004].

The four parameters typically used to specify dynamic instability are growth rate, $\hat{v}_{\mathrm{g}}$; rapid shortening rate, $\hat{v}_{\mathrm{s}}$; catastrophe frequency, f_{cat}; and rescue frequency, f_{res}. (However, the probability of catastrophe per unit time is a function of how long the microtubule has been growing Odde et al. [1995].) Table 4.1 lists results from several studies of the modulation of dynamic instability. Neither rigorous nor exhaustive, it is intended only to summarize some of the effects that have been observed. Microtubule associated proteins (MAPs) may, for example, cap, sever, polymerize, or depolymerize microtubules, track the growing tip of a microtubule, nucleate microtubule growth, sequester free tubulin, or some combination thereof, but simple ions can also have a pronounced effect on microtubule polymerization.

Table 4.1: Examples of modulation of plus-end dynamic instability

Substance	$\hat{v}_{\mathrm{g}}$	$\hat{v}_{\mathrm{s}}$	f_{cat}	f_{res}	reference
Mg^{2+}	$\uparrow$	$\uparrow$	$\otimes$	$\otimes$	O'Brien et al. [1990]
Ca^{2+}	$\otimes$	$\uparrow$	$\uparrow$		O'Brien et al. [1997]
Tau	$\uparrow$	$\downarrow$	$\downarrow$		Drechsel et al. [1992]
Doublecortin	$\otimes$	$\downarrow$	$\downarrow$		Moores et al. [2006]
Op18/stathmin pH	$\downarrow$	$\downarrow$	$\uparrow$		Howell et al. [1999]
XMAP215	$\uparrow$		$\downarrow$		Kinoshita et al. [2001]
EB1	$\uparrow$	$\downarrow$	$\uparrow$	$\uparrow$	Vitre et al. [2008]
Cls1p (CLASP)	$\uparrow$	$\downarrow$	$\downarrow$	$\uparrow$	Al-Bassam et al. [2010]

$\uparrow$ denotes an increase, $\downarrow$ denotes a decrease, and $\otimes$ indicates authors concluded there was no effect. This table oversimplifies the effects of the substances it describes and is intended only to provide a rough overview. For instance the effect of Op18/stathmin on $\hat{v}_{\mathrm{g}}$ is pH-dependent, and the effects of some MAPs differ, for instance, by organism. In some cases, effects were markedly different at the minus end. Differences in polymerization dynamics may also arise from, for instance, changes in β-tubulin isotype composition and post-translational modifications.

Elucidation of the mechanisms of action of MAPs and microtubules *in vivo* depends on an understanding of the basic phenomenon of microtubule assembly from

purified tubulin *in vitro* which, in turn, is informed by the structure of $\alpha\beta$-tubulin and its incorporation into the microtubule lattice.

4.2 Microtubule structure

4.2.1 $\alpha\beta$-tubulin

The structure of tubulin has been obtained from electron crystallography of zinc-induced taxol-stabilized sheets of antiparallel protofilaments [e.g., Lowe et al., 2001; Nogales et al., 1998] combined with cryoelectron microscopy images of microtubules [e.g., Li et al., 2002], and also from crystal structures of $\alpha\beta$-tubulin in complex with a stathmin-like domain and a drug [e.g., Ravelli et al., 2004].

The folds of α and β tubulins are similar and can be divided into several functional domains. Nogales et al. [1998] describe the tubulin fold as "a core of two β-sheets surrounded by α-helices" (a core helix, H7, is between these two sheets) and specify three functional domains (see also Fig. 4.1): an N-terminal nucleotide-binding domain containing loops believed to be oriented toward the lumen, an intermediate domain containing loops believed to mediate some lateral contacts as well as taxol binding, and a C-terminal domain believed to be involved in inter-monomer interactions and MAP and motor binding. The nucleotide-binding site is oriented toward the microtubule plus end and is believed to have its nucleotide exchange blocked by the next plus-proximal α- or β-tubulin. In the case of β-tubulin, GTP hydrolysis is believed to be enabled by residues of the α-tubulin of the next plus-proximal subunit along the protofilament [Amos, 2004; Nogales and Wang, 2006]. The final C-terminal residues (13 in α- and 9 in β-tubulin) are apparently disordered [though reported observable by Wang and Nogales, 2005] acidic residues that are assumed to project into solution [Amos, 2004]. This corresponds to part of the "E-hook" of tubulin.

The E-hook of tubulin is a negatively-charged C-terminal region (roughly 10-

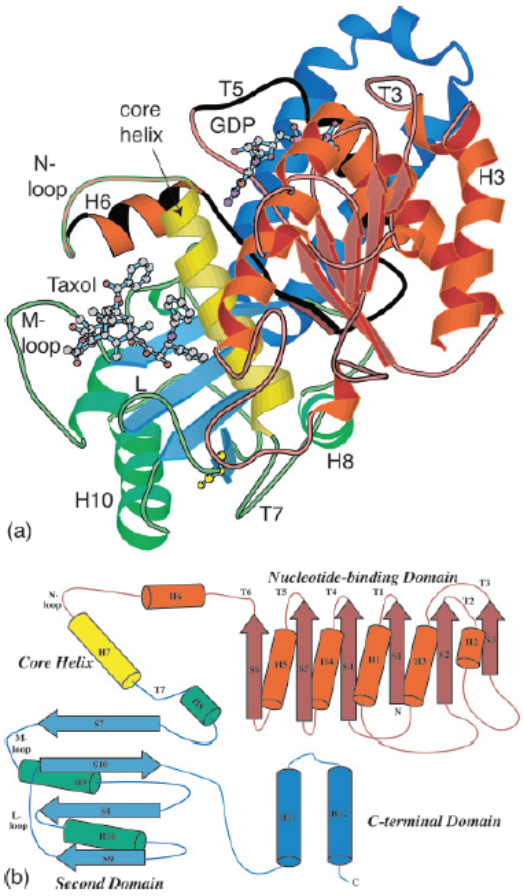

Figure 4.1: Structure of β-tubulin. (a) Ribbon diagram and (b) domain organization of β-tubulin. The N-terminal domain binds the guanine nucleotide. A core helix, H7, is between the two β-sheets. The M-loop, which interacts with taxol when bound, is believed to be involved in lateral interactions. Further description is in the main text. Figure from Amos [2004].

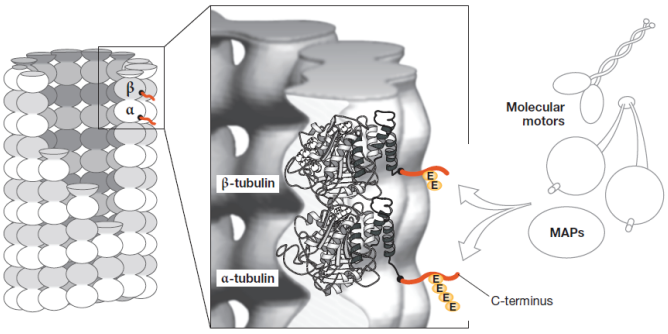

Figure 4.2: The E-hook and post-translational modification. The E-hook (red lines), which is rich in glutamate (E) residues, is believed to be disordered and to project into solution. It has been implicated in motor and microtubule-associated protein (MAP) function and is a site of post-translational modification. For instance, post-translational polyglutamylation of glutamate residues near the C-termini of α- and β-tubulins by reversible addition of up to to $\sim$20 glutamyl units (orange ovals marked "E") is especially common in the microtubules of neurons, centrioles, axonemes, the mitotic spindle and (in cytokinesis) the midbody [reviewed by Janke et al., 2008]. Figure from Janke et al. [2008]

25 C-terminal residues rich in Glu and Asp) implicated in the function of motors and MAPs, including the diffusion of some MAPs on the microtubule lattice [e.g., Brouhard et al., 2008; Helenius et al., 2006; Hertzer and Walczak, 2008; Lakämper and Meyhöfer, 2005]. The C-terminal region of tubulin is a source of variability among microtubules; its sequence varies across isotypes and it is the site of multiple post-translational modifications [Westermann and Weber, 2003], a notable exception being acetylation of several Lys residues [Choudhary et al., 2009]. In addition to the E-hook, calculations indicate that large portions of the microtubule exterior and lumen are at negative electrostatic potential, with some positive regions [Baker et al., 2001].

Lateral (protofilament-protofilament) interactions are crucial to the present work based on the predictions of a model introduced in section 4.3.1.2 (p. 64). Lateral interactions are believed to be mediated by several loops. The M loop [Li et al., 2002; Nogales et al., 1999; Sui and Downing, 2010] of one subunit may interact with the N

(H1-S2) loop [Li et al., 2002] in addition to the S2-H3 loop [Sui and Downing, 2010] of a lateral neighbor. Li et al. [2002] noted that the N loop contains residues that vary among β-tubulin isotypes, suggesting it might contribute to differences in dynamics and drug sensitivity among isotypes. Lowe et al. [2001] also noted that residues involved in longitudinal interactions are better conserved than those involved in lateral interactions. In microtubules with 11 to 16 protofilaments, lateral interactions appear to be mediated in part by M loops on the microtubule luminal wall, and there are opportunities for salt-bridge formation [Sui and Downing, 2010], though one of these appears to correspond to a salt-bridge that formed only in the presence of taxol in molecular dynamics simulations [Mitra and Sept, 2008].

The nature of subunit-subunit interactions has been investigated in a computational study of energetic contributions due to electrostatics and burying of solvent-accessible surface area [Sept et al., 2003]. Longitudinal translation of protofilaments relative each other revealted two energy minima. These corresponded to A- and B-type joins, with the latter more energetically favorable. The two minima could be explained by solvent-accessible surface area contributions, but the preference for B-type joins was found to be largely due to electrostatic contributions. Furthermore, longitudinal interactions were found to be stronger than lateral interactions, which is consistent with the VanBuren et al. [2002] simulations of subunit exchange kinetics introduced in section 4.3.1.3. It is the lateral and longitudinal bonds that allow assembly of subunits into the microtubule lattice.

4.2.2 Microtubule lattices

The 13-protofilament microtubule lattice (Figs. 1.3, 4.3) can be described as a left-handed 3-start helix in which no distinction is made between α and β monomers [Desai and Mitchison, 1997; Howard, 2001]. The helix pitch is 12 nm. Here, "n-start" indicates that n starts are required to complete the lattice; following the helical path

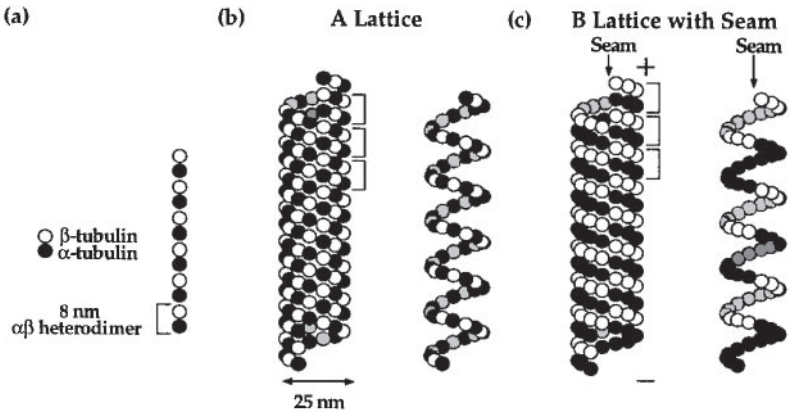

Figure 4.3: The 13-protofilament microtubule lattice. (a) Tubulin dimers stacked end to end constitute a protofilament. (b) Hypothetical A-type lattice in which lateral (protofilament-protofilament) interactions are between α- and β-tubulins. In both (b) and (c), the left-hand image shows the full lattice, while the right-hand image shows one of the 3 helical paths required to complete the lattice, emphasizing where lateral interactions are α-α, α-β, and β-β. (c) Physiological B-type lattice. Along the seam, protofilaments are said to have "A-type" joins. Figure from Desai and Mitchison [1997].

from one protofilament to the next for one rotation around the microtubule will result in arrival n monomers down the starting protofilament. Along most of this helical path, stepping from one protofilament to the next involves stepping from an α-tubulin to another α or from β to β, and the subunits are said to have B-type lateral joins. However, since following the helical path results in arrival 3 monomers down (1.5 subunits down) the starting protofilament, there must be a pair of protofilaments between which the join is α-β or *vice versa*, termed an A-type join (more precisely, the number of A-type joins must be odd) [Desai and Mitchison, 1997; Howard, 2001].

Microtubules with number of protofilaments, N_{PF}, from 8 to 20 and with several numbers of starts have been reported [references in Sui and Downing, 2010]. The distribution of N_{PF} for microtubules formed by spontaneous nucleation *in vitro* depends on conditions [e.g., Chrétien and Wade, 1991; Ray et al., 1993] and is typically 13 or 14, while microtubules *in vivo* usually have 13 [Desai and Mitchison, 1997]. (A no-

table exception is in *Caenorhabditis elegans*, in which 15-protofilament microtubules are present in touch-receptor neurons and 11-protofilament microtubules are present in other cells [Chalfie and Thomson, 1982].) Cells control N_{PF} by, for instance, nucleation from centrosomes. Also, the microtubule tip tracker EB1 has been reported to promote 13-protofilament microtubules *in vitro* and to reduce transitions between N_{PF} values along the microtubule [Vitre et al., 2008].

The ability of microtubules to accommodate a range of N_{PF} can be explained in part by the lattice rotation model [Chrétien and Wade, 1991; Howard, 2001]; protofilaments, rather than aligning parallel to the microtubule axis, follow a helical path around the microtubule, termed a supertwist, with a pitch typically of a few µm (the motor kinesin will follow this path [Ray et al., 1993]). Because of this supertwist, the local geometry experienced by a subunit is similar over a range of protofilament numbers [Howard, 2001], though there appears to be an energetic preference for less supertwist under standard assembly conditions (80 mM PIPES and 1 mM each of EGTA, $MgCl_2$, GTP) [Chrétien and Fuller, 2000].

Increased N_{PF} also increases microtubule radius, requiring flexibility in the interactions between protofilaments. Cryoelectron microscopy results for 11- to 16-protofilament microtubules (Fig. 4.5) found lateral interactions were similar for this range, but larger N_{PF} may introduce new lateral contacts [Sui and Downing, 2010].

The multi-protofilament structure of microtubules allows them to grow to substantial lengths; a single-protofilament "microtubule" would tend to sever in the middle by dissociation of a single (longitudinal) bond, and the association of a free subunit with another free subunit would be more favorable than with long polymer, resulting in short microtubules even at subunit concentrations far above the critical concentration [Howard, 2001]. In a multi-protofilament polymer such as a microtubule or F-actin, each subunit not at an end binds to multiple neighbors; for the polymer to be severed or to lose subunits other than at its ends would require multiple bonds

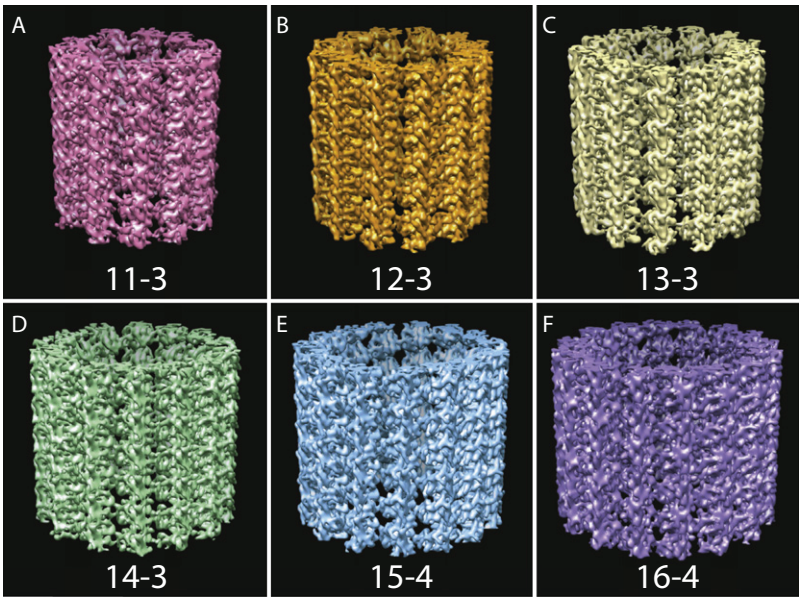

Figure 4.4: Microtubule lattices with different numbers of protofilaments. These models are based on cryoelectron microscopy data combined with 2D electron crystallography data. N_{pf}-n indicates number of protofilaments and number of starts (e.g., 13-3 indicates a 13-protofilament 3-start helix). All lattices other than 13-3 have supertwist. Figure from Sui and Downing [2010].

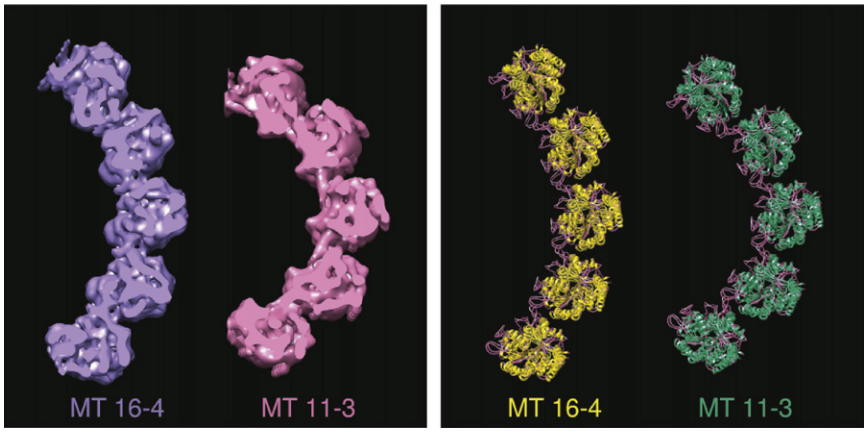

Figure 4.5: Effect of lattice changes on lateral interactions. End-on cross-sections based on reconstructions from electron microscopy images show that a 4-start 16-protofilament microtubule may have additional lateral interactions relative to a 3-start 11-protofilament microtubule (both in the presence of taxol, which is believed to affect lateral contacts). Figure from Sui and Downing [2010].

to be broken. The expected average length is much longer [Howard, 2001]. (*In vivo*, enzymes sever F-actin [dos Remedios et al., 2003] and microtubules [Roll-Mecak and McNally, 2010].)

Having discussed $\alpha\beta$-tubulin and its arrangement in the microtubule lattice, the next natural topic leading to polymerization is the microtubule tip. However, the next section focuses on protofilament and subunit curvature, which are relevant to observed tip structures and also to the proposal that GDP tubulin in the microtubule lattice is a strained torsional spring that would be unstable in the lattice were it not for the GTP cap (section 1.2.2) [reviewed by Nogales and Wang, 2006; Nogales et al., 2003].

4.2.3 Protofilament and subunit curvature

For rapidly shortening microtubules grown from purified tubulin, pronounced curvature of protofilaments at the tip (ram's horns) away from the microtubule axis has been observed [e.g., Mandelkow et al., 1991; Müller-Reichert et al., 1998], though this depends on conditions [e.g., see also Arnal et al., 2000; Höög et al., 2011]. This suggests that rapid shortening is correlated with a change in intra-subunit or inter-subunit angle (or both). For growing microtubules, protofilaments near the tip have also been observed to curve away from the microtubule axis (section 4.2.4, p. 58).

That GTP-tublin is straighter that GDP-tubulin is suggested by several studies. For instance, Müller-Reichert et al. [1998] prepared microtubules with GTP (i.e., having a predominantly GDP lattice) or the slowly-hydrolyzable GTP analog GMPCPP, which assumed to keep subunits in a GTP-like state. They depolymerized these microtubules by cold treatment or addition of Ca^{2+} and observed them by cryoelectron microscopy, finding that the GDP microtubles had curved protofilaments at their ends and that GMPCPP reduced this curvature. A similar atomic force microscopy study yielded similar curvatures, estimating angle changes per α or β monomer along

the protofilament of 8° with GMPCPP and 12° with GDP [Elie-Caille et al., 2007]. In addition, the authors found that taxol initially results in very straight protofilaments, but that these become curved on a timescale of many hours. In a cryoelectron microscopy study of unusual assemblies of tubulin, Wang and Nogales [2005] concluded that GDP tubulin is more curved and much more flexible than GTP tubulin. Higher flexibility would enable GDP-tubulin to adopt conformations farther from its preferred conformation, but would presumably reduce the depolymerization force per unit angular distortion. The view that emerges is that GTP- and GDP-tubulin have intrinsic curvature and are strained in the microtubule lattice, but GDP-tubulin is more strained, leading to its destabilization of the lattice.

4.2.4 Structures at the tips of growing microtubules

Three key features of the microtubule tip (Figs. 4.6, 4.9) have implications for models of microtubule growth (section 4.3). First, the protofilaments may end at roughly the same axial position (blunt tip) or a group of adjacent protofilaments may form a sheet extension (tapered tip). Assumptions about tip bluntness are implicit in models for microtubule growth that provide the basis for calculations of subunit kinetics (on and off rates; section 4.3.1.2, p. 64). Second, protofilaments at the tip may coincide with the cylinder defined by the bulk of the microtubule or they may curve away from the protofilament axis. Curvature is important to models relating hydrolysis and catastrophe. Third, GTP- and GDP-tubulins may be distributed in various configurations near the tip. This section focuses on the first two properties, leaving the third to section 4.3.2 (p. 71).

Studies of microtubules grown from purified tubulin [Chrétien et al., 1995; Mandelkow et al., 1991; Vitre et al., 2008] or in cell-free *Xenopus* egg extracts [Arnal et al., 2000] using cryoelectron microscopy or in *Schizosaccharomyces pombe* cells using electron tomography [Höög et al., 2011], usually combined with light microscopy

to establish dynamics under the conditions in question, have provided substantial data on bluntness and curvature. Terminology describing tip structure below is as described in Fig. 4.6.

Evidence of tapering and curving at the tip is moderately contradictory. Mandelkow et al. [1991] found that microtubules under growth-phase conditions were 60% blunt, 36% clearly tapered (with 72% of these less than 50 nm), and 4% coiled (presumably rapidly shortening). The authors did not focus on the curvature of the tapered ends, but some curvature is apparent in their images, particularly for the longer tapered ends. Other studies have observed curved tapered ends, some in the hundreds of nm long [Arnal et al., 2000; Chrétien et al., 1995; Vitre et al., 2008] or, in contrast, predominantly curved and relatively blunt ("flared") tips as observed from multiple angles by tomography [Höög et al., 2011].

Chrétien et al. [1995] found that tapering was more pronounced with increasing tubulin concentration, with some sheet extensions exceeding 1 µm under some conditions. Sheet extensions tended to curve away from the microtubule axis, and in some cases two sheets extended from one tip. Development of tapering over time was quantified, with some evidence that tips become more tapered during initial growth and then begin to become less tapered. This was observed more recently in the control for a study of the microtubule tip-tracking protein EB1 [Vitre et al., 2008].

Bluntness has been suggested to correlate with catastrophe. For instance, Op18 / stathmin promoted both catastrophe and blunt ends when added to *Xenopus* egg extracts [Arnal et al., 2000]. Results with EB1, though more complicated due to EB1's multiple effects, also suggest a correlation [Vitre et al., 2008]. In contrast, simulations have predicted the opposite [VanBuren et al., 2005], and the above mentioned Höög et al. [2011] tips were curved, relatively blunt, and growing. The mean length of the outwardly curved portion was 18 nm, corresponding to roughly two layers of subunits. Tapered tips (sheets) were rare, not exceeding 3% under any of the conditions, and

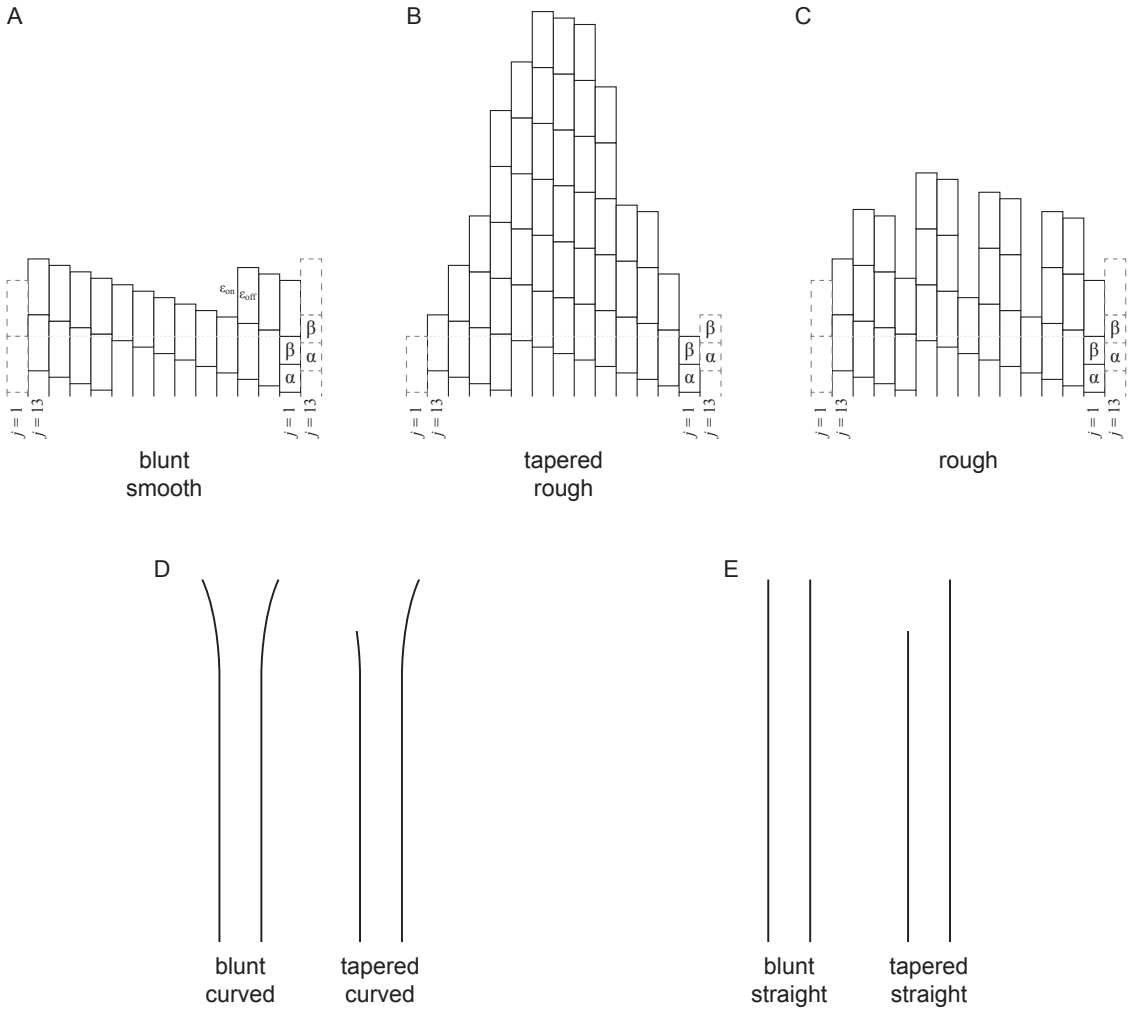

Figure 4.6: Terminology for microtubule tips. The seam is between protofilaments $j = 1$ and $j = 13$. (A) A blunt tip has all protofilaments ending at nearly the same position. The subunit marked ε_{off} may be said to be in the "cozy corner," in which case the vacancy marked ε_{on} would be the "cozy corner" for a new subunit addition. (B) A tapered tip has protofilaments of varying length forming a sheet extension. Roughness, which will be discussed in section 4.3.1.2 (p. 64), is a measure of the number of free lateral interactions exposed, so this tapered tip has higher roughness than the blunt, smooth tip. (C) A tip with roughness similar to (B) that might appear in an experiment to resemble (A). (D) Curved protofilaments at the tip. (E) Straight protofilaments at the tip.

they were, on average, an order of magnitude shorter than those observed by Arnal et al. [2000] in *Xenopus* extracts. Blunt straight ends were also rare. The authors interpreted the predominance of flared tips to indicate that in *S. pombe* protofilaments have "little or loose lateral interaction," though presumably they might also tend to form, for instance, moderately stable pairs or triplets, ensuring mutual stabilization of protofilaments, perhaps sometimes with a gap between them as in Fig. 4.6C. The effect of MAPs at growing tips in cells is presumably complex, so it is difficult to predict whether microtubules grown from purified tubulin would exhibit similar behavior.

4.3 Microtubule polymerization

For growth-phase microtubule polymerization, the tip is assumed, until catastrophe, to be approximately equivalent to polymerization without GTP hydrolysis. This implies that the presence of GDP-tubulin at or near the tip of any protofilament can be neglected. The subunit exchange at the tip of a growth-phase microtubule is important to models of the GTP cap, catastrophe, and rescue, as well as modulation by MAPs and drugs. This section begins with a discussion of microtubule polymerization neglecting hydrolysis, followed by a short discussion of the effects of hydrolysis. Table 4.2 summarizes symbols used to represent key physical quantities.

4.3.1 Growth-phase polymerization

Polymer subunits such as G-actin or $\alpha\beta$-tubulin under suitable conditions and in the absence of nucleotide hydrolysis are expected to polymerize in three phases: spontaneous nucleation, growth, and polymer size redistribution [Oosawa, 1970]. This section focuses on one end of the polymer in the growth phase, which is most relevant to the present work, beginning with the model typically applied to microtubule growth.

Table 4.2: Nomenclature for microtubule polymerization dynamics with typical units

Variable name	Units	Meaning
k_{B}	pN nm / K	Boltzmann's constant
T	K	absolute temperature
[Tub]	µM	free tubulin concentration
N_{PF}	-	number of protofilaments
v_{g}	s^{-1}	net growth rate, subunits/time
$\hat{v}_{\mathrm{g}}$	$\mu\mathrm{m\,min}^{-1}$	net growth rate, distance/time
v_{s}	s^{-1}	rapid shortening rate, subunits/time
$\hat{v}_{\mathrm{s}}$	$\mu\mathrm{m\,min}^{-1}$	rapid shortening rate, distance/time
f_{cat}	min^{-1}	frequency of catastrophe
f_{res}	min^{-1}	frequency of rescue
$k_{\mathrm{off,PF}}$	s^{-1}	off rate per protofilament
$k_{\mathrm{off,MT}} \equiv N_{\mathrm{PF}} k_{\mathrm{off,PF}}$	s^{-1}	off rate per microtubule
$k_{\mathrm{on,PF}}$ or $k_{\mathrm{on,MT}}$	$\mu\mathrm{M}^{-1}\,\mathrm{s}^{-1}$	on rate constant per protofilament or per microtubule
$k^{*}_{\mathrm{on,MT}} \equiv k_{\mathrm{on,MT}}[\mathrm{Tub}]$	s^{-1}	on rate per microtubule
$k^{*}_{\mathrm{on,PF}} \equiv k_{\mathrm{on,PF}}[\mathrm{Tub}]$	s^{-1}	on rate per protofilament
$k^{(i)}_{\mathrm{off,PF}}$	s^{-1}	off rate for a subunit with i lateral neighbors (2D models)
$\Delta G_{\mathrm{Lateral}} < 0$	pN nm	free energy of lateral interaction per subunit
$\Delta G^{*}_{\mathrm{Longitudinal}} < 0$	pN nm	free energy of longitudinal interaction and immobilization per subunit
$\Gamma \equiv e^{-\Delta G_{\mathrm{Lateral}}/k_{\mathrm{B}}T}$	-	for certain assumptions, off rate increase upon loss of a lateral interaction (2D models)

Furthermore, $k_{\mathrm{off,MT}}$ is used as the off rate in the 1D model (section 4.3.1.1 on p. 63) and as the mean off rate in 2D models (section 4.3.1.2 on p. 64; Appendix B on p. 148). Free energy under standard conditions is denoted with a superscript zero, and this use is clarified in Appendix B, p. 148.

4.3.1.1 Classic Oosawa 1D model

The net growth rate, $\hat{v}_{\mathrm{g}}$, of a microtubule is proportional to the difference between subunit association and subunit dissociation rates. Oosawa [1970], in a study based on theory from macromolecular chemistry, assumed that dissociation occurs at a constant rate $k_{\mathrm{off,MT}}$ and that association occurs at a rate $k^{*}_{\mathrm{on,MT}} \equiv k_{\mathrm{on,MT}}[\mathrm{Tub}]$ where [Tub] is the concentration of free subunits, yielding

$$\hat{v}_{\mathrm{g}} = a(k_{\mathrm{on,MT}}[\mathrm{Tub}] - k_{\mathrm{off,MT}}) \tag{4.1}$$

where $a = \frac{8\,\mathrm{nm}}{N_{\mathrm{PF}}}$ is the mean length increase per subunit added [†] , giving $\hat{v}_{\mathrm{g}}$ dimensions of length per time. The association of one subunit, Tub, onto the end of a microtubule, MT, is the reaction

$$\mathrm{MT} + \mathrm{Tub} \underset{k_{\mathrm{off,MT}}}{\overset{k_{\mathrm{on,MT}}}{\rightleftharpoons}} \mathrm{MT},$$

for which the reaction quotient is $[\mathrm{Tub}]^{-1}$, so that

$$\Delta G_{\mathrm{subunit}} = \Delta G^{0}_{\mathrm{subunit}} + k_{\mathrm{B}}T \ln [\mathrm{Tub}]^{-1}, \tag{4.2}$$

where $\Delta G_{\mathrm{subunit}}$ and $\Delta G^{0}_{\mathrm{subunit}}$ are the free energy change for subunit addition under, respectively, the conditions in question and standard conditions.

At equilibrium, the free subunit concentration is said to be at the critical concentration, C_{c}, and there is no net growth: $\hat{v}_{\mathrm{g}} = 0$ and $[\mathrm{Tub}] = C_{\mathrm{c}}$. Also, $\Delta G_{\mathrm{subunit}} = 0$. The equilibrium constant is $K_{\mathrm{eq}} = C_{\mathrm{c}}^{-1} = k_{\mathrm{on,MT}}/k_{\mathrm{off,MT}} = e^{-\Delta G^{0}_{\mathrm{subunit}}/k_{\mathrm{B}}T}$. The off rate can be obtained by rearrangement:

$$k_{\mathrm{off,MT}} = k_{\mathrm{on,MT}} e^{\Delta G^{0}_{\mathrm{subunit}}/k_{\mathrm{B}}T} \tag{4.3}$$

[†]Considering the geometry of the microtubule lattice, the length increase for a given subunit association will depend on the definition of the microtubule "end" and on the protofilament to which the subunit associates. Futhermore, different experimental techniques may effectively impose different definitions of the microtubule end [Howard and Hyman, 2009].

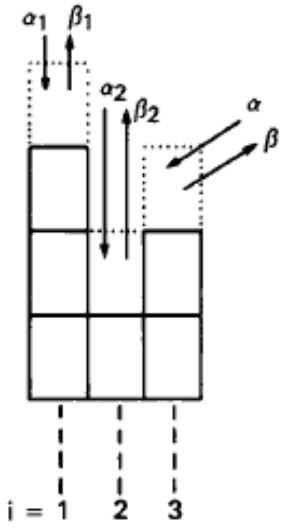

Figure 4.7: Rate constants as depicted by Hill. Rate constants (Hill used α, β, α_1,...) for a given subunit depend on the surroundings of that subunit. Considering a zero-start 3-protofilament helix (implicitly wrapped into a tube so that the leftmost and rightmost protofilaments are in contact), a subunit at the tip may have 0, 1, or 2 lateral neighbors with different rate constants for each case. Figure from Hill [1986].

4.3.1.2 Hill 2D model

The above Oosawa model assumes that all subunit association events are kinetically equivalent to each other and that, similarly, all subunit dissociation events are kinetically equivalent to each other. However,

> "...if a polymer has several strands [protofilaments], it will also have several on and off sites at an end [see Fig. 4.7], with associated fluctuating rate constants that depend on the instantaneous arrangement of subunits at the end... Such polymers will have average overall on and off rate constants but these rate constants will, in general, *not* be constant: they will depend on free subunit concentration..." Hill [1987]

One might expect that this kinetic equivalence assumption would be most reasonable if lateral interactions were very weak; however, arguing against this is the expected importance of lateral interactions to formation of long polymers (end of sec-

tion 4.2.2). Very weak lateral interactions would result in protofilaments that grow independently of each other, producing extreme differences in protofilament length (see discussion of equation B.2, p. 149). The large number of single-protofilament extensions from the tip would eliminate the lateral interactions that prevent the microtubule from severing. The assumption suggested by Hill [1987] for effectively-1-protofilament models is that the tip structure is always configured such that the practically significant association site is always the same and, similarly, the practically significant dissociation site is always the same. There may be multiple such sites at a time, but a hypothetical single-site growth phenomenon is what might be termed "helical growth" or "cozy-corner growth" at the tip of a 3-start 13-protofilament microtubule that is always (neglecting the seam) as blunt and smooth as that depicted in Fig. 4.6A (p. 60): Only the subunit with zero lateral neighbors would have a practically significant off rate, and only the vacancy next to this subunit would have a practically significant on rate.

Arguing against effectively-1-protofilament microtubule models is the range of experimentally observed tip structures (section 4.2.4). Hill [1986], considering differences in association/dissociation kinetics at different sites, provided a framework for predicting how tip structure and overall off rate should, in general, depend on [Tub]. Appendix B (p. 148) follows Hill's framework for one case, adapting the nomenclature to the present work. Key points of Hill's work follow:

1. Surface roughness is a key property of a given tip configuration. Hill defined (equation B.3, p. 150) an index of the surface roughness (molecular roughness) of the tip (Fig. 4.6, p. 60) as a measure of the number of subunits with exposed lateral surface area. More exposed area corresponds to more surface free energy and, therefore, a less energetically favorable tip configuration.

2. The equilibrium probability of one tip configuration relative to another is a function of the difference in their surface free energies, which is proportional

to the difference in their surface roughnesses. Tip configurations with identical roughness are equally probable. Exposed longitudinal surface also contributes to free surface energy, but not to differences in free surface energy from one tip configuration to another. The free energy of a lateral subunit-subunit interaction relative to $k_{\mathrm{B}}T$ determines the distribution of tip structures of varying roughness because it relates differences in exposed surface to differences in surface free energy.

3. Increasing [Tub] (a departure above the critical concentration) will increase surface roughness. This is supported by the Chrétien et al. [1995] observation of increasing tip taper with increasing with [Tub]. One could think of this as vaguely related to the law of mass action, in which increasing a reactant (tubulin) drives the reaction toward energetically unfavorable products (rough tips). Alternatively, one can consider an initially rough tip at [Tub] near zero: preferential dissociation of subunits not having lateral neighbors will result in a blunt, smooth tip.

4. Surface roughness is also related to dissociation rate. A tip with very low roughness will have a relatively low dissociation rate, though the roughness-$k_{\mathrm{off,MT}}$ relationship is not simple. Increasing [Tub] should increase surface roughness and, in turn, dissociation rate, in contradiction to the assumption of the Oosawa 1D model described in the preceding section.

5. Based on Hill's analytic and simulation work, neither the overall on rate nor the overall off rate can be assumed, in general, to be proportional to [Tub]. However, if subunit association is assumed to be diffusion limited and not, for instance, inhibited by neighboring protofilaments it may be appropriate to assume that the on rate is proportional to [Tub] and is independent of the number of lateral neighbors.

As noted in section 4.2.1, tubulin residues involved in longitudinal contacts are highly conserved while those involved in lateral contacts are less well conserved [Lowe et al., 2001]. If these sequence differences change the free energy of lateral interaction, the surface roughness of microtubules growing from purified tubulin isoforms might allow experimental estimation of isoform-specific free energy of lateral interaction. However, estimating surface roughness from, for instance, cryoelectron microscopy/tomography or fluorescence images has not been established. Chapter VI (see especially equation 6.7 on p. 108 along with equations 6.10 and 6.11) provides a method for experimental estimation of mean exchange rates, which could potentially be used with simulations to obtain interaction energies.

A change in longitudinal bond energy would be predicted to affect the dissociation rate for all subunits at the tip by the same factor, regardless of the number of neighbors each has.

4.3.1.3 Simulations based on the 2D model

The 2D simulations of VanBuren et al. [2002] are key to the interpretation of experimental data in Chapter VI. This section briefly describes early simulations by Chen and Hill before describing those of VanBuren and colleagues.

Hill [1986] computed mean surface roughness as a function of [Tub] and $\Delta G_{\mathrm{Lateral}}$. He obtained values analytically or by Monte Carlo simulation for 4 types of lattice. Surface roughness had little dependence on [Tub] for $-\Delta G_{\mathrm{Lateral}}/k_{\mathrm{B}}T > 4$. Considering the value of $\Delta G_{\mathrm{Lateral}}$ obtained by more recent computational work (Table 4.3 on p. 69, discussed below), one might assume surface roughness has weak dependence on [Tub]. However, Hill [1986] did not use realistic geometry, focusing on 2- or 3-protofilament models, as well as a staggered 5-protofilament model. For these, there might be fewer possible rough configurations similar to Fig. 4.6B or C (p. 60) or to the taper sometimes observed experimentally (section 4.2.4). Lattice geometry may

therefore have caused an underestimation of the importance of considering lateral interactions.

Chen and Hill [1985] performed Monte Carlo simulations of 5-start 13-protofilament microtubules in which GTP hydrolysis was incorporated but in which only helical growth was allowed (no changes in surface roughness). These studies form the basis for subsequent work by VanBuren et al. using updated geometry and a clever approach for obtaining longitudinal and lateral interaction energies.

VanBuren et al. [2002], performing 2D simulations of 13-protofilament microtubules rooted in previous work by Hill (and used in section 6.2.4, p. 97), screened for reasonable values of the free energies of lateral interaction[‡] $\Delta G^0_{\text{Lateral}}$ and longitudinal interaction $\Delta G^{0*}_{\text{Longitudinal}}$, where * indicates the term incorporates the entropic penalty of subunit immobilization. They assumed a constant on rate per protofilament, $k_{\text{on,PF}}$[Tub], and determined the off rate for every subunit in the lattice based on the total free energy change for dissociation. For subunits not at the tip, they included in this the free energy of lateral bonds experienced by subunits above it (toward the tip), and dissociation of a non-tip subunit resulted in dissociation of subunits above it.

For each variable-length time step of the simulation, the rate k_E for each potential association or dissociation event E was computed, and the actual time t_E for the potential event to occur was determined from $t_E = -k_E^{-1} \ln(R_E)$ where $0 < R_E < 1$ was a uniformly distributed random number. The event with the smallest t_E was selected for each timestep. The authors constrained $\Delta G^0_{\text{Lateral}}$ and $\Delta G^{0*}_{\text{Longitudinal}}$ to pairings yielding $\hat{v}_{\text{g}}$ in agreement with experiment. Varying [Tub] narrowed results to a single pairing. Table 4.3 lists values obtained assuming two values of $k_{\text{on,PF}}$ (A and B), along with the average of values used in Chapter VI (case C). Fig. 4.8 demonstrates the sensitivity to $\Delta G^{0*}_{\text{Longitudinal}}$ and $\Delta G^0_{\text{Lateral}}$ of $k^{(i)}_{\text{off,PF}}$, where i is the

[‡]The superscript zero denotes standard conditions, but [Tub]does not affect the free energy of lateral association. Implicitly, $\Delta G^0_{\text{Lateral}} = \Delta G_{\text{Lateral}}$.

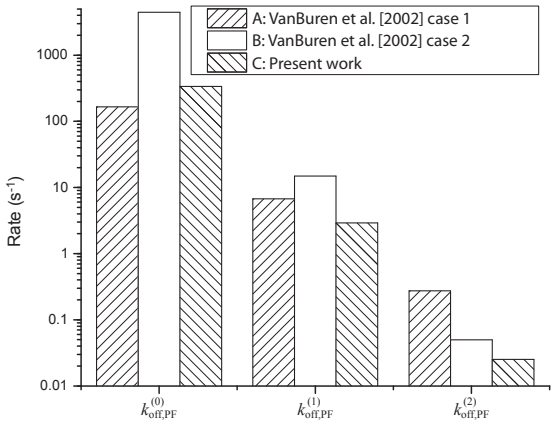

Figure 4.8: $k^{(i)}_{\mathrm{off,PF}}$ values used in VanBuren simulations. The off rate for a subunit with i lateral neighbors, $k^{(i)}_{\mathrm{off,PF}} = k_{\mathrm{on,PF}} e^{\left(\Delta G^{0*}_{\mathrm{Longitudinal}} + i\Delta G^{0}_{\mathrm{Lateral}}\right)/k_{\mathrm{B}}T}$, is calculated from values in Table 4.3, in which the cases A, B, and C correspond to those of this figure. Kinetics are sensitive to energetics of interaction.

number of lateral neighbors. These simulations also took into account the possibility of a subunit at the seam having a half neighbor. Additional results of this study and a subsequent study [VanBuren et al., 2005] are relevant to the GTP cap.

Table 4.3: VanBuren model $k_{\mathrm{on,PF}}$, $\Delta G^{0}_{\mathrm{Lateral}}$, and $\Delta G^{0*}_{\mathrm{Longitudinal}}$values

Case	$k_{\mathrm{on,PF}}$ ($\mu\mathrm{M}^{-1}\,\mathrm{s}^{-1}$)	$\frac{\Delta G^{0}_{\mathrm{Lateral}}}{k_{\mathrm{B}}T}$	$\frac{\Delta G^{0*}_{\mathrm{Longitudinal}}}{k_{\mathrm{B}}T}$	$\frac{k^{(0)}_{\mathrm{off,PF}}}{k^{(1)}_{\mathrm{off,PF}}} = \frac{k^{(1)}_{\mathrm{off,PF}}}{k^{(2)}_{\mathrm{off,PF}}}$
A	2	-3.2	-9.4	2.5×10^1
B	4	-5.7	-6.8	3.0×10^2
C	4.5	-4.75	-9.5	1.2×10^2

Cases A and B are those used by VanBuren et al. [2002], who obtained 1D-model $k_{\mathrm{on,MT}}$ estimates of a few $\mu\mathrm{M}^{-1}\,\mathrm{s}^{-1}$ from the literature. Values indicated are based on what appears to be the more likely of two possible interpretations of their publication. Case B was also used in Schek et al. [2007]. Case C is the average value used in Chapter VI in which parameters were obtained by a different method. See also Fig. 4.8 and Table 6.2 (p. 103).

4.3.1.4 Experimental observation of growth-phase kinetics

The above Oosawa 1D model yields equation (4.1) (p. 63), which has provided adequate fits to experimental $\hat{v}_{\mathrm{g}}$ *vs.* [Tub] data, Table 6.1 on p. 91); the model has

therefore been assumed to be realistic model of microtubule growth, and the fitting parameters have yielded estimates of $k_{\mathrm{on,MT}}$ and $k_{\mathrm{off,MT}}$.

Studies have generally estimated $k_{\mathrm{on,MT}}$ well below the diffusion limit as estimated by Northrup and Erickson [1992] and discussed, for instance, by Brouhard et al. [2008]. This low $k_{\mathrm{on,MT}}$ can be taken to imply an activation barrier that limits the fraction of diffusion-based subunit-tip encounters that result in subunit association [e.g., Northrup and Erickson, 1992]. For instance, from this, to explain $\hat{v}_{\mathrm{g}}$ increases due to the MAP XMAP215, Brouhard et al. [2008] postulated a transition state that can be stabilized by the MAP XMAP215 in order to reduce the activation barrier. XMAP215 also catalyzes the reverse reaction.

Several experimental observations suggest the growth-phase $k_{\mathrm{off,MT}}$ is appreciable. Schek et al. [2007] observed large growth-phase shortening events, and such events can also be found in the Kerssemakers et al. [2006] data. Needleman et al. [2010], adding exogenous labeled tubulin to meiotic *Xenopus* extracts at low labeling ratio, observed fast subunit exchange in the spindle. Because they were observing individual subunits in a sample of dense microtubules they interpreted their data in terms of a phenomenological model with multiple possible interpretations [described in Mirny and Needleman, 2010]. The fit to their data, extrapolated to time intervals perhaps 10 to 50 times shorter than they measured, would predict that many subunits would have shorter lifetimes than Oosawa-1D-model-based rates would allow.

A key feature of microtubule growth that the Oosawa 1D model fails to predict is variability in growth rate. To predict growth rate variability, the observation $k_{\mathrm{off,MT}} \ll (k_{\mathrm{on,MT}}[\mathrm{Tub}])$ for the practical range of [Tub] allows the simplifying assumption[§] that microtubule growth results mainly from subunit association events, with little competition from dissociation. Over a given time interval Δt, the number of associations λ_+ should be Poisson distributed, in which case the mean should equal

[§](The more general case in which association events and dissociation events are taken into account is explained in the discussion of Fig. 6.1, p. 94.)

the variance:

$$\langle \lambda_+ \rangle = \left\langle \lambda_+^2 \right\rangle - \langle \lambda_+ \rangle^2 .$$

From this, one can predict the variance in microtubule growth rate. Experiments have consistently measured growth rates far more variable than the Oosawa model would predict.

Several possible causes of the variability in microtubule growth rate have been eliminated. For instance, experimental error was eliminated as a source, and individual microtubules exhibited as much variability as the entire population, eliminating differences among microtubules as the source [Gildersleeve et al., 1992]. Based on a GMPCPP study, GTP-hydrolysis did not account for $\hat{v}_{\mathrm{g}}$ variability [Dye and Williams, 1996]. A more quantitative assessment relating variability to growth rate confirmed previous results [Pedigo and Williams, 2002].

Howard and Hyman [2009] suggested that high variability in growth rate may result from subunit exchange at the tip being more rapid than has been estimated, with net growth resulting from relatively large association and dissociation rates. This, combined with the above-described results suggesting a high dissociation rate or fast exchange, along with the argument of Hill [1986] that dissociation rate should depend on [Tub], motivates the experiments of Chapter VI. The remainder of this chapter provides a brief description of the effects of GTP hydrolysis.

4.3.2 Polymerization with nucleotide hydrolysis

Upon incorporation of a GTP-subunit into the lattice, the rate of GTP hydrolysis by that subunit increases. It is thought that this increase occurs when the next vacancy of the same protofilament becomes occupied; the nucleotide-binding domain of β-tubulin is oriented such that the α-tubulin of the next plus-proximal subunit, when present, is thought to block nucleotide exchange and stimulate hydrolysis [Amos, 2004].

The number of GTP subunits the cap must have to stabilize the microtubule is unclear. For instance, two studies concluded that 13 GMPCPP subunits are necessary and sufficient to stabilize a GDP lattice [Caplow and Shanks, 1996; Drechsel and Kirschner, 1994]. Simulations in which most protofilaments started with a 4-GTP-subunit cap suggested uncapping 4 protofilaments can still yield growth [VanBuren et al., 2005].

The value to which the hydrolysis rate increases would determine (along with subunit exchange kinetics) cap size (Fig. 4.9). Cap size has been estimated experimentally to be small [e.g., references in Schek et al., 2007], suggesting GTP hydrolysis occurs quickly upon subunit incorporation. However, microtubules have been observed to shorten during the growth phase, sometimes by amounts corresponding to more than 5 layers Schek et al. [2007] (also visible in the data of Kerssemakers et al. [2006]) without undergoing catastrophe, suggesting a finite hydrolysis rate and a distributed GTP cap. Simulations suggest a hydrolysis rate of roughly $1\,\mathrm{s}^{-1}$ supports growth consistent with experiment and a mean cap size of 55 subunits (s.d. 12), while very fast hydrolysis prevents growth due to frequent catastrophe [VanBuren et al., 2002].

The use of a constant catastrophe frequency per unit time is at odds with experimental evidence that the probability of catastrophe was not constant over time, with catastrophe unlikely in the early stages of growth: Odde et al. [1995] found catastrophe tended to occur after 0.5 to 4 minutes (6 µM tubulin, plus end). The amount of time that a microtubule plus end grew before catastrophe was gamma-distributed, which can be interpreted to mean that catastrophe is the result of a sequence of first-order transitions. Data were consistent with 3 such transitions (occurring at about 1.7 per minute) being required for catastrophe. This implies tip properties indicate how long the microtubule has been growing, and this information travels with the tip as the microtubule grows. Presumably, explaining this result will require an improved understanding of the kinetics of subunit exchange and GTP hydrolysis, of the devel-

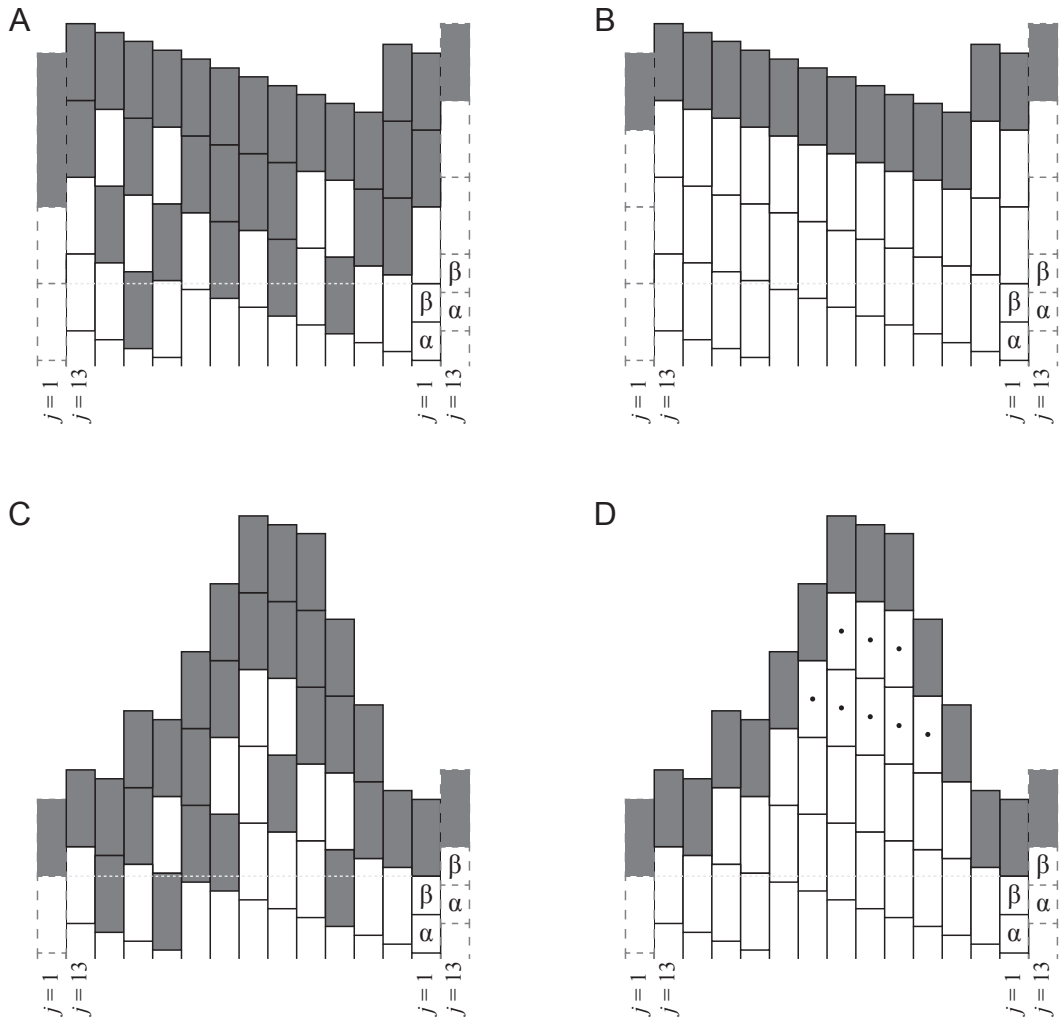

Figure 4.9: Examples of potential GTP cap distributions. GTP-tubulin (dark) caps the primarily GDP-tubulin (light) lattice. The seam is between protofilaments $j = 1$ and $j = 13$. The tip is blunt (A,B) or tapered (C,D). Upon subunit incorporation, the hydrolysis rate increase is (A,C) modest, yielding a distributed cap or (B,D) large, yielding a single layer of GTP. Considering (D), if the tapered portion of the tip were allowed to bend away from the microtubule axis, and if this were to reduce the hydrolysis rate (i.e., if straightening stabilized the transition state of the hydrolysis reaction [Howard, 2001; Wang et al., 2007]), the subunits marked with dots might also contain GTP. This possibility, which is independent of whether hydrolysis is tightly coupled, is supported by very limited evidence, but it is discussed briefly in Chapter VII

opment of tip structure over time, and of the effects of GTP hydrolysis on subunits and the lattice. Underscoring our limited understanding are several studies that are difficult to explain with available data.

Co-polymerization of GDP- and GTP-subunits into the microtubule lattice [Valiron et al., 2010] appears to slow the rates of growth, $\hat{v}_{\mathrm{g}}$, and rapid shortening, $\hat{v}_{\mathrm{s}}$, relative to that in the absence of free GDP-subunits. The decrease in $\hat{v}_{\mathrm{s}}$ suggests that GDP-subunits incorporated by co-polymerization differ from those that originally incorporated as GTP-subunits. Cryoelectron microscopy did not reveal obvious effects on the lattice from co-polymerization, indicating differences in lattice configuration or subunit conformation are relatively subtle. Co-polymerization and transitions between conformations could be speculated to be facilitated by higher flexibility of GDP-tubulin relative to GTP-tubulin observed in unusual assemblies of tubulin [Wang and Nogales, 2005], with conformational transitions faster in solution than in the lattice.

Using antibody-recognition of GTP-subunits in the lattice in cells, Dimitrov et al. [2008] observed apparent GTP remnants in the predominantly GDP bulk lattice, and these correlated with rescue events. These remnants may have been the result of MAPs. The antibody may have been recognizing subunits in which hydrolysis was inhibited, or it may have been recognizing a conformation normally adopted by GTP subunits but occasionally adopted by GDP-subunits [Kueh and Mitchison, 2009]. In the latter case, such a conformation might be similar to that which slowed $\hat{v}_{\mathrm{s}}$ in the Valiron et al. [2010] study.

The next chapter describes a method for observation of microtubule polymerization dynamics at high spatiotemporal resolution. This is followed by a results chapter that supports the above-mentioned 2D model.

CHAPTER V

Nanometer-Resolution Microtubule Polymerization Assays Using Optical Tweezers and Microfabricated Barriers

This chapter* describes one of the experimental techniques used in Chapter VI. This technique was originally demonstrated by Schek et al. [2007].

Addition and loss of one or a few subunits cannot be observed at the spatiotemporal resolution of conventional microscopy, and requires development of approaches with higher resolution. Here we describe an assay in which one end of a microtubule (MT) abuts a barrier, and MT length changes are coupled to the movement of an optically trapped bead, the motion of which is tracked with high resolution. We detail assay execution, including preparation of the experimental chamber and orientation of the MT against the barrier. We describe design requirements for the experimental apparatus and barriers, and preparation of materials including stable, biotinylated MT seeds from which growth is initiated and NeutrAvidin®-coated beads. Finally, we discuss advantages of moving the optical trap such that it applies a constant force (force clamping), detection limits, the importance of high temporal resolution, data analysis, and potential sources of experimental artifacts.

*This chapter is largely identical to Charlebois et al. [2010].

5.1 Introduction

Most direct characterization of microtubule (MT) dynamics, focusing on rates of growth, shortening, and transitions between growth and shortening, has been by light microscopy (e.g., [Chrétien et al., 1995; Dye and Williams, 1996; Gildersleeve et al., 1992; Horio and Hotani, 1986; Jordan et al., 1993; Odde et al., 1996; Walker et al., 1988]), and this approach continues to yield valuable insights into MT dynamics and their modulation (e.g., [Bieling et al., 2007; Brouhard et al., 2008; Helenius et al., 2006; Moores et al., 2006; Pedigo and Williams, 2002]). However, conventional light microscopy allows observation of MT length changes corresponding to the addition or loss of hundreds of subunits. At standard video rate, the temporal resolution is, at best, on the order of the time between subunit additions or losses, though recent data suggest subunit exchange is much more rapid [Schek et al., 2007]. Rates of growth and shortening thus represent an average over many addition or loss events. Observing one or a few such events to unequivocally determine molecular-scale details requires much higher spatiotemporal resolution.

Nanometer-resolution measurements of events resulting from MT dynamics has recently been achieved with the development of assays using optical tweezers (e.g., [Asbury et al., 2006; Grishchuk et al., 2005; Kerssemakers et al., 2006; Schek et al., 2007]; reviewed in [Gardner et al., 2008a]), including those in which the tweezers are used to polymerize an MT into a barrier and track MT length changes [Kerssemakers et al., 2006; Schek et al., 2007], yielding important new insights into MT polymerization dynamics. For instance, on short (hundreds of ms) timescales, growth rates were directly measured to be highly variable and, even during periods of net growth, sometimes negative [Kerssemakers et al., 2006; Schek et al., 2007], with growth-phase shortening events that correspond to the loss of several layers of subunits [Schek et al., 2007].

5.2 Rationale

To observe MT polymerization with sufficient spatiotemporal resolution to detect addition or loss of one or a few 8-nm subunits, MT length changes can be measured by coupling them to the movement of an object whose position can be tracked at high resolution: in this case, a bead held by optical tweezers. The MT-linked bead is trapped, and the MT is oriented such that it abuts a suitably designed barrier (Fig. 5.1A–C). Because MTs are relatively rigid, growth or shortening at the end of the MT abutting the barrier will result in bead movement, which can be tracked with high precision using interferometry or video processing. The trap position can be held fixed [Kerssemakers et al., 2006], or it can be moved such that applied force is constant [Schek et al., 2007], which is termed force clamping. Here we focus on our force-clamp assay [Schek et al., 2007], but note advantages of other approaches [Kerssemakers et al., 2006].

5.3 Methods

The assay entails constructing an experimental chamber, flowing in the experimental solution including NeutrAvidin®-coated beads coupled to biotinylated MT seeds (short, stable MTs from which growth can be initiated), trapping an MT-linked bead, orienting the MT against a barrier (Figs. 5.1, 5.2), and collecting position data. Microfabrication of barriers on glass coverslips is described elsewhere [Schek and Hunt, 2005], and here we focus on execution of the assay.

A coverglass patterned with barriers microfabricated from LOR and SU-8 (MicroChem, Newton, MA) photoresist layers (Fig. 5.1C, section 5.4 on p. 81) is cleaned with, in succession, methanol, ethanol, isopropanol, 0.1% sodium dodecyl sulfate (SDS), and purified water. This is incorporated into an experimental chamber using two aluminum foil spacers, each with a thin coating of vacuum grease, to position

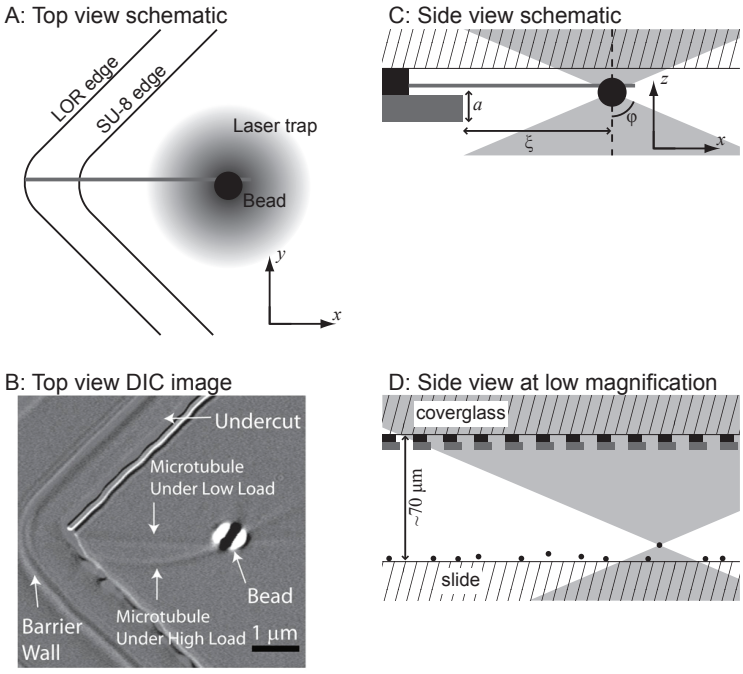

Figure 5.1: Assay overview and experimental geometry. (A) Schematic top view. The microtubule (gray) tip is constrained in the y direction by the vertex of the LOR photoresist wall, which also blocks movement or growth in the negative x direction. The microtubule is pushed toward the barrier by the laser trap via the bead. A force-clamp feedback loop can move the laser trap along the x-axis such that the force on the bead is constant, in which case microtubule length changes result in corresponding trap movement. This image is after Schek et al. [2007], Fig. 1. (B) Differential interference contrast image corresponding to (A). An image of the microtubule when buckled is superimposed on the image of the microtubule under low load, demonstrating that the microtubule tip remains constrained over a range of forces. Reprinted from Schek et al. [2007]. (C) Schematic side view. The laser propagates in the negative z direction. The undercut of the LOR layer (black) allows the SU-8 layer (gray) and coverglass (hatched) to constrain the microtubule tip in the z direction. The focus of the trapping laser beam (gray triangles), which is slightly above the bead center (not shown), is a distance a above the bottom of the SU-8 layer in the z direction and a distance ξ from the SU-8 edge in the x direction. If ξ approaches $\sqrt{2}a\tan(\varphi)$ (assuming the barrier edge is 45°from the x axis), the laser will be clipped by the barrier. This image is after Schek and Hunt [2005], Fig. 1. (D) Schematic side view at lower magnification. Beads sink to the bottom of the experimental chamber, which is ∼70 µm below the coverglass. Positioning the trap at increasing depth impairs trapping due to spherical aberration and interference of the laser with photoresist structures.

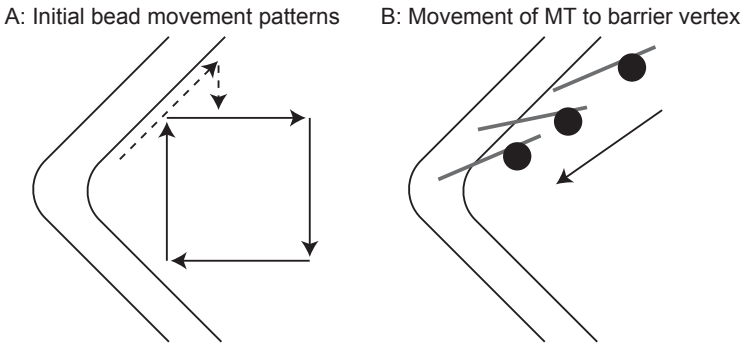

Figure 5.2: Orienting an MT in the barrier. (A) Initial bead movement patterns. The bead is moved, for instance, in a square pattern (solid arrows) or along the barrier edge and then toward the center in the y direction (dashed arrows) to keep the MT in the focal plane and orient it as shown in (B). (B) Movement of MT into barrier vertex. The MT is maneuvered into the undercut and along the barrier edge toward the vertex. Final orientation should be similar to that of Fig. 5.1A.

the coverglass a small distance (~70 µm) above the slide. The foil spacers are spaced about 6mm apart to create an experimental flow chamber with barriers on the upper surface, and open ends such that fluids may be introduced by capillary action. Thin spacing must be maintained between the coverglass and slide: because our microscope is upright, we use silica beads (Section 5.4), which sink to the bottom of the chamber where they must be initially trapped (Fig. 5.1D); however, with increasing depth, the beam profile of the trapping laser is increasingly impaired by spherical aberration and by passage through the photoresist structures that form the barriers above (Fig. 5.1D). This can be partially remedied by patterning barriers at a reduced surface density or by increasing power of the trapping laser when searching for a bead.

Before introducing the experimental mixture, buffer is flowed into the experimental chamber, and if any areas exclude liquid this is remedied by gently pressing the coverglass. Because beads spontaneously aggregate, they are separated by passage through a 25-G needle several times immediately before the experiment. Following this shearing, several chamber volumes of the experimental mixture (buffer, beads, stable MT seeds, free tubulin, MAPs, and MT-binding drugs as applicable) are flowed

into the experimental chamber, which must then be sealed to prevent drying and drying-induced fluid flow during experiments; we use VALAP (a 1:1:1 mixture of Vasoline, lanolin, and paraffin), which is melted and brushed onto the ends of the chamber. The chamber is then quickly moved to the microscope, and a single free bead is trapped. To determine whether one or more MT seeds are attached to a given trapped bead, the bead is moved laterally relative to the buffer by moving the trap or microscope stage to bring an MT into the focal plane (the trap is positioned such that the bead is held in the imaging focal plane).

A bead with an MT seed is moved to the vicinity of a barrier and oriented appropriately (Fig. 5.2). The bead can be moved in a pattern (Fig. 5.2A) that keeps the MT in the focal plane and orients its plus end near an edge of the barrier (Fig. 5.2B), at which point the bead can be moved such that the MT moves into the undercut and down the barrier edge to the vertex. The MT tip must be located at the barrier vertex and constrained by the undercut (Fig. 5.1A–C), at which point applying the force clamp will push the MT against the barrier. From this point onward, trap movements required to maintain constant force correspond to changes in MT length.

To establish whether the plus end or the minus end is in the barrier, the growth of both ends is observed by light microscopy. If experimental conditions require a relatively low growth rate, the investigator may more easily determine MT polarity by inducing high growth at the end of an experiment by flowing in buffer with a high tubulin concentration. An alternative approach for establishing MT polarity is to substitute axonemes for seeds, as MTs preferentially grow from the plus ends of isolated axonemes. These provide tighter control over protofilament number and allow the MT to be oriented using a keyhole trap [Kerssemakers et al., 2006].

5.4 Materials

All chemicals are obtained from Sigma-Aldrich (St. Louis, MO) unless otherwise specified.

5.4.1 Buffer

We perform experiments in BRB-80 [80 mM pipes, 1 mM$MgCl_2$, 1 mM ethylene glycol tetraacetic acid (EGTA), pH 6.8]. Because MT growth [Khan and Luduena, 1991] and flexural rigidity [Mickey and Howard, 1995] are influenced by the oxidation state, we supplement the buffer with oxygen scavengers: 0.12 mg/mL catalase, 0.6 mg/mL glucose oxidase, 30 mM glucose, and 2 mM dithiothreitol. We also supplement buffer with an additional mM $MgCl_2$ per mM of guanine nucleotide.

5.4.2 Experimental Apparatus

The optical tweezers apparatus [Brouhard et al., 2003; Schek and Hunt, 2006; Visscher and Block, 1998] should have several features. First, it should detect bead position with high spatiotemporal resolution using, for instance, back-focal-plane interferometry (BFPI) [Gittes and Schmidt, 1998b]. High temporal resolution allows thermal noise to be suppressed by filtering, which improves spatial resolution (see section 5.5). Second, the apparatus should be able to apply a time-averaged constant force (force clamp) by moving the trap, which has several advantages (section 5.5), including tracking MT length changes over a larger range and minimizing the effect of force on results. Finally, it should allow simultaneous light microscopy appropriate for visualizing MTs, such as video-enhanced differential-interference contrast (VE-DIC) microscopy. For VE-DIC, contrast enhancement, background subtraction, and frame averaging can be achieved with a Hamamatsu ARGUS (Hamamatsu Photonics, Hamamatsu City, Japan) or with equivalent commercial or custom digital image acquisition and processing. The setup should ideally simultaneously process and record

video at 30Hz, allowing the user to record MT movement while observing it in real time.

5.4.3 MT Length Constraints: Applied Force and Barrier Design

The MT used for the experiment must be short enough that it will not buckle under the trapping force [Schek and Hunt, 2005]. The force at which a segment of MT buckles under compression is proportional to its flexural rigidity and inversely proportional to the square of its length, and has been estimated at 2 pN for a 10-µm MT [Gittes et al., 1993], though smaller values have been measured (e.g., [Kikumoto et al., 2006; Kurachi et al., 1995]). The length of MT between the bead and barrier in our experiments is generally ~5 µm.

The MT must also be long enough that the experiment can be conducted without impairing measurements of the bead position [Schek and Hunt, 2005]. The geometry of both the barrier and laser beam must be considered (Fig. 5.1C). The laser must not pass through photoresist upstream of the trap, as this would change the beam profile, thereby introducing an error in the applied force. In the case of BFPI detection, the laser beam should not pass through photoresist downstream of the trap either, since this affects the bead position measurement. Relatively thin layers of photoresist allow the assay to be conducted with the trap closer to the barrier. The effect of the barriers on the trap and bead detection at a given position can be determined experimentally by performing a power spectrum calibration [Gittes and Schmidt, 1998a]: if the power spectrum is Lorentzian and the parameters yielded by the calibration are consistent with those obtained in the absence of barriers, then the effect of the barrier on measured bead position is negligible.

5.4.4 Preparation of Biotinylated MT Seeds

For taxol-stabilized seeds, 50 µM tubulin and 1 mM GTP in buffer (see above) are incubated at 37°C for 25 min, brought to 10µM taxol, and immediately vortexed. These MTs are centrifuged (Beckman Airfuge; Beckman Coulter, Brea, CA), the supernatant is discarded, and the pellet is rinsed and resuspended in BRB-80 with 10 µM taxol. Biotin succinimidyl ester (B1606; Invitrogen Corporation, Carlsbad, CA) is added at 1.7 mM, and the sample is incubated at 37°C for 15 min. To quench the reaction, three volumes of 400 mM glycine (in BRB-80) are added, followed by an additional 10 min of incubation. The sample is centrifuged, the supernatant is discarded, and the pellet is rinsed and resuspended in BRB-80 without taxol. It is then sheared several times through a 30-G needle. Finally, in order to deplete taxol, the seeds are centrifuged, rinsed, and resuspended two more times in buffer. The resulting seeds should be ~2 µm long. The amount of free biotin in the experimental solution must be minimal, as it may compete with seeds for NeutrAvidin®-binding sites.

For guanylyl-(α,β)-methylene-diphosphonate (GMP-CPP; NU-405S; JenaBioscience, Jena, Germany) stabilized seeds, the above protocol is altered as follows. The initial tubulin concentration is 2 µM to reduce spontaneous MT nucleation [Hyman et al., 1992]. The 1 mM GTP is replaced with 0.2 mM GMP-CPP (this five-fold reduction in concentration reduces expense). Only one centrifugation is performed after shearing.

For experiments in which a relatively low polymerization rate is expected, seeds can be made longer by adjusting the shearing protocol (e.g., see [Farrell et al., 1987; Melki et al., 1993; Williams and Rone, 1989; Yamauchi et al., 1993]), or short seeds can be elongated before the experiment by incubating with tubulin (pulsed if necessary). Seeds will anneal to form longer MTs over longer time periods (hours). We generally begin a day of experiments by making seeds and stop collecting data when the seed concentration and length are no longer appropriate.

5.4.5 Preparation of NeutrAvidin®-Coated Beads

A solution of ~0.6-µm silica beads (SS03N; Bangs Laboratories, Fishers, IN) at 10 mg/mL in BRB-80 is sonicated and vortexed (a few minutes each), and 20 $\mu g\,mL^{-1}$ biotin–BSA is added, followed by 5 min of vortexing. The beads are then centrifuged. The supernatant is discarded and the pellet is rinsed three times with BRB-80 gently and without resuspension. It is then resuspended in 10 times the original volume (~1 mg/mL beads) and vortexed. This solution is brought to 20 $\mu g\,mL^{-1}$ NeutrAvidin® (A2666, Invitrogen) and vortexed gently for 5 min. During this step, a low bead concentration reduces the chances of NeutrAvidin® binding two biotinylated beads to each other. The beads are centrifuged, the supernatant is discarded, and the pellet is rinsed and resuspended in the original volume (~10 mg/mL beads). The beads are centrifuged, rinsed, and resuspended three additional times. Silica beads will slowly sediment, so when making aliquots, the beads should be mixed frequently to ensure all aliquots have roughly the same concentration. Aliquots are flash-frozen in liquid nitrogen and stored at –80°C.

Most beads should be attached to zero, one, or occasionally two seeds, and the concentration of bead–seed complexes must be low enough to prevent the formation of networks of beads and seeds. In the experimental solution, we generally use taxol-stabilized biotinylated seeds at ~1/50 dilution and beads at ~1/80 dilution, but these quantities vary significantly.

5.5 Discussion

Here we discuss advantages of force clamping, approaches to data analysis, assessment of detection limits, and potential sources of artifacts.

5.5.1 Advantages of Force Clamping

In contrast to stationary-trap experiments, a force-clamp experiment [Finer et al., 1994; Gittes and Schmidt, 1998a; Visscher and Block, 1998] uses a feedback loop in which the trap is moved in response to changes in the bead position such that the time-averaged force is constant. This offers several advantages. In a stationary-trap experiment, the MT lengthens against the barrier, pushing the bead from the trap center. Data collection terminates when the MT pushes the bead out of useable range of the trap or force becomes high enough to buckle the MT or induce a catastrophe. Also, because the force changes with bead movement, its effect on MT polymerization dynamics is variable. With force clamping, data can be collected over a much larger range of displacement because the trap moves to accommodate bead movement, and the force can be tightly controlled as an experimental variable or kept low to minimize its effect on polymerization dynamics. Also, stationary-trap data underestimates MT growth because MT displacement is partially accommodated by stretching of the bead–MT linkage. The stiffness of the bead–MT linkage must be obtained to correct this underestimation [Kerssemakers et al., 2006], and this can be challenging due to nonlinear compliance and variability of compliance between bead–MT complexes [Svoboda et al., 1993; Visscher and Block, 1998]. Force clamping obviates the need to correct for this compliance [Visscher and Block, 1998]; it maintains a constant stretch of the bead–MT linkage so that changes in bead position directly correspond to changes in MT length [Schek et al., 2007].

5.5.2 Data Analysis: Bead Position Relative to Trap Center

The raw bead position data allow assessment of force-clamp performance and can allow detection of events that occur more quickly than the force clamp responds. Although the position of the bead can be detected at kHz frequencies with subnanometer precision using techniques such as BFPI [Gittes and Schmidt, 1998b], much of

the high-frequency movement is due to thermal motion, and must be filtered to obtain a precise estimate of MT length changes. Applying a low-pass filter yields a good signal-to-noise ratio and allows examination of events occurring on a timescale longer than the reciprocal of the filter cutoff frequency (see "Detection limits" below). To minimize phase distortion, forward–backward filtering may be appropriate (e.g., [Gustafsson, 1996]).

Bead position data also allow forces experienced by the bead and MT to be assessed. For instance, if the bead is subjected to a combination of thermal, Hookean, and drag (proportional to velocity) forces, the power spectrum of the bead position versus time trace will be Lorentzian and will yield spring constants and damping coefficients [Gittes and Schmidt, 1998a]. In addition to allowing the stiffness of the optical trap to be verified, this type of analysis can identify artifacts resulting from, for instance, the MT becoming stuck to the barrier, or the laser beam being clipped by a barrier.

5.5.3 Data Analysis: MT Length Changes

A subunit addition will change MT length by 0–8 nm: given the 13 protofilament lattice structure of an MT, addition of a single subunit increases the MT length by at most 8 nm if the subunit adds to the leading protofilament, and various smaller amounts including no length change if the subunit adds to a lagging protofilament.

Several approaches are available for analysis of length changes. Most simply, length changes Δx and growth rates r are computed for each fixed time interval of length τ. For analysis of the distribution of Δx or r, variance may be of particular interest because the variance of MT growth rate is higher than expected from conventional linear polymer growth theory [Oosawa, 1970], and there has been substantial interest in determining the mechanism behind this (e.g., [Dye and Williams, 1996; Howard and Hyman, 2009; Odde et al., 1996; Pedigo and Williams, 2002]). In cases

where it is difficult to choose an appropriate timescale, τ, of interest a priori, analysis can be repeated for multiple values of τ [Svoboda et al., 1994], an algorithm can be applied that computes growth or shortening rate using time intervals of varying length as it proceeds through the time series [Schek et al., 2007], or a timescale-independent approach such as spectral analysis can be applied [Odde et al., 1996]. To detect repeated displacement events (e.g., steps), the distance between relatively stationary periods can be examined, for example, by forming a pairwise-distance distribution function [Svoboda et al., 1993]. Searches for steps must be approached cautiously however: without fundamental expectations for speed and size of steps to form a null hypothesis, it is difficult to design a statistical test to establish that a noisy data stream contains "steps," and related errors have repeatedly plagued biophysical studies of nanoscale movements. Limits to detection of steps in noisy signals are discussed further in Moffit et al. [Moffitt et al., 2008].

5.5.4 Detection Limits: Forces, Bandwidth, and Resolution

For experiment design and data interpretation, it is crucial to understand the forces to which the bead is subjected: trap, bead–MT linkage, viscous, and thermal. These forces and their implications for detection limits are discussed in detail elsewhere [Gittes and Schmidt, 1998a; Moffitt et al., 2008; Visscher and Block, 1998]. Briefly, in a force-clamp assay, theoretical spatial resolution can be computed, and is predicted to improve with decreasing bead–MT linkage compliance, bead drag coefficient, and filter cutoff frequency used by the force clamp [Gittes and Schmidt, 1998a]. Therefore, resolution may improve with a smaller bead, which should decrease drag and bead–MT compliance due to bead rocking, or with higher applied force, assuming the bead–MT linkage compliance exhibits strain hardening [Svoboda et al., 1993]. Furthermore, high bandwidth facilitates stationary-trap or forceclamp data analysis, in which case filtering may be required to suppress thermal noise and achieve desired

spatial resolution, though at the cost of lowered temporal resolution (e.g., see supplemental material accompanying [Schek et al., 2007]). Temporal resolution is therefore determined by detector bandwidth or by the filter cutoff, and events that cannot be resolved in time will be detected with a delay or, if they do not result in a persistent displacement, will be missed or underestimated: for example, a spike caused by rapid addition and loss of subunits may not be apparent in filtered data, but still be visible in the raw high-bandwidth data.

In addition to theoretical considerations, data should be collected using a control MT in which length changes are suppressed, such as a GMP-CPP-stabilized MT without free tubulin, in order to experimentally assess detection limits and potential artifacts [Schek et al., 2007].

5.5.5 Potential Sources of Artifacts

Several potential sources of artifacts should be considered.

1. An MT may become stuck to a barrier. To verify that this has not occurred, the MT should be pulled slightly (~500 nm) away from the barrier wall at the end of each experiment, and the trace should be inspected for evidence of sticking.

2. If substantial MT nucleation occurs during the experiment (this is easily observed under VE-DIC), the concentration of free tubulin may fall rapidly toward the critical concentration. Nucleation of pure GTP-tubulin is highly cooperative; the rate of nucleation is extremely sensitive to free tubulin concentration (e.g., [Carlier and Pantaloni, 1978; Fygenson et al., 1995; Voter and Erickson, 1984]). Furthermore, nucleation is stimulated in the presence of, for instance, γ-tubulin or γ-tubulin complexes (reviewed in [Job et al., 2003]), taxol (e.g., [Schiff et al., 1979]), certain MAPs (e.g., [Gupta et al., 2009; Moores et al., 2006; Slep and Vale, 2007]), or a slowly-hydrolysable GTP analog such as GMP-CPP [Hyman et al., 1992; Sandoval and Weber, 1980].

3. MT ends other than the one in the barrier may impair measurements. For instance, the end of the MT opposite that under investigation may strike a different wall. Also, an MT that is out of plane, and therefore not visible, may strike the barrier. Data should be inspected for signs that such events occurred (e.g., a drop in thermal movements or movement of the bead in the y direction).

4. Drift may impair measurements. Barrier movement in the x direction due to stage drift may result in underestimation or overestimation of MT growth rates. Depending on the design of the tweezers apparatus, drift in the z direction may affect trap stiffness and bead-position detection sensitivity. It may also change the zero position of the bead detection system, thereby introducing error in the applied force.

5. Small details in the shape of the barriers may cause artifactual length change measurements. With sufficient forces and appropriate barrier design, this can be addressed or avoided: this is discussed in the supplemental material accompanying Schek et al. [2007].

5.6 Summary

We have described an assay for studying MT polymerization dynamics with high spatiotemporal resolution and discussed interpretation of the data. This technique promises to yield a wealth of insights into MT polymerization dynamics and their modulation by MAPs and MT drugs.

CHAPTER VI

Fluctuations in growth rate support a 2D model for microtubule self-assembly kinetics

This chapter* provides evidence that the classic Oosawa 1D model (section 4.3.1.1, p. 63) is an inadequate representation of microtubule assembly kinetics, and that a 2D model [Hill, 1986; VanBuren et al., 2002] (p. 64, p. 148) is a practically significant improvement over the 1D model.

Symbols representing physical quantities match those of Table 4.2 (p. 62).

6.1 Introduction

The tubulin subunit association rate constant, $k_{\mathrm{on,MT}}$ ($\mu\mathrm{M}^{-1}\,\mathrm{s}^{-1}$) and dissociation rate constant, $k_{\mathrm{off,MT}}$ (s^{-1}) have been previously estimated from *in vitro* measurements of the net microtubule assembly rate, v_{g} (subunits/s; with ∼1625 subunits/μm of MT length) as a function of the free tubulin concentration [Tub] (μM) (Table 6.1). These rate constants have been estimated by fitting the microtubule assembly data to the 1D model of Oosawa [1970]. A key, but untested, assumption of this model is that the tubulin subunit dissociation rate is constant regardless of [Tub]. As described

*This chapter is largely identical to a typescript that was accepted for publication [Gardner et al., 2011]. This publication, on which I am second author, is the result of a collaboration described in the acknowledgements (p. iv).

by Hill [1986] (p. 64, p. 148), this assumption cannot be strictly correct since it requires that the microtubule tip structure is on average constant over varying [Tub], which is not thermodynamically tenable. In addition, Chrétien et al. [1995] found experimentally that microtubule tips shift from relatively blunt tip structures at low [Tub] to relatively tapered tip structures at high concentrations. However, the 1D model might still serve as a reasonable approximation if the microtubule tip structure is only weakly dependent on free tubulin subunit concentration. Thus, the canonical view of microtubule polymerization implicitly rests on the assumption that all tubulin subunits at the tip of a growing microtubule are on average energetically similar to one another, so that $k_{\mathrm{off,MT}}$ is independent of [Tub].

Table 6.1: Published $k_{\mathrm{on,MT}}$ and $k_{\mathrm{off,MT}}$ estimates for growing microtubule plus ends

$k_{\mathrm{on,MT}}$ ($\mu\mathrm{M}^{-1}\,\mathrm{s}^{-1}$)	$k_{\mathrm{off,MT}}$ (s^{-1})	Reference
3.9 ± 1.8	25.7 ± 7.1	Engelborghs et al. [1977]
7.2	17	Bergen and Borisy [1980]
1.00 ± 0.36	2.00 ± 0.18	Farrell and Jordan [1982]
4.2	2.3	Carlier et al. [1984]
3.82	0.37	Mitchison and Kirschner [1984]
1.4	—	Gard and Kirschner [1987]
8.9 ± 0.3	44 ± 14	Walker et al. [1988]
6.8	$25 - 30$	O'Brien et al. [1990]
3	0.1	Drechsel et al. [1992]
6.9 ± 0.5	32 ± 6.0	Trinczek et al. [1993]
$*5$	0.1	Hyman et al. [1992]
5.7	14.1	Chrétien et al. [1995]
$*4.9 \pm 2.3$	0.49 ± 0.12	Brouhard et al. [2008]

* denotes use of GMPCPP either at the lowest [Tub][Brouhard et al., 2008] or for the entire data set [Hyman et al., 1992]. Walker et al. [1988] excluded "pause" phase time intervals from their growth-phase data analysis, complicating comparison of their results with those of others, but they report that pauses were rare.

To test whether thermodynamic differences between tubulin subunits at the microtubule tip are important for interpreting growth data, we studied microtubule assembly at near-molecular resolution using total internal reflection fluorescence (TIRF) microscopy, and with our high temporal and spatial resolution nanoscale laser tweezer

assay (Chapter V, [Schek et al., 2007]). To simplify our initial analysis, we inhibited GTP hydrolysis by performing experiments in the presence of the slowly hydrolyzable GTP analogue GMPCPP. Preventing GTP hydrolysis suppressed transitions to rapid shortening that present potentially confounding variables for interpreting microtubule growth dynamics.

By analyzing the variance of the microtubule growth rate v_g at high spatiotemporal resolution, we show that the kinetics of microtubule assembly are much more rapid than previously assumed, even when GTP hydrolysis is inhibited. This data is explained by a 2D model of the tip structure, and interpreted in this context shows that a non-homogeneous tip structure has a significant impact on tubulin subunit dissociation rates from the tip of a growing microtubule. In summary, we show (1) that tubulin subunit dissociation rates $k_{off,MT}$ from the tip of a growing microtubule depend on the [Tub], and (2) that dissociation rates increase substantially at higher [Tub], which requires that growth-phase subunit on-off events occur much more rapidly than previously appreciated. This reassessment of microtubule assembly kinetics leads to a new perspective on microtubule assembly regulation via MAPs and drugs, where weak and infrequent interactions with tubulin subunits at the growing microtubule tip can strongly affect net assembly.

6.2 Results

6.2.1 The 1D Model Predicts Fewer Large Shortening Events at Higher Tubulin Concentration

In a linear (1D) model [Oosawa, 1970], a key assumption is that the departure rate of tubulin subunits from the microtubule tip ($k_{off,MT}$) is a [Tub]-independent constant. As shown in Fig. 6.1A (left), this model specifies that, for a time interval Δt, the number of subunit associations, λ_+, is determined by the on rate constant

$k_{\mathrm{on,MT}}$ and the free tubulin concentration [Tub]. The number of departure events from the tip (λ_-) in this time interval depends only on the off rate constant, $k_{\mathrm{off,MT}}$. Thus, for the 1D model, the departure rate of tubulin subunits from the tip will remain constant, regardless of subunit arrival rate or [Tub].

Given the number of arrivals, λ_+, and the number of departures, λ_-, (both Poisson distributed) the resulting difference, $(\lambda_+ - \lambda_-)$, gives the distribution of incremental microtubule length changes (Fig. 6.1A, right). A strong but untested prediction of the 1D model is that the likelihood of large microtubule shortening events will decrease as the subunit arrival rate (λ_+) becomes larger (Fig. 6.1A, right). In the example shown in Fig. 6.1A (right), the probability of a shortening event whose magnitude is larger than some arbitrary value (e.g., larger than the vertical dashed line located at $|\lambda_+ - \lambda_-| = |-4|$ in Fig. 6.1A, right) decreases with increasing [Tub]. This is because microtubule growth increments will be strongly favored over shortening increments as the subunit arrival rate increases with increasing [Tub], while the departure rate remains constant. Thus, the 1D model can be tested by quantifying the distribution of microtubule length increments as a function of [Tub]. In particular, the 1D model predicts that the frequency of large shortening events should decrease at higher [Tub].

6.2.2 The Frequency of Large Microtubule Shortening Events Increases at Higher Tubulin Concentration in TIRF Experiments

To test the 1D model predictions, we performed *in vitro* GMPCPP-tubulin experiments to measure microtubule assembly dynamics at nanometer scale resolution. Using GMPCPP allowed us to focus on the intrinsic variability in the microtubule growth rate without the potentially confounding effects of nucleotide hydrolysis. As shown in Fig. 6.1B, assembly of GMPCPP-tubulin labeled with Alexa-488 (55 % labeled, Invitrogen Corp.) onto Rhodamine-labeled GMPCPP-tubulin seeds was imaged by TIRF microscopy (section 6.4 on p. 6.4 and [Gell et al., 2010]). We measured

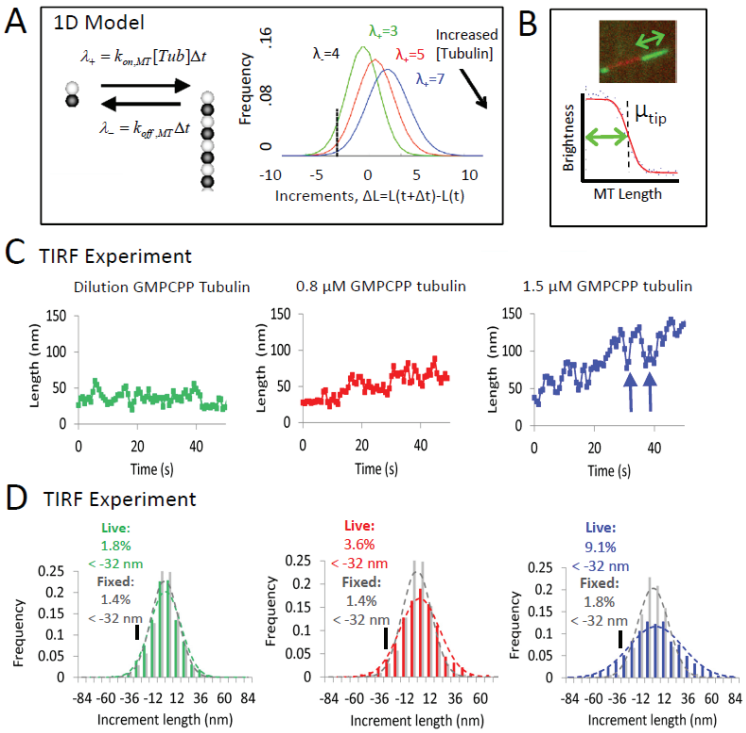

Figure 6.1: TIRF microscopy reveals $k_{\text{off,MT}}$increases with [Tub]. (A) A 1D model (left). In a time interval Δt, the number of subunits added to the tip is $\lambda_+ \propto$ [Tub], while the number of subunits lost, λ_-, is [Tub]-independent. The 1D model predicts (right) that large shortening events (e.g., left of vertical dashed line) decrease in frequency as [Tub] increases (i.e., as λ_+ increases). (B) Microtubule length measured at high spatial resolution using TIRF microscopy. Microtubule extensions (green), grown from GMPCPP microtubule seeds (red), are visualized during growth at varying [Tub]. Tip position is measured by fitting the decay in fluorescence intensity to the error function [Demtchouk et al., 2011]. (C) Typical growth traces at different [Tub]. v_g variability increases with [Tub]. Furthermore, the magnitude of large shortening events increases at higher [Tub] (e.g., blue arrows). (D) Quantification of v_g variability. Length increments over 1.4 s intervals are summarized for each concentration. The fixed-microtubule increment distribution is narrower than the live increment distribution for both 0.8 and 1.5 µM ($p = 0.018$ and $p = 0.002$ by t-test, respectively). In contradiction to 1D model predictions (see A), large negative (shortening) increments are more common at higher [Tub]. For example, shortening events < -32 nm account for 1.8 % of all length increments in the dilution experiments, but 9.1 % of such increments at a [Tub] = 1.5 µM. As a control, we show the distribution of increments obtained from fixed microtubules (gray dashed line). The fraction of length change increments for fixed microtubules remains relatively unchanged (1.4 % for a pre-fix [Tub] of 0.6 µM, and 1.8 % for 1.5 µM).

the length of microtubule extensions at 700 ms intervals in the presence of two different non-zero concentrations of GMPCPP tubulin, and in a dilution experiment in which the residual [Tub] was estimated to be ∼0.1 µM. Although the time-lapse interval between subsequent images was 700 ms, all of the images were collected using 100 ms exposure times, regardless of concentration.

The positions of microtubule ends were estimated by fitting the error function to the fluorescence intensity at microtubule end, where the microtubule end was defined as the position at which the error function fell to 50 % of the signal (μ_{tip}, Fig. 6.1B) [Bicek et al., 2009; Demtchouk et al., 2011; Pearson et al., 2006; Wan et al., 2009]. Because GMPCPP tubulin spontaneously nucleates at ∼2 µM tubulin, we selected [Tub] for analysis from ∼ 0.1 µM (dilution experiments) to 1.5 µM GMPCPP tubulin, which represents a ∼15-fold range of concentration.

As expected, the rate of net assembly increased as the [Tub] increased from dilution experiments to 1.5 µM (Fig. 6.1C). Due to the low [Tub], the net microtubule growth velocity is slow even at the highest concentration tested (maximum value of ∼0.15 µm min^{-1} at 1.5 µM GMPCPP tubulin), which is consistent with the previously reported value of 0.07 µm min^{-1} at 0.5 µM GMPCPP tubulin [Brouhard et al., 2008].

We found that microtubule growth trajectories in dilution experiments and at 0.8 µM GMPCPP-tubulin (Fig. 6.1C, green and red) showed steady growth or shortening with small length fluctuations, while microtubule growth trajectories at 1.5 µM GMPCPP-tubulin (Fig. 6.1C, blue) appeared to grow "noisily" with larger length fluctuations. These fluctuations were quantified by calculating the net length change increments for each 1.4 s interval during the first 30 s of growth for each microtubule (Fig. 6.1D).

We note that the measurement error can be readily estimated from the increment distribution for fixed microtubules (gray), where the standard deviation of increments is ∼20 nm (corresponding to single time point position estimates of $\pm 20\,\text{nm}/\sqrt{2} =$

$\pm 14\,\mathrm{nm}$), and so the measurement accuracy is on the nanoscale. To account for potential microtubule tip tracking accuracy changes as a function of microtubule tip structure, we fixed microtubules after having grown them in the correct corresponding [Tub] in each case.

Using the TIRF system, we found that the experimentally observed frequency of large shortening events (e.g., $< -32\,\mathrm{nm}$, equivalent to 4 dimer lengths and significantly above measurement error) increases at higher [Tub] ($(1.8 \pm 0.4)\,\%$ in dilution experiments to $(9.1 \pm 0.8)\,\%$ at $1.5\,\mu\mathrm{M}$ tubulin, Fig. 6.1D). This result stands in direct conflict with the 1D model, which predicts that the frequency of large microtubule shortening events should decrease with increasing [Tub] (Fig. 6.1A, left). We note that for fixed (non-dynamic) microtubules the frequency of "shortening" events arising from measurement noise alone is approximately independent of [Tub], ranging from $(1.4 \pm 0.4)\,\%$ at low concentration to $(1.8 \pm 0.4)\,\%$ at high concentration. Thus, the increase in the frequency and magnitude of shortening events at higher [Tub] strongly suggests that the tubulin subunit dissociation rate from the microtubule tip increases at higher [Tub], which violates a basic assumption of the 1D model.

6.2.3 The Frequency of Large Shortening Events Increases at Higher Tubulin Concentration in Laser Tweezers Experiments

To examine microtubule growth rates with higher resolution, we measured the variability in growth rates using our high temporal and spatial resolution nanoscale laser tweezers assay (Chapter V, [Schek et al., 2007]). Here, a spatial resolution of $< 3.5\,\mathrm{nm}$ at 10 Hz temporal resolution is achieved by measuring the position of microtubule-attached beads as microtubules grow into a microfabricated barrier (Fig. 6.2A). We observed variability in microtubule growth at three different [Tub], with variability increasing substantially at higher [Tub] (Fig. 6.2B). By quantitatively comparing the growth increment sizes at $0.1\,\mathrm{s}$ time intervals, we found that the frequency of

large shortening events (e.g., $< -8\,\mathrm{nm}$) increased from $(1.4 \pm 0.3)\,\%$ of all events at $0.5\,\mu\mathrm{M}$ tubulin, to $(6.3 \pm 0.5)\,\%$ of all events at $1.5\,\mu\mathrm{M}$ tubulin (Fig. 6.2C). As described above, this stands in marked contrast to the expectation from the 1D model, which predicts that the frequency of large shortening events should decrease at higher [Tub]. Because of the higher spatial-temporal resolution in the tweezers experiment, we were also able to test for the possible addition of oligomers [Kerssemakers et al., 2006; Schek et al., 2007]. Here, we never observed increments equal to or larger than 16 nm (i.e., two subunits) at $0.5\,\mu\mathrm{M}$ and $1.0\,\mu\mathrm{M}$ ($N = 4998$ increments), and only very rarely at $1.5\,\mu\mathrm{M}$ ($0.93\,\%$, $N = 2567$ increments). In addition, these rare instances of increments larger than 16 nm could be explained by rapid successive addition events of single subunits [Schek et al., 2007], particularly considering our estimates (below) of subunit exchange rates. Thus, similar to the TIRF data, the optical tweezers data indicates that the tubulin subunit dissociation rate from the microtubule tip increases at higher [Tub], which is inconsistent with the 1D model.

In addition, the laser-tweezers data was collected using unlabeled tubulin, which provides an important control for the labeled tubulin in the TIRF experiments, as similar results are obtained in both experiments. Because results are consistent between the laser-tweezers data, which used unlabeled tubulin, and the TIRF experiments, this argues that differently labeled tubulins are not a significant source of growth variance.

6.2.4 Concentration-Dependent Tubulin Subunit Dissociation Rates are Explained by Accounting for Both Lateral and Longitudinal Bonds

Because the tubulin dissociation rate from the microtubule tip increases at higher [Tub], it seems necessary that the state of the microtubule tip is on average shifted to a less stable configuration at higher [Tub]. To explicitly account for the energetic states of individual tubulin subunits in the microtubule, we performed computational

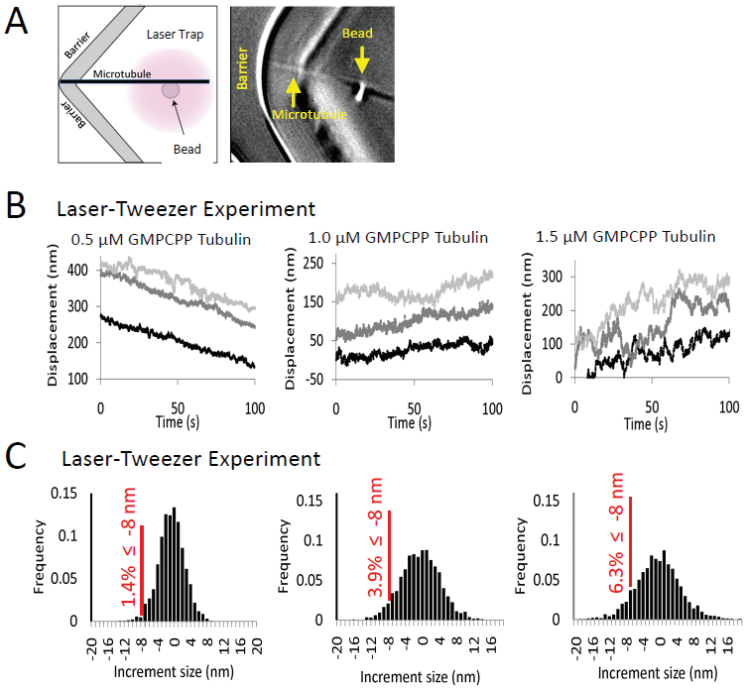

Figure 6.2: Nanoscale optical tweezers experiments confirm increasing growth rate variability and frequency of large shortening events at higher [Tub] (A) In high temporal and spatial resolution laser tweezer experiments, the position of a microtubule-attached bead is monitored as the microtubule tip grows against a microfabricated barrier. (B) Net assembly rate variability is measured with increasing [Tub]. In experimental traces shown at right, the microtubule growth rate variability becomes larger (i.e., "noisier") with increasing [Tub]. (C) Histograms of microtubule length change increments at 0.1 s intervals show increased variability with increasing [Tub]. Importantly, large microtubule shortening events increase in frequency at higher [Tub] (percentages of increments that are $\leqslant -8$ nm shown in red), consistent with the TIRF measurements, but in direct contradiction to both intuitive expectation and the 1D model prediction.

simulations using our previously published "2D" model for microtubule assembly [VanBuren et al., 2002]. In contrast to the 1D model, where protofilaments are regarded as independent with a single $k_{\mathrm{off,PF}}$, the 2D model explicitly accounts for the bonds in both the lateral and longitudinal directions. Together, these bonds stabilize a subunit. As the number of these bonds varies, the $k_{\mathrm{off,PF}}$ will also change. Since the number of lateral bonds between subunits at the tip depends on the tip structure, $k_{\mathrm{off,PF}}$ averaged over time and all protofilaments yields $k_{\mathrm{off,MT}}$. This value for $k_{\mathrm{off,MT}}$ could increase at higher [Tub], consistent with our experimental observations (Figs. 1 and 2). Therefore, we asked whether the 2D model predicts an increase in $k_{\mathrm{off,MT}}$ at higher [Tub].

The 2D simulation accounts for (1) subunit arrivals at the tip of the microtubule, and (2) subunit departures from the tip (Fig. 6.3A). For arrivals, the subunit arrival rate at the tip of a protofilament ($k^*_{\mathrm{on,PF}}$) is given by

$$k^*_{\mathrm{on,PF}} = k_{\mathrm{on,PF}}[\mathrm{Tub}] \tag{6.1}$$

where $k_{\mathrm{on,PF}}$ is the on rate constant per individual protofilament ($\mu\mathrm{M}^{-1}\,\mathrm{s}^{-1}$, such that $k_{\mathrm{on,MT}} = 13k_{\mathrm{on,PF}}$), $k^*_{\mathrm{on,PF}}$ is the arrival rate per individual protofilament (s^{-1}, similarly $k^*_{\mathrm{on,MT}} = 13k^*_{\mathrm{on,PF}}$), and [Tub] is the free tubulin subunit concentration. This expression for tubulin subunit arrival rate to each protofilament is identical to the 1D model. However, to account for energetic differences between tubulin subunits at the microtubule tip, in the 2D model the subunit departure rate from a given protofilament, $k_{\mathrm{off,PF}}$, depends on the equilibrium constant, where

$$K_{\mathrm{eq}} \equiv \frac{k_{\mathrm{on,PF}}}{k_{\mathrm{off,PF}}} = e^{-\Delta G^0_{\mathrm{total}}/k_{\mathrm{B}}T}. \tag{6.2}$$

Therefore, by rearrangement:

$$k_{\text{off,PF}} = \frac{k_{\text{on,PF}}}{e^{-\Delta G^0_{\text{total}}/k_{\text{B}}T}} \tag{6.3}$$

where, $k_{\text{off,PF}}$ is the off rate per individual protofilament (s^{-1}), k_{B} is Boltzmann's constant, T is absolute temperature, and $\Delta G^0_{\text{total}}$ is the total free energy of the stabilizing bonds on a specific subunit, given by

$$\Delta G^0_{\text{total}} = \sum \Delta G^{0*}_{\text{Longitudinal}} + \sum \Delta G^0_{\text{Lateral}} \tag{6.4}$$

In this way, tip subunits will (by definition) have one longitudinal bond (Fig. 6.3A), and therefore the total value for $\Delta G^{0*}_{\text{Longitudinal}}$ will be identical for all subunits at the tip. However, the lateral bond energy ($\Delta G^0_{\text{Lateral}}$) will vary, such that subunits with two lateral neighbors will have a two-fold more negative value for $\Delta G^0_{\text{Lateral}}$ than subunits with only one lateral neighbor.

As the stochastic 2D model computer simulation proceeds (see movies accompanying Gardner et al. [2011]), the tip structure naturally evolves as subunits arrive and depart from the tip of each protofilament, and the behavior averaged over time can be calculated for a given [Tub] (simulation parameters in Table 6.2 and Fig. 6.4). The steady-state subunit off rate from the microtubule tip (averaged over time and summed over all protofilaments) can then be calculated as a function of the free subunit concentration. Consistent with our experimental data, we found that interactions between neighboring protofilaments can result in a strong concentration-dependent subunit dissociation rate from the microtubule tip (Fig. 6.3B). As a result, the 2D model predicts that net microtubule assembly (Fig. 6.3B, blue) results from the relatively small difference between a large subunit arrival rate that increases with [Tub] (Fig. 6.3B, green), and a large subunit departure rate that also increases with increasing [Tub] (Fig. 6.3B, red). Thus, the 2D model assumes that subunits at the tip of a growing microtubule are not energetically identical, and therefore predicts that

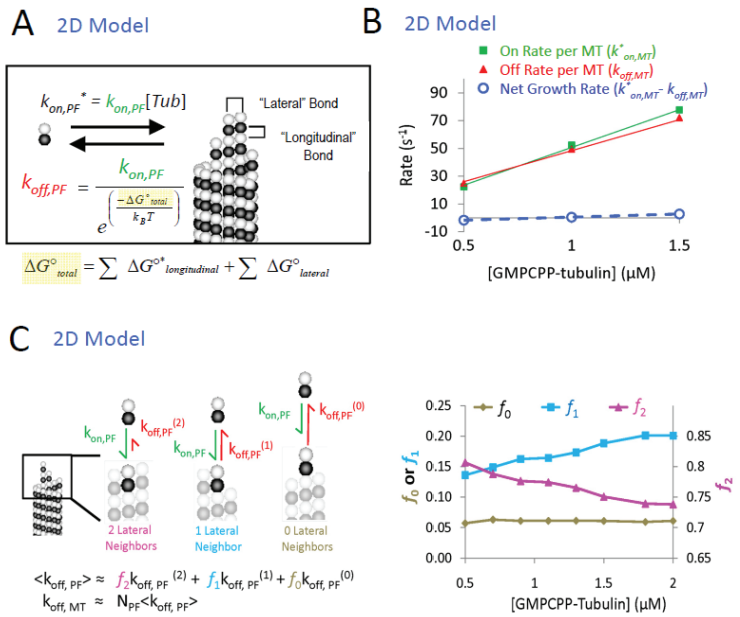

Figure 6.3: A 2D model predicts that tubulin subunit dissociation rates are dependent on [Tub] (A) Microtubules grow and shorten via the addition and loss of $\alpha\beta$-tubulin subunits. A 2D model includes the effect of both lateral bond interactions between neighboring protofilaments and longitudinal bonds along the protofilament. In the 2D model, subunit on rates and off rates can be calculated, such that the on rate depends on the [Tub], while tubulin subunit off rates depend on their stability in the polymer, as calculated by summing all of the lateral and longitudinal bond energies for a given tubulin subunit. (B) The 2D model predicts that tubulin dissociation rates increase at higher [Tub] (red). Thus, the net assembly rate (blue) is given by the small difference between the large on rate (green) and the large off rate (red). (C) Left: Lattice thermodynamics dictate that dissociation rates at growing microtubule tips vary for each protofilament based on the number of lateral neighbor interactions at the protofilament tip. Here, dissociation rates are high for tubulin subunits with fewer lateral neighbors, while increasing the number of lateral neighbors (and thus increasing the number of stabilizing lateral bonds) results in reduced dissociation rates. Right: The 2D model predicts that 1-neighbor protofilament tip interactions increase in likelihood at higher [Tub], while 2-neighbor interactions decrease with increasing free subunit concentration.

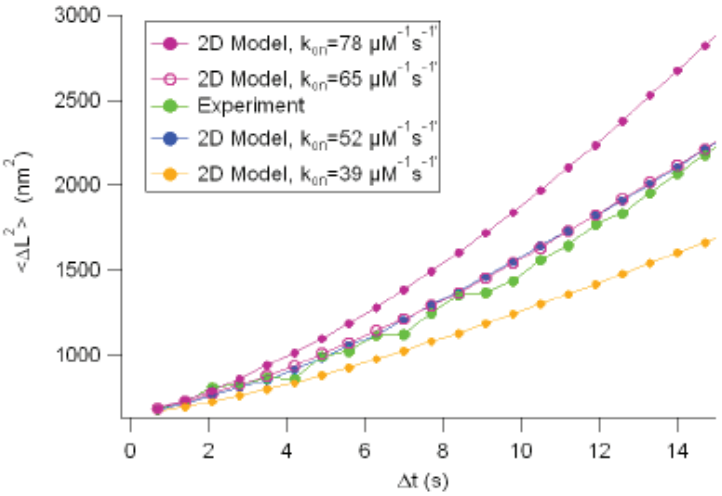

Figure 6.4: Constraint of $k_{\text{on,MT}}$ in 2D Model Simulations. By quantifying the microtubule length change increment variance as a function of time step, $k_{\text{on,MT}}$ is constrained in the 2D model simulation. The range of tested values for $k_{\text{on,MT}}$ is 39-78 $\mu\text{M}^{-1}\,\text{s}^{-1}$, and values of 52 and 65 $\mu\text{M}^{-1}\,\text{s}^{-1}$ are consistent with experimental results.

the average $k_{\text{off,MT}}$ increases at higher [Tub]. This result provides an explanation for the discrepancy between the 1D model and our experimental observations.

Why do the subunit dissociation rates increase at higher [Tub]? The protofilament dissociation rate constant is dependent on the number of neighboring protofilaments available for forming stabilizing lateral bonds (Fig. 6.3C), which must on average be shifted toward less stable configurations as the [Tub] increases. For example, tubulin subunits with two lateral neighbors (Fig. 6.3C, left) have a low dissociation rate constant, while subunits with one lateral neighbor have a moderate dissociation rate constant, and tubulin subunits with no lateral neighbors have a high dissociation rate constant due to the lack of any stabilizing lateral bonds (Fig. 6.3C, left). Thus, if the probability of the configurations were known, the dissociation rate constant averaged over the entire microtubule tip ($k_{\text{off,MT}}$) would be given by

$$k_{\text{off,MT}} \approx f_0 k_{\text{off,PF}}^{(0)} + f_1 k_{\text{off,PF}}^{(1)} + f_2 k_{\text{off,PF}}^{(2)} \tag{6.5}$$

Table 6.2: 2D Model Simulation Parameter Values

Parameter	Description	Value	Reference
[Tub]	Free subunit concentration	0.5 to 1.5 µM	Experiment
$k_{\mathrm{on,MT}}$	On-rate constant	52 to 65 $\mu\mathrm{M}^{-1}\,\mathrm{s}^{-1}$	Constrained by experimental GMPCPP increment variance
$k_{\mathrm{hydrolysis}}$	Hydrolysis rate	$0\,\mathrm{s}^{-1}$	Assumed negligible
$\Delta G^{0*}_{\mathrm{Longitudinal}}$	Free energy of longitudinal interaction incorporating entropic penalty of immobilization	$-9.5 k_{\mathrm{B}}T$	Constrained for GMPCPP by model-fitting to all new experimental results
$\Delta G^{0}_{\mathrm{Lateral}}$	Free energy of lateral interaction	-4.5 to $-5.0 k_{\mathrm{B}}T$	Constrained by GMPCPP experimental results with value depending on $k_{\mathrm{on,MT}}$
k_{b}	Spring constant for bead-microtubule linkage	$0.021\,\mathrm{pN\,nm}^{-1}$	Schek et al. [2007]
k_{trap}	Spring constant for trap	$0.021\,\mathrm{pN\,nm}^{-1}$	Schek et al. [2007]
T	Temperature	309 K	Experiment
δ	On-rate penalty for lagging protofilaments	15	Constrained by model-fitting to experimental tip standard deviation measurements

where f_i are the mean probabilities of tubulin subunits at the tip with i lateral neighbors, and $k^{(i)}_{\mathrm{off,PF}}$ are the individual protofilament dissociation rate constants for a tubulin subunit with i lateral neighbors [Hill, 1986].

We then examined in what way the relative fractions of tubulin subunits with 0, 1, or 2 lateral neighbors change with increasing [Tub] in the 2D model. We found that the fraction of tubulin subunits at microtubule tips with 0 lateral neighbors remains relatively constant at all concentrations (Fig. 6.3C, right, yellow). However, there is an increase in the probability of relatively unstable 1 lateral neighbor subunits at the microtubule tip with increasing [Tub] (Fig. 6.3C, right, blue), and a corresponding decrease in the probability of relatively stable tubulin subunits having 2 lateral neighbors (Fig. 6.3C, right, magenta). This result explains why the subunit dissociation rate accelerates with increasing [Tub] in the 2D model. It is important to appreciate that the off rate is enslaved to, or dependent upon, the on rate. This means that as the on rate goes up, the tip becomes more extended (i.e., protofilament lengths are more variable with increasing tendency toward only one lateral neighbor), which in turn increases the off rate. Thus, the off rate is in fact dependent on the on rate, and they rise together.

6.2.5 The 1D and 2D Models Both Predict the Linear Dependence of Growth Rate on Tubulin Concentration But With Differing Rate Constants

To quantitatively test both the 1D and the 2D models, we first constrained their association rate constants based on mean microtubule growth rate as a function of [Tub]. For the 1D model, the average association rate constant for an entire microtubule tip, $k_{\mathrm{on,MT}}$ ($\mu\mathrm{M}^{-1}\,\mathrm{s}^{-1}$) and the average tip dissociation rate constant, $k_{\mathrm{off,MT}}$ (s^{-1}) have been previously estimated from experimental measurements of the net assembly rate, v_{g} (subunits/s; with $\sim 1625\,$subunits/μm of microtubule length) as a

function of the free subunit concentration, [Tub] (μM), using:

$$v_g = k_{on,MT}[\text{Tub}] - k_{off,MT} \tag{6.6}$$

Using equation 6.6, the 1D model average association rate constant ($k_{on,MT}$) is the slope of a linear fit to the net assembly rate *vs.* [Tub], while the 1D model average dissociation rate constant ($k_{off,MT}$) is the y-intercept (Fig. 6.5A). Numerous *in vitro* studies have confirmed the predicted linear relationship for growing GTP-tubulin microtubules, and for GMPCPP-tubulin microtubules, which do not undergo transitions to rapid shortening due to very slow hydrolysis of this GTP analogue [Dye and Williams, 1996]. These studies, summarized in Table 6.1, have consistently yielded average association rate constants of $k_{on,MT} \approx 5\,\mu M^{-1}\,s^{-1}$ (range 1–9 $\mu M^{-1}\,s^{-1}$) and average dissociation rates of $k_{off,MT} \approx 15\,s^{-1}$ (range 0.1–44 s^{-1}).

Similar to these studies, we experimentally measured the microtubule growth velocity as a function of [Tub] using both the *in vitro* TIRF and the nanoscale laser tweezers assays (Fig. 6.5A).

We then calculated the 1D model association and dissociation rate constants using the combined results from both experiments (Fig. 6.5A). From the slope and intercept, the 1D model microtubule association rate constant for GMPCPP-Tubulin was $k_{on,MT} = 5.1\,\mu M^{-1}\,s^{-1}$, and the dissociation rate constant was $k_{off,MT} = 3.9\,s^{-1}$. Thus, our observed growth velocity dependence on [Tub] was within the range previously observed and yields similar 1D model rate constants to those previously reported (Table 1).

The 2D model also predicts a linear dependence of microtubule growth rate on tubulin concentration (Fig. 6.5B). However, the 2D model predicts that the average dissociation rate increases approximately linearly with [Tub] due to evolving tip structures (Fig. 6.3B). This in turn requires that the association rate constant is substantially larger than in a 1D model in order to produce the observed net micro-

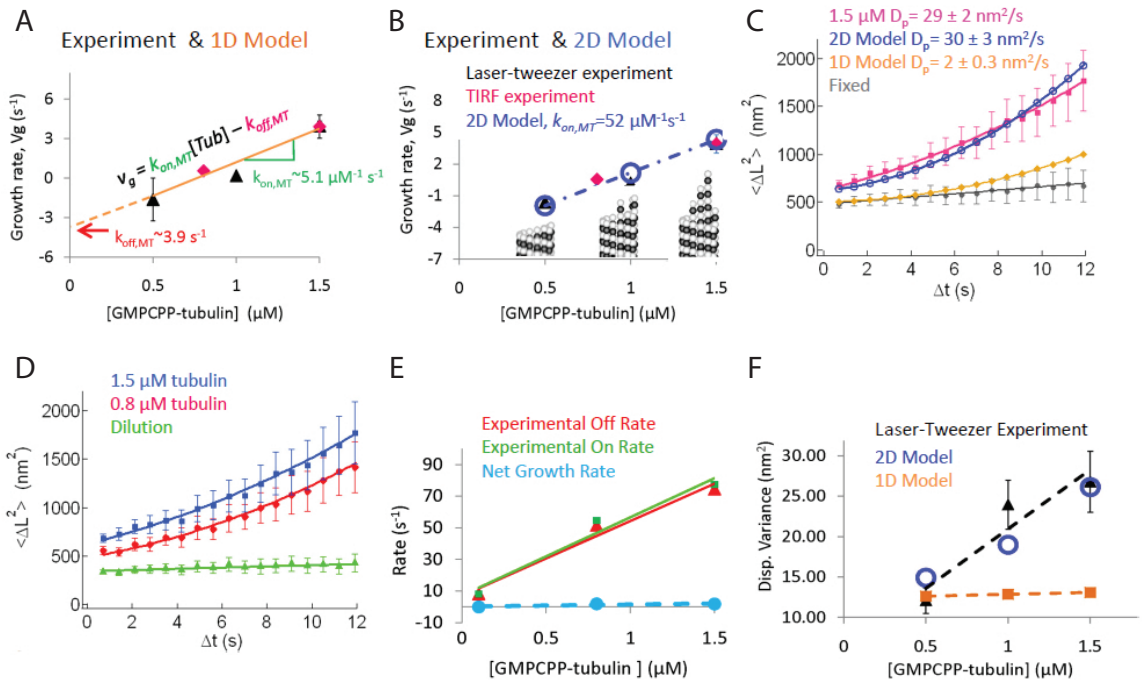

Figure 6.5: Lateral interactions require rapid on-off kinetics for subunits at the microtubule tip. (A) 1D-model estimates of $k_{\mathrm{off,MT}}$ and $k_{\mathrm{on,MT}}$ based on laser-tweezers and TIRF-microscopy data. (B) Similar to the 1D model, a 2D model predicts v_{g} increases linearly with [Tub]. However, to produce the correct v_{g} it requires $k_{\mathrm{on,MT}}$ an order of magnitude higher because of increasing $k_{\mathrm{off,MT}}$ at higher [Tub] as tip structures become more extended. (C) A 2D model with rapid subunit exchange predicts experimental microtubule growth variability in the TIRF assay, as quantified by D_{p} (discussion of equation 6.7), while a first-order Poisson process (derived from the 1D model) with slow exchange fails to reproduce the experimentally observed variability in v_{g}. Here, D_{p} is estimated by fitting equation 6.7 to mean squared microtubule length increment ($\langle \Delta L^2 \rangle$) *vs.* time interval ($\Delta t$). The experimental estimate and 2D model value of D_{p} are both at least an order of magnitude larger than predicted for a 1D model. (D) Similar analysis to (C) at varying [Tub]yields $k^*_{\mathrm{on,MT}} \equiv k_{\mathrm{on,MT}}$[Tub], $k_{\mathrm{off,MT}}$, and v_{g} estimates (main text, Table 6.3, and (E)). (E) Experimental $k^*_{\mathrm{on,MT}}$ and $k_{\mathrm{off,MT}}$ as a function of [Tub]. Similar to the 2D model prediction (Fig. 6.3B), $k_{\mathrm{off,MT}}$ increases with [Tub] (red). v_{g} (blue) is given by the small difference between the large on (green) and large off (red) rates. (F) A 2D model with fast subunit exchange predicts experimental microtubule growth variability in the laser-tweezer assay, while a first-order Poisson process (derived from the 1D model of Oosawa) with slow exchange fails to reproduce the experimentally observed growth rate variance at higher [Tub]. The 1D model predicts the variance is smaller than the measurement variance, and so should appear constant across all [Tub].

Table 6.3: Experimental On and Off Rate Constant Estimates for Microtubule Plus-ends

Nucleotide	GMPCPP			GTP		
[Tub] (µM)	Dilution	0.8	1.5	7.0	9.0	12.0
D_{p} ($\mathrm{nm^2\,s^{-1}}$)	3.1±0.24	20.1±2.0	28.8±2.4	111±12	155±11	272±16
$\hat{v}_{\mathrm{g}}$ ($\mathrm{nm\,s^{-1}}$)	-0.06±0.12	1.9±0.07	1.8±0.11	5.7±0.18	7.9±0.13	10.7±0.36
$k_{\mathrm{off,MT}}$ ($\mathrm{s^{-1}}$)	8.2±0.65	51.6±5.3	74.5±6.3	287±30	402±29	708±42
$k_{\mathrm{on,MT}}$[Tub] ($\mathrm{s^{-1}}$)	8.1±0.67	54.6±5.3	77.4±6.4	296±30	414±29	726±43
$k_{\mathrm{on,MT}}$ ($\mu\mathrm{M^{-1}\,s^{-1}}$)	81.3±0.44	68.3±6.6	51.6±4.3	42.3±4.3	46.0±3.2	60.5±3.5

s.e. in D_{p} and v_{g} obtained by Poisson stepper model. s.e. in rate constants obtained by propagation of errors. For the dilution experiment, the residual GMPCPP-Tubulin concentration was estimated to be 0.1 µM by using the ratio of TIRF background fluorescence before and after dilution of 1.5 µM tubulin, using the formula: (background mode in 1.5 µM - camera offset)/(background mode after dilution – camera offset)=(1.5/residual dilution concentration). There was no significant background photobleaching in the dilution movies, suggesting that the coverslip-attached tubulin is negligible in this case.

tubule growth rate (Figs. 3B and 4B). As a result, the 2D model association rate constant must be approximately an order of magnitude higher than the association rate constant estimated for the 1D model ($k_{\mathrm{on,MT}} \approx 52\,\mu\mathrm{M}^{-1}\,\mathrm{s}^{-1}$ with a 2D model, see Fig. 6.4 and Table 6.2) (Fig. 6.5B). This 2D model association rate constant, when considered on a per protofilament basis ($k_{\mathrm{on,PF}} = k_{\mathrm{on,MT}}/13 = 4\,\mu\mathrm{M}^{-1}\,\mathrm{s}^{-1}$), is consistent with theoretical predictions for rotational-translational diffusion-limited protein-protein association reactions [Northrup and Erickson, 1992] and is similar to that estimated for F-actin (2 protofilament) self-assembly on a per protofilament basis, $k_{\mathrm{on,filament}} = 11.6\,\mu\mathrm{M}^{-1}\,\mathrm{s}^{-1}$ or $k_{\mathrm{on,PF}} = 5.8\,\mu\mathrm{M}^{-1}\,\mathrm{s}^{-1}$ [Pollard, 1986].

6.2.6 The Variability in Growth Rate is Significantly Underpredicted by the 1D Model, But is Correctly Predicted By the Rapid On-Off Kinetics Required in the 2D Model

For a stochastic process the variance in the number of events per time interval is equal to the mean number of events. Therefore the variability in the rate of microtubule growth should reflect the underlying rates of subunit addition and loss. As described above, since the 2D model predicts rate constants that are an order of magnitude higher than the 1D model, it also predicts a much larger variance in microtubule assembly rate. To quantitatively compare the predictions of the 1D and 2D models to our experimental results, we calculated the mean squared displacement of microtubule length increments for increasing time steps, and plotted the results for each model with the 1.5 µM TIRF experimental data (Fig. 6.5C). By plotting the results in this manner, the length fluctuations of filament growth can be described by a diffusion with drift equation, as given by:

$$\left\langle \Delta L^2 \right\rangle = v_{\mathrm{g}}^2 \Delta t^2 + 2D_{\mathrm{p}} \Delta t + \sigma^2 \tag{6.7}$$

where ΔL is the microtubule length change increment (in nm) over a given time step Δt (in s), v_{g} is the net growth rate ($\mathrm{nm\,s^{-1}}$), and D_{p} is the effective diffusion coefficient for the microtubule polymerization, which provides a quantitative measure of the variability in microtubule growth increments. Finally, σ^2 is the experimental measurement noise.

By fitting the experimental data and both models' predicted data to a quadratic equation, the diffusion coefficient (D_{p}) can be estimated, which provides a quantitative measure of the microtubule growth variability. The 1D model diffusion coefficient D_{p} (constrained by mean growth rate data to $k_{\mathrm{on,MT}} = 5.1\,\mu\mathrm{M}^{-1}\,\mathrm{s}^{-1}$ and $k_{\mathrm{off,MT}} = 3.9\,\mathrm{s}^{-1}$, as in Fig. 6.6A) is an order of magnitude lower than the experimental diffusion coefficient (Fig. 6.5C). In contrast, the 2D model, constrained by the mean growth rate experiments to a 10-fold higher association rate constant than in the 1D model ($k_{\mathrm{on,MT}} = 52\,\mu\mathrm{M}^{-1}\,\mathrm{s}^{-1}$), predicts a diffusion coefficient D_{p}, that is similar to the experimental data (Fig. 6.5C, 2D model parameters as in Table 6.2). Thus, microtubule assembly is too variable to be consistent with the 1D model, but is consistent with the 2D model.

6.2.7 Experiments Confirm Rapid Tubulin On-Off Kinetics Predicted by the 2D Model

The tubulin subunit on rate ($k^*_{\mathrm{on,MT}} \equiv k_{\mathrm{on,MT}}[\mathrm{Tub}]$) and the off rate ($k_{\mathrm{off,MT}}$) from the microtubule tip can be directly estimated from the mean-squared displacement versus time data (Fig. 6.5D). The diffusion coefficient, D_{p}, relates the microtubule length mean squared displacement due to diffusion alone, $\langle \Delta l_{\mathrm{D}}^2 \rangle$, to the time interval, Δt, via

$$\left\langle \Delta l_{\mathrm{D}}^2 \right\rangle = 2 D_{\mathrm{p}} \Delta t \tag{6.8}$$

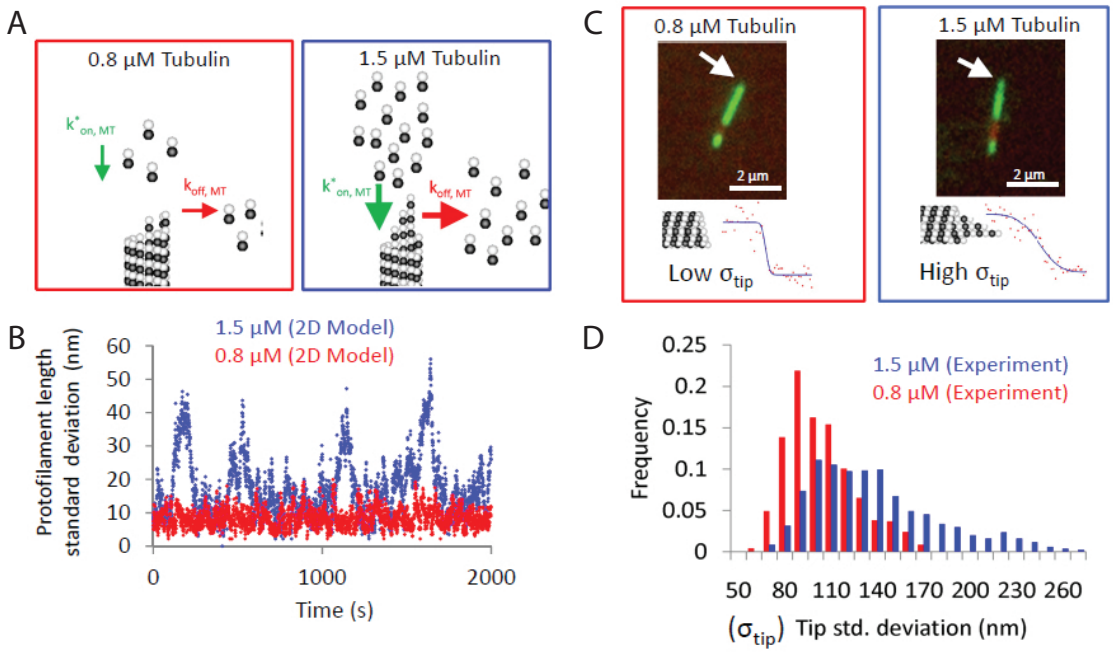

Figure 6.6: TIRF microscopy measurements show that microtubule tip structure depends on free GMPCPP-tubulin concentration. (A) A 2D model predicts that $k_{\text{off,MT}}$ increases at higher [Tub] because of increased incidence of 1-neighbor subunits at the tip (greater disparity in protofilament length), which are promoted at high $k^*_{\text{on,MT}} \equiv k_{\text{on,MT}}$[Tub]. (B) The standard deviation of protofilament lengths for a given microtubule provides a measure of the variability in protofilament lengths. The 2D model predicts that the standard deviation of protofilament lengths will, on average, be large in 1.5 µM tubulin relative to 0.8 µM tubulin. (C) Fitting the error function to the decay in fluorescence intensity at the microtubule end yields estimates of the mean (μ_{tip}) and the standard deviation (σ_{tip}) of the error function. μ_{tip} represents the microtubule tip position (as described above), while σ_{tip} reflects the variability in protofilament lengths at the microtubule tip. A low σ_{tip} (left) suggests that microtubule tips are blunt, with low variation in protofilament length. Conversely, a high σ_{tip} (right) suggests that tips are extended, with a higher variation in protofilament length. (D) In TIRF experiments, the tip standard deviation increases with increasing free GMPCPP-tubulin concentration. At [Tub] = 0.8 µM, the mean±sd of σ_{tip} is (99 ± 22) nm (n=700), while at [Tub] = 1.5 µM it is (140 ± 55) nm (n=1120; $p < 10^{-15}$) (similar length microtubules at both concentrations). This experimental result shows that tips of microtubules growing in the presence of GMPCPP at [Tub] = 0.8 µM are relatively blunt with low protofilament length variation, while at [Tub] = 1.5 µM they are more extended, with a larger variation in protofilament lengths.

and the growth rate variance due to diffusion is described by a Skellam distribution [Oosawa, 1970; Skellam, 1946], so that

$$\left\langle \Delta l_{\mathrm{D}}^2 \right\rangle = a^2 \left(k_{\mathrm{on,MT}}[\mathrm{Tub}] + k_{\mathrm{off,MT}} \right) \Delta t \tag{6.9}$$

where a is the change in microtubule length contributed by a single dimer, which is on average 0.615 nm. Combining equations 6.8 and 6.9 and solving for D_{p} we obtain,

$$D_{\mathrm{p}} = \frac{a^2}{2} \left(k_{\mathrm{on,MT}}[\mathrm{Tub}] + k_{\mathrm{off,MT}} \right) \tag{6.10}$$

In addition, by definition,

$$\hat{v}_{\mathrm{g}} = a \left(k_{\mathrm{on,MT}}[\mathrm{Tub}] - k_{\mathrm{off,MT}} \right) \tag{6.11}$$

Thus, through these two equations 6.10 and 6.11, the two unknowns, $k_{\mathrm{on,MT}}$ and $k_{\mathrm{off,MT}}$, can be calculated at a given [Tub] using the experimental estimates of D_{p} and v_{g}. (Stukalin and Kolomeisky [2004] recommended this type of analysis. It is thoroughly explained by [Mirny and Needleman, 2010], but a factor of $N_{\mathrm{PF}} \approx 13$ is not accounted for.)

To calculate the values for $k_{\mathrm{on,MT}}$ and $k_{\mathrm{off,MT}}$ from the experimental data, and to confirm concentration-dependent tubulin subunit dissociation rates, we completed the mean-squared displacement analysis as described above for a range of [Tub] in the TIRF analysis (Fig. 6.5D). Detailed results are summarized in Table 6.3 and shown in Fig. 6.5E. The experimentally estimated tubulin dissociation rate increases substantially as the [Tub] is increased, and the relatively slow net experimental microtubule assembly rate (blue) represents the difference between a large experimental on rate (green) and a large off rate (red), similar to the 2D model prediction (Fig. 6.3B). For example, at 1.5 µM, the net microtubule assembly rate (blue) represents the dif-

ference between a large on rate, $k_{\mathrm{on,MT}}[\mathrm{Tub}] \approx 77\,\mathrm{s}^{-1}$ (green), and a large off rate, $k_{\mathrm{off,MT}} \approx 75\,\mathrm{s}^{-1}$ (red). In addition, the dilution experimental results demonstrate that the off rate collapses to very near the 1D model estimate when microtubule tips are blunt (1D model $k_{\mathrm{off,MT}} \approx 4\,\mathrm{s}^{-1}$, estimated experimental $k_{\mathrm{off,MT}}$ in dilution experiment, $\approx 8\,\mathrm{s}^{-1}$).

6.2.8 Growth Variability in the Laser-Tweezer Assay is Consistent with Rapid Tubulin Subunit On-Off Kinetics

We then asked whether, consistent with the TIRF assays, the variance in the growth rate measured using the optical tweezers assay is quantitatively larger than expected for the 1D model. As shown in Fig. 6.5F, the 1D model, constrained by mean growth rate data to $k_{\mathrm{on,MT}} = 5.1\,\mu\mathrm{M}^{-1}\,\mathrm{s}^{-1}$ and $k_{\mathrm{off,MT}} = 3.9\,\mathrm{s}^{-1}$ (Fig. 6.5A), predicts a microtubule growth rate variance in the laser tweezer assay of $\sigma^2_{\mathrm{Assembly}} = 1.0\,\mathrm{nm}^2$ at $0.5\,\mu\mathrm{M}$ tubulin ($k^*_{\mathrm{on,MT}} = 2.5\,\mathrm{s}^{-1}$) and $\sigma^2_{\mathrm{Assembly}} = 1.7\,\mathrm{nm}^2$ at $1.5\,\mu\mathrm{M}$ tubulin ($k^*_{\mathrm{on,MT}} = 7.6\,\mathrm{s}^{-1}$). Our laser tweezers assay has a measurement variance due to Brownian motion of the microtubule-bead complex of $\sigma^2_{\mathrm{Thermal}} = (3.5\,\mathrm{nm})^2 = 12\,\mathrm{nm}^2$ (at 10 Hz) [Schek et al., 2007]. Thus, the 1D model predicts that the experimentally observed variance, $\sigma^2_{\mathrm{Observed}} = \sigma^2_{\mathrm{Assembly}} + \sigma^2_{\mathrm{Thermal}} = 13\,\mathrm{nm}^2$, will be dominated by the thermal measurement noise and so will not depend on free subunit concentration (Fig. 6.5F, orange line). Contrary to this expectation, the microtubule growth increment distribution from the laser-tweezer assay increases with the [Tub], and is inconsistent with the 1D model at $1.0\,\mu\mathrm{M}$ ($p < 10^{-8}$, Two-tailed F-test) and $1.5\,\mu\mathrm{M}$ ($p < 10^{-8}$, Two-tailed F-test).

The 2D model, constrained by the mean growth rate experiments to a 10-fold higher association rate constant than the 1D model, predicts a substantial increase in growth rate variance with increasing [Tub]. For the 2D model at 0.1 s time intervals, the growth rate variance is predicted to increase from $15\,\mathrm{nm}^2$ at $0.5\,\mu\mathrm{M}$ tubulin to

$25\,\mathrm{nm}^2$ at $1.5\,\mu\mathrm{M}$ tubulin (Fig. 6.5F, blue, 2D model parameters as in Table 6.2) which is consistent with experimental results ($1.0\,\mu\mathrm{M}$, $p = 0.47$; $1.5\,\mu\mathrm{M}$, $p = 0.31$; Two-tailed F-Test). Thus, the experimentally measured microtubule growth variance at higher [Tub] is inconsistent with the relatively slow kinetics predicted by the 1D model, but is well described using a 10-fold higher tubulin association rate constant.

6.2.9 Experimentally, Microtubule Tips Are More Tapered At Higher Tubulin Concentration, Consistent with Concentration-Dependent Subunit Dissociation Rates

In shifting from low [Tub] (i.e., favoring 2 lateral neighbors, Fig. 6.3C) to high concentration (i.e., favoring 1 lateral neighbor, Fig. 6.3C), the microtubule tip structure shifts from being relatively blunt, where protofilaments are typically the same length, to a more tapered tip in which protofilament lengths are more variable (Fig. 6.6A). The 2D model simulations predict that at high [Tub] (i.e., when subunits arrive rapidly to the tip), protofilaments will tend to grow independently of their neighbors, which results in tip subunits that are more likely to have only 1 lateral neighbor. Specifically, the tip structures at higher [Tub] will exhibit greater disparity in protofilament length (i.e., higher protofilament length standard deviation), with more single-neighbor protofilament extensions (Fig. 6.6B, blue). In contrast, at low [Tub], the relatively higher off rate will favor blunt ends (i.e., lower protofilament length standard deviation), where two lateral neighbors predominate (Fig. 6.6B, red). These predictions are consistent with cryoelectron microscopy images of microtubules formed from GTP-tubulin, where the mean microtubule tip taper lengths increase with increasing [Tub] in the presence of GTP [Chrétien et al., 1995].

To test this prediction for GMPCPP microtubules, we estimated tip structures using TIRF microscopy by fitting the error function to the green Alexa-488 fluorescence intensity at microtubule ends, which yields both the mean protofilament

length (μ_{tip}) (Fig. 6.1B) and the standard deviation of protofilament lengths (σ_{tip}) (Fig. 6.6C) [Demtchouk et al., 2011]. Specifically, we expect that tips with small standard deviations have relatively "blunt" tips (Fig. 6.6C, left), while tips with larger standard deviations have more tapered tips (Fig. 6.6C, right). Using this approach, we quantified the distribution of tip standard deviations (σ_{PF}) for similar lengths of Alexa-488 microtubules grown at 0.8 µM and 1.5 µM GMPCPP-Tubulin (Fig. 6.6D). We found that the distribution of microtubule tip standard deviations at a concentration of 0.8 µM GMPCPP-Tubulin is (99 ± 22) nm (mean±sd; n=700), while the mean microtubule tip standard deviation at 1.5 µM GMPCPP-Tubulin is (140 ± 55) nm (mean±sd; n=1120) (Fig. 6.6D). This difference in tip standard deviations ($p < 10^{-15}$) suggests that microtubule tips are relatively blunt (with low protofilament length variation) in 0.8 µM GMPCPP-Tubulin, while at 1.5 µM they are more extended, with a larger variation in protofilament lengths. These results are consistent with the prediction that a decrease in the mean number of subunit lateral neighbors at the microtubule tip causes the mean subunit dissociation rate to accelerate with increasing [Tub].

6.2.10 GTP-Tubulin Growth Variability is Consistent with Rapid Tubulin Subunit On-Off Kinetics

To test whether the conclusions from our GMPCPP tubulin experiments would be consistent with GTP-tubulin experiments at nearer to physiological concentrations, we performed TIRF experiments with GTP-tubulin at 7, 9, and 12 µM, and also assessed the variability of dynamic GTP-tubulin microtubules with the laser-tweezer assay (results of Schek et al. [2007]. As is the case with GMPCPP-tubulin, the 2D model predicts that both $k^{*}_{\mathrm{on,MT}}$ and $k_{\mathrm{off,MT}}$ will increase at higher [Tub] (Fig. 6.7A). According to the 2D simulations, the increment variance will then increase proportionate to the tubulin concentration. Therefore, in our previous study with ~ 5 µM

GTP-tubulin in an *in vitro* laser tweezers microtubule assembly assay [Schek et al., 2007] we should have observed a variance of ≈3-fold larger than in our present 1.5 µM GMPCPP-tubulin experiments ($\frac{5\,\mu M}{1.5\,\mu M} \approx 3$). As shown in Fig. 6.7B, the variance is ≈3-fold higher at ≈3-fold higher [Tub] (5 µM GTP-tubulin *vs.* 1.5 µM GMPCPP tubulin both sampled at 0.5 s intervals).

In TIRF experiments with GTP-tubulin at 7, 9, and 12 µM, we observed an increase in microtubule growth variability and in negative growth excursions in going from 7 µM tubulin to 12 µM tubulin (Fig. 6.7C), similar to the GMPCPP tubulin data. As described above, we then fit the mean-squared-displacement data to the diffusion-drift model for each concentration (Fig. 6.7D). Using this method, the tubulin subunit on rate ($k^*_{\mathrm{on,MT}}$) and the off rate ($k_{\mathrm{off,MT}}$) from the microtubule tip can be directly estimated from the data (Fig. 6.7E, Table 2). Consistent with the GMPCPP tubulin experiments, the experimentally estimated tubulin dissociation rate increases substantially as the GTP-tubulin concentration is increased, and the net experimental microtubule assembly rate (blue) represents the small difference between a large experimental on rate (green) and a large off rate (red), similar to the 2D model prediction (Compare Fig. 6.7A and Fig. 6.7E). In these experiments, the measured range of [Tub] is consistent with *in vivo* tubulin concentration estimates (supplemental data accompanying Gardner et al. [2011]).

6.2.11 *In Vivo* Microtubule Growth Variability is Consistent with Rapid Tubulin Subunit On-Off Kinetics

To assess how our *in vitro* data compare with microtubule growth *in vivo* we measured microtubule growth at 0.5 s intervals near to the periphery of live LLC-PK1α cells, as previously described [Bicek et al., 2009] (Fig. 6.8A). To assess the measurement error, we also measured the length of microtubules in fixed LLC-PK1α cells at 0.5 s intervals (tubulin concentration estimate 5–15 µM, supplemental data

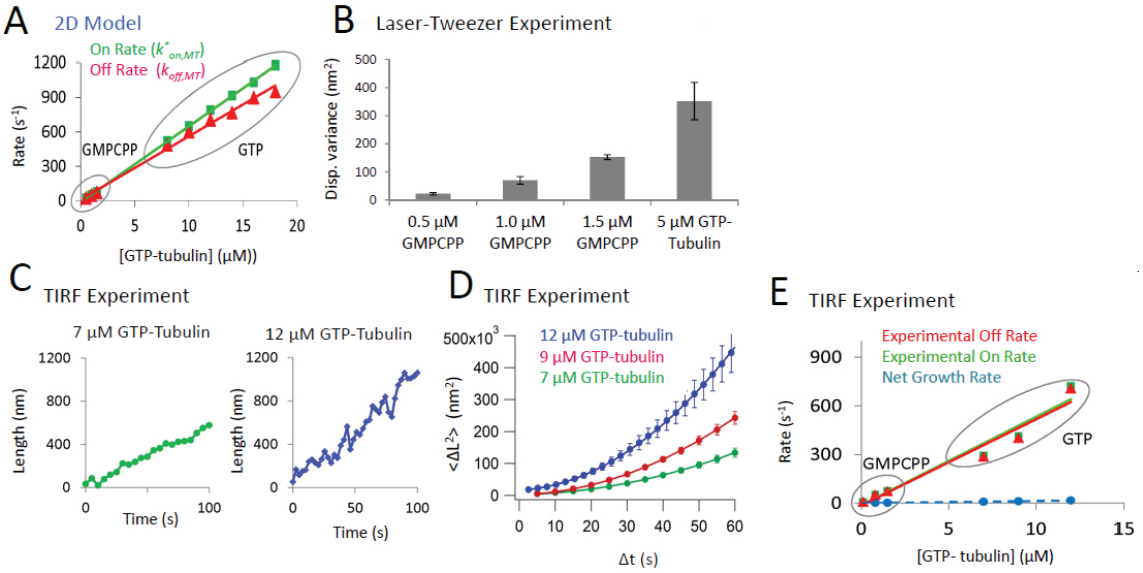

Figure 6.7: Higher [Tub] result in increased growth variability in vitro. (A) A 2D model predicts that subunit association rates and subunit dissociation rates will continue to increase for GTP-tubulin at higher [Tub]. (B) Because of rising association and dissociation rates at higher [Tub], the microtubule growth rate variability continues to increase for higher [Tub] (5 μM GTP-tubulin data from Schek et al. [2007], downsampled to 0.5 s intervals) (C) TIRF experiments with GTP-tubulin qualitatively show increasing growth variability at 12 μM tubulin as compared to 7 μM tubulin. (D) The polymerization diffusion coefficient (D_p) and the microtubule growth velocity (v_g) for three different concentrations of GTP-tubulin are estimated by fitting a quadratic curve to a plot of mean squared displacement (in microtubule length increments) vs. time step (Δt) as given by Eqn. 6.7. By analyzing the mean-squared displacement *vs.* time-step data at different [Tub], the subunit on rates, off rates, and net rates can be estimated in each case, as described in the text and summarized in Table 2 and (E). (E) Experimental subunit on rates and off rates are plotted as a function of GMPCPP-tubulin and GTP-tubulin concentration. Similar to the 2D model prediction (Fig. 6.7A), the subunit off rate rises with increasing [Tub] (red). The net assembly rate (blue) is given by the small difference between the large on rate (green) and the large off rate (red). Please see Fig. 6.8 for confirmation *in vivo*.

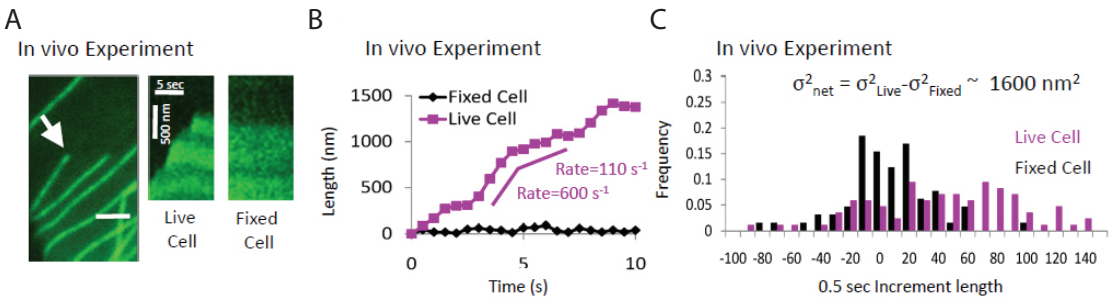

Figure 6.8: [Tub] and growth variability in vivo. This figure is further to Fig. 6.7. (A) Microtubule growth rates are measured near the cell periphery in both live and fixed LLC-PK1α cells to measure the variance in growth rate at 0.5 s intervals (green: GFP-tubulin). (B) Microtubule length as a function of time for live and fixed microtubules. Growing microtubules frequently shift the net rate dramatically on a time scale of seconds. In this example, the net rate shifts from 600 s^{-1} to 110 s^{-1} in a period of a few seconds. (C) *In vivo* microtubule growth rate variance is nearly 5-fold higher than GTP-tubulin in vitro data at 5 µM. In vivo growth rate variances are calculated by subtracting the fixed-cell measurement error variance from the live-cell data. Thus, the kinetic constants in vivo are at least as large as those estimated in vitro for GTP-tubulin at similar concentrations.

accompanying Gardner et al. [2011]). As shown in Fig. 6.8B, there is high variability in live-cell microtubule growth rates, consistent with previous reports [Shelden and Wadsworth, 1993]. With our high-resolution tracking accuracy (~36 nm) [Demtchouk et al., 2011], we can now readily detect nanoscale changes in microtubule length, including periods where the growth rate abruptly shifts (Fig. 6.8B). That the net rate is commonly ~600 s^{-1}, at least transiently, strongly suggests that the *in vivo* on-off dynamics are on the scale of 1 kHz. The *in vivo* variance in growth rate at 0.5 s intervals is ~1600 nm^2 (after subtracting the fixed microtubule variance), which is nearly 5-fold larger than the *in vitro* growth rate variance for GTP-tubulin microtubules at ~5 µM tubulin (downsampled to 0.5 s intervals). Thus, the kinetic rate constants *in vivo* are at least as large as we estimate for *in vitro* assembly.

6.3 Discussion

Using nanometer-resolution measurements, we confirm that microtubule assembly is highly variable and find this is due to the coordinate increase of both the on and off rates of tubulin with increasing [Tub]. By using GMPCPP-tubulin we demonstrated that the observed nanoscale variability is not the consequence of GTP hydrolysis-associated effects. The increasing off rate at higher concentrations is incompatible with a fundamental assumption of the classic 1D self-assembly model of Oosawa [1970], and requires a large revision of the rates of addition-loss during overall net microtubule growth (Fig. 6.9). Our analysis implies that the rates of tubulin addition-loss have been consistently underestimated in the literature by at least an order of magnitude. The analysis leads us to conclude that the on and off rates are nearly equal at experimental and physiologic [Tub], so that net microtubule assembly results from a modest difference between two large rates. This in turn implies that, in principle, a cell can significantly alter net microtubule assembly via relatively weak modification of the off rate, which was previously viewed as too small (relative to the on rate) to serve as a significant point of control over microtubule assembly.

To explain our results, we find that a 2D model that accounts for both longitudinal and lateral bonds in the microtubule naturally gives rise to an increasing off rate at higher [Tub]. The origin of this effect in the 2D model is the increasing tendency toward more tapered tips at higher [Tub], which we confirmed experimentally via TIRF microscopy (Fig. 6.6). We also found that the variability of microtubule assembly with GTP tubulin *in vitro* and *in vivo* is largely accounted for by the revised kinetic rates, which under typical conditions occur at kHz frequency. In summary, we found, using integrated experiments and computational modeling, that the kinetics of microtubule assembly are far more rapid than previously thought. In light of our findings, it will now be of interest to re-examine how microtubule assembly is regulated by MAPs and therapeutic drugs, such as the anticancer drug paclitaxel.

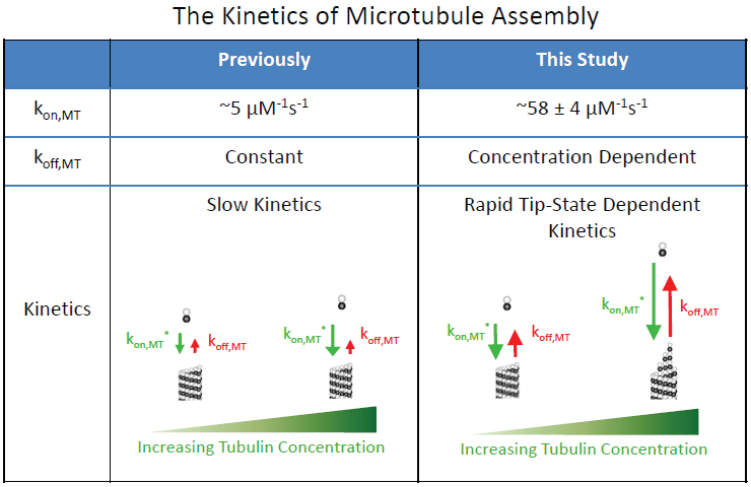

Figure 6.9: Revised view of microtubule assembly kinetics. By accounting for a non-homogeneous tip structure in a 2D model of microtubule assembly, we find that (1) the association rate constant for tubulin subunits during microtubule assembly is an order of magnitude higher than previously thought, (2) the tubulin subunit dissociation rate is not constant, as previously assumed, but rather increases at higher [Tub], and (3) microtubule assembly is driven by rapid on and off events of individual tubulin subunits, the rates of which increases with the increasingly tapered tip structures observed at higher [Tub]. Under typical assembly conditions, ∼10 μM GTP-tubulin, the combined kinetic rates are estimated to occur at nearly 1000 per second. At all [Tub] the association and dissociation rates are nearly equal to each other.

6.3.1 Relationship to previous studies

Previous studies have noted surprisingly high variability of microtubule assembly using relatively low resolution transmitted light microscopy imaging (≈100-150 nm resolution at ≈0.2-1 Hz) [Dye and Williams, 1996; Gildersleeve et al., 1992; Odde et al., 1996; Pedigo and Williams, 2002]. From the study of Dye and Williams [1996], it appeared that GTP hydrolysis was not responsible for the high variability, since their studies were conducted using GMPCPP-tubulin. However, the relatively low spatial and temporal resolution imaging techniques in this study limited the strength of the conclusions that could be drawn. In agreement with our findings, Dye and Williams proposed that the variability was likely due to structural configurations at the microtubule tip, but they did not identify the rapid kinetics and variable off rates from these lower resolution results. Recent advances in optical tweezers and digital fluorescence imaging have enabled measurement of microtubule assembly dynamics with nanoscale resolution at 1-10 Hz temporal resolution [Demtchouk et al., 2011; Kerssemakers et al., 2006; Schek et al., 2007]. Our previous study using laser tweezers to measure microtubule assembly from GTP-tubulin with 3.5 nm spatial resolution and 10 Hz temporal resolution revealed surprisingly large fluctuations in assembly at the nanoscale. The fluctuations presented themselves as substantial shortening episodes during periods of overall net growth, corresponding in many cases to multiple layers of tubulin dimers. However, these nanoscale-resolution studies examined GTP-tubulin assembly, leaving open the possibility for variability due to GTP hydrolysis [Howard and Hyman, 2009]. The present study now removes potential ambiguities due to either low resolution or GTP hydrolysis by reporting the first measurements of microtubule assembly in a single nucleotide state (GMPCPP) with nanoscale spatial resolution.

6.3.2 Possible alternative explanations for high variability in microtubule assembly

While the use of GMPCPP-tubulin, rather than GTP-tubulin, argues against hydrolysis-mediated fluctuations, the surprisingly large variability in assembly could potentially be explained without invoking rapid assembly kinetics.

We considered whether the mixed isotypes of tubulin, which was purified from bovine and porcine brain, might contribute to variability in growth owing to a distribution of thermodynamic parameters for different tubulin isoforms or tubulin with different post-translational modifications. However, in this case we would expect the variability to remain approximately constant with increasing tubulin concentration, since the concentrations of all isotypes would increase in constant proportion to the total tubulin concentration. However, we observed by both TIRF microscopy and by the laser tweezers assay that the variance increased with [Tub], arguing against a significant role of tubulin isotype heterogeneity. We note also that a recent study of variability in assembly found no significant differences between brain-derived β-tubulin isoforms [Rezania et al., 2008]. Similar arguments apply to trace contaminations from GTP and/or GDP in the β-tubulin subunit, rather than GMPCPP in the β-tubulin, as the relative proportions should remain constant with increasing [Tub]. In addition, our results with GTP-tubulin yield the same on-rate constant as obtained for GMPCPP-tubulin, and together show an increase in on-rate and off-rate across a 100-fold range of [Tub]. Finally, it has been shown that the fraction of GDP-tubulin necessary to appreciably alter microtubule assembly is $\sim$40% [Vandecandelaere et al., 1995].

In addition, while it is formally possible that defects incorporated into the lattice could contribute to the observed microtubule growth variability, it is not clear why there should be an increased fraction of defects between 0.8 and 1.5 µM GMPCPP-tubulin, as the growth rate is only marginally more rapid at 1.5 µM as compared

to 0.8 µM ($3.4\,\mathrm{nm\,s^{-1}}$ and $2.4\,\mathrm{nm\,s^{-1}}$, respectively). We also note that defects are relatively rare, with estimates ranging from ∼1 per µm [Davis et al., 2002] to 1 per 4 µm [Chrétien et al., 1992]. Therefore, defects are expected to be too rare (< 1 per 1600 subunits) to be the dominant source of variability.

It could be argued that thermal fluctuations of the leading protofilaments could drive the observed length fluctuations, but the expected deformations based on the mechanical stiffness of protofilaments would be too small to give rise to the observed variance, as described previously [Elie-Caille et al., 2007; Kerssemakers et al., 2006; Schek et al., 2007]. The consistency of the laser tweezers and TIRF experiments also argues against this possibility.

6.3.3 The 2D model for microtubule assembly

While it is possible to construct complex alternative explanations for variability in assembly, the 2D model [VanBuren et al., 2002] provides a physically direct and simple explanation. It also predicts that tips will be more tapered at higher [Tub], which we confirmed experimentally for GMPCPP-tubulin, and has previously been observed for GTP-tubulin in cryo-electron microscopy studies [Chrétien et al., 1995].

The 2D model provides a link between the structural observation of increasing taper at higher [Tub] and the increasing off rate. The off rate increases at high [Tub] because the protofilaments grow more autonomously from each other due to the greater frequency of addition events, which do not depend on the neighbor's state. The resulting variability in protofilament length increases the frequency of subunits with 1-neighbor (i.e., tapered) relative to subunits with 2-neighbors (i.e., blunt) at the tips of each protofilament. Thus, while the 1D model is appealing in its simplicity, it is inadequate to explain the variability in microtubule assembly. By contrast, the 2D model explains both the mean and the variance in microtubule assembly, as well as the longer microtubule tip taper at higher [Tub].

One might wonder whether the transient binding events that we detected are perhaps not productive in the sense that they may not contribute to GTP hydrolysis. However, because of the stochastic nature of thermal forces, it is not possible to predict how long a given subunit will remain in a microtubule after it has added at the tip. Given our current lack of understanding of the hydrolysis reaction, it is possible that every addition event could potentially stimulate hydrolysis of GTP-tubulin. Therefore, in order to understand the hydrolysis reaction it is important to first establish a firm understanding of the subunit addition-loss kinetics. Our findings strongly support the use of a 2D assembly model for further investigation of microtubule dynamics, including the hydrolysis reaction.

6.3.4 Implications for the Regulation of Microtubule Dynamics by MAPs and Drugs

The finding that tubulin association and dissociation rates are substantially higher than has been previously recognized significantly changes the conceptualization of microtubule growth. For example, under typical GTP-tubulin concentrations of 10 µM *in vitro*, we estimate an on rate $k^*_{\mathrm{on,MT}} = 520\,\mathrm{s}^{-1}$ and an off rate $k_{\mathrm{off,MT}} = 480\,\mathrm{s}^{-1}$, for a net rate of $40\,\mathrm{s}^{-1}$ ($1.5\,\mu\mathrm{m\,min}^{-1}$) (Fig. 6.7E). Thus, the total number of events is about $1000\,\mathrm{s}^{-1}$. These estimates stand in marked contrast to previous kinetic rate constant estimates, which would yield an order of magnitude lower on rate of $k^*_{\mathrm{on,MT}} = 50\,\mathrm{s}^{-1}$ at 10 µM GTP-tubulin and a fixed off rate of $k_{\mathrm{off,MT}} = 10\,\mathrm{s}^{-1}$. In addition, our analysis and experiments imply that the on rates and off rates are nearly equal at all [Tub], and the net microtubule growth rate is a small difference between similarly large association and dissociation rates.

The near equality of on and off rates implies that infrequent and/or weak suppression of the off rate should lead to dramatic shifts in net assembly for single microtubules *in vivo*. Using our nanoscale resolution image analysis, which has single

time-point accuracy of 36 nm in LLC-PK1α cells [Demtchouk et al., 2011], we can now see that such shifts are in fact the norm in living epithelial cells. As shown in Fig. 6.8A, a growing microtubule shifts from a net rate of $600\,s^{-1}$ to $110\,s^{-1}$ in a matter of a few seconds. This sequence clearly shows a "hypersensitivity" of assembly, where the net growth state fluctuates wildly, perhaps due to weak and infrequent interactions with MAPs.

The near equality of on and off rates also implies that a slight tipping of the balance by a single MAP at the microtubule tip might significantly affect catastrophe and rescue *in vivo*. For example, weak suppression of the off rate by a stabilizing MAP would lead to a rapid and significant increase in the microtubule GTP-cap size, and a corresponding substantial decrease in catastrophe frequency. Furthermore, a much larger off rate allows a substantial range of growth regulation to be exerted purely through suppression of tubulin loss from the microtubule tip. This has important implications for explaining how a MAP such as XMAP215/chTOG, which is overexpressed in colon and hepatic tumors, promotes assembly. Growth rates *in vivo* and with this MAP *in vitro* are commonly 2-10 fold higher than with pure tubulin at $\sim 10\,\mu M$ GTP-tubulin [Cassimeris et al., 1988; Charrasse et al., 1998; Pryer et al., 1992; Rusan et al., 2001; Shelden and Wadsworth, 1993; Vasquez et al., 1994]. In the context of the 1D model, a 10-fold increase in growth rate can only be achieved by increasing the on rate because, for example, suppressing tubulin dissociation entirely (i.e., decreasing the off rate from $10\,s^{-1}$ to $0\,s^{-1}$) would only achieve a 25 % increase in net assembly rate. However, in the 2D model, a ten-fold increase in net growth rate by a MAP can be achieved simply by suppressing the off rate by a factor of two. Such a mechanism of growth enhancement is similar to that proposed by VanBuren et al. [2002] and Brouhard et al. [2008] to account for the 5-fold acceleration of growth rate by XMAP215.

Other possible examples include the neuronal MAPs, tau and MAP2, which pro-

mote microtubule assembly *in vitro* at sub-stoichiometric concentrations [Drechsel et al., 1992; Pryer et al., 1992]. This could then be important in maintaining the neuronal phenotype without requiring high MAP expression levels.

Conversely, a weakly destabilizing MAP would be expected to tip the balance strongly toward catastrophe. The best understood catastrophe-promoting MAP, MCAK, seems to at least partly fulfill this description. The catalytic effect of MCAK is to increase the tubulin off-rate by 100-fold [Hunter et al., 2003], which corresponds to a modest free energy increase of $\Delta G^0 = \ln 100 = 4.6 k_{\mathrm{B}}T$. Interestingly, this energy turns out to be nearly equal in magnitude to our estimate of the lateral bond energy in the 2D model ($-4.5 k_{\mathrm{B}}T$ to $-5.0 k_{\mathrm{B}}T$; Table 6.2). In addition, MCAK's catalytic effect on the off-rate is only weakly cooperative, so that even a single molecule is able to affect the off-rate (Hunter et al., 2003). The *in vivo* expression level of MCAK is crucial to maintenance of proper ploidy, which is important to avoid progression into a cancerous phenotype [Bakhoum et al., 2009a,b].

One example of high sensitivity to limited numbers of MAPs *in vivo* is the length-dependent disassembly of budding yeast kinetochore microtubules mediated by kinesin-5 motors, Cin8p and Kip1p, which establishes the congressed state characteristic of metaphase mitotic spindles [Gardner et al., 2008b]. In the metaphase budding yeast spindle, there are an estimated 40 microtubules and 50 kinesin-5 motors bound to the spindle [Gardner et al., 2008b; Winey et al., 1995]. This ∼1:1 microtubule:motor stoichiometry implies that even a single kinesin-5 motor at the plus end has a significant impact on the microtubule assembly state. From modeling studies, it was estimated that the presence of a single motor at the plus end was sufficient to promote catastrophe ∼10-fold [Gardner et al., 2008b]. Given that metaphase yeast kinetochore microtubules contain on average about 600 tubulin dimers, the effect of the motor can be regarded as even more potent, with about one motor per ∼600 tubulin dimers.

Slight tipping of the balance between addition and loss may play a role in rescue as well. For a rapidly disassembling microtubule *in vitro*, the net shortening rate is $\sim -30\,\mu\mathrm{m\,min^{-1}}$ ($-500\,\mathrm{nm\,s^{-1}}$), or $-800\,\mathrm{s^{-1}}$ [Walker et al., 1988]. In this case, we estimate that at $10\,\mu\mathrm{M}$ GTP-tubulin the on rate is $\sim 600\,\mathrm{s^{-1}}$, so the off rate is $1400\,\mathrm{s^{-1}}$, or about a 2-fold difference. This stands in marked contrast to the 1D model, which views the same $-800\,\mathrm{s^{-1}}$ net disassembly rate as being due to an on rate of nearly zero and an off rate of $800\,\mathrm{s^{-1}}$. The 1D model explanation is problematic, as it implies that the on rate, which is presumably driven by translational and rotational diffusion of subunits [Northrup and Erickson, 1992], suddenly goes to zero once catastrophe has begun. With the 2D model, it now becomes relatively easy to understand how rescue can occur in the absence of MAPs or drugs (because the on rate is not near zero in the 2D model), and furthermore how these agents can in turn alter the rescue rate under substoichiometric conditions.

Hypersensitivity of assembly can also potentially facilitate rapid cell-wide microtubule array reorganization. A prime example of a dramatic microtubule reorganization process is Drosophila embryo mitosis, where a mitotic spindle forms, segregates a genome, and subsequently disassembles in a matter of minutes [Stiffler et al., 1999]. Such dramatic transitions *in vivo* occur under conditions of fixed total tubulin concentration, which serves to buffer perturbations to net assembly [Mitchison and Kirschner, 1987]. For example, if an assembly-promoting MAP is upregulated, then the initial response will be potent. However, as net assembly is promoted, the free concentration will drop, which will mitigate the assembly-promoting activity. Thus, constant total tubulin concentration will act to buffer and mitigate perturbations to microtubule dynamics, and confer a degree of robustness and homeostasis on the microtubule cytoskeleton. To overcome the built-in cell-level buffering effect and perform highly dynamic operations such as mitosis, the microtubule array needs to be hypersensitive.

To summarize, it will be important to revisit current models for microtubule regulation *in vivo* via MAPs and therapeutic drugs in light of our findings. In particular, because both on and off rates are rapid and nearly equal, MAPs that promote net microtubule assembly could work through a modest suppression of tubulin subunit off-rates [Brouhard et al., 2008; Murphy et al., 1977; Pryer et al., 1992; VanBuren et al., 2002, 2005].

6.3.5 Implications for Other Multi-stranded Filaments

More generally, our results identify a fundamental theoretical limitation to the 1D model of Oosawa, which has been used for nearly 40 years to interpret kinetic self-assembly data of microtubules, F-actin, viruses, and amyloid aggregates [Cannon et al., 2004; Collins et al., 2004]. It will be important to revisit earlier 1D model-based studies to confirm that the assumption of constant subunit dissociation rate holds for self-assembled polymers containing both longitudinal and lateral interactions, since presently established kinetic estimates for these biological assemblies may need to be revised as we have found with microtubules.

6.4 Methods

6.4.1 Tweezers experiments

A microtubule linked to a 0.57-µm diameter silica bead was trapped by optical tweezers and oriented toward a microfabricated barrier. A weak force clamp was applied (∼0.2 pN) to abut the microtubule against the barrier. Schek et al. [2007] (their Fig. 6B) showed that the applied force of 0.2 pN has only a modest effect on the net growth rate. Experiments were conducted at 34 °C. In the laser-tweezer experiments, we detect microtubule length changes without large variability at 0.5 µM GMPCPP tubulin, and then observe increasing growth variability with increasing GMPCPP

tubulin concentration. Therefore, the laser-tweezer data is internally controlled by using a range of GMPCPP-tubulin concentrations.

6.4.2 TIRF microscopy experiments

Assembly of GMPCPP-Tubulin labeled with Alexa-488 (55% labeled, Invitrogen Corp.) onto Rhodamine-labeled GMPCPP-Tubulin seeds was imaged by TIRF microscopy as described [Gell et al., 2010]. Images were collected with an Andor iXon camera on a Zeiss Axiovert 200 M microscope using a Zeiss100X/1.45 NA Plan FLUAR objective. A 2.5X Optovar was used to provide additional magnification and to limit pixel size to 64 nm. An objective heater was used to warm the flow channel to 35 °C for GMPCPP experiments. Although the time-lapse interval for collecting images was 700 ms, all of the images were collected at 100 ms exposure times, regardless of concentration. GTP experiments were performed at 1 mM GTP at 30 °C. At higher tubulin concentrations where the growth rate becomes rapid, we found that the drift term is dominant even over short times, and the diffusive term is difficult to accurately estimate within the experimental TIRF data temporal resolution.

Fixation experiments were performed by flowing in a mixture of BRB80 with 0.05% Glutaraldehyde once microtubule extensions achieved the appropriate length. Similar tip structure distributions were used for each concentration to accurately compare fixed and live microtubule growth increments.

6.4.3 Simulations

Simulations were performed as described Schek et al. [2007]; VanBuren et al. [2002] with a hydrolysis rate of zero. For the rare cases where a lagging protofilament had two longer neighboring protofilaments, we also included an on-rate penalty to account for steric hindrance. Here, the on rate constant was described as $k_{\mathrm{on,PF}}/\delta$, where δ is the on-rate penalty.

CHAPTER VII

Summary and recommended future directions

7.1 Summary

The present work demonstrates a new assay for probing the mechanics of a mitotic spindle pole and provides, to our knowledge, the first measurements of the mechanics of isolated spindle poles. We find that microtubules undergo bidirectional motor-driven movement and are attached to the pole by cross links (which may be motors) that have a compliance suited to spindle-pole attachment. We also find that the kinesin-5 Eg5 decreases pole compliance.

The present work also provides evidence that the exchange of $\alpha\beta$-tubulin subunits at the tips of microtubules is an order of magnitude faster than has generally been believed, with the net growth rate resulting from high on and off rates that are roughly equal. Models of subunit exchange must, unlike the 1D Oosawa model, take into account differences in lateral interactions between subunits at the tip in order to provide an adequate description of microtubule polymerization.

7.2 Recommended future directions

7.2.1 Mechanics of the mitotic spindle

The data on the mechanics of asters suggest new avenues of investigation. Several established biochemical depletions [Chakravarty et al., 2004] were not attempted in this study. For comparison across species, a study of asters formed in *Xenopus* extracts [Ohba et al., 1999] may yield important new data, though such extracts may not be appropriate for optical trapping due to excessive debris (Henry Schek, personal communication). A study of the mechanics of centrosomes might yield new insight into their mitotic functions. For instance, they might be found to be far stiffer than HeLa mitotic asters, suggesting that they act as the firm anchors of the spindle while compliant acentrosomal connections provide malleability. Effects of centrosome mutations and changes in centrosome mechanics over the course of their maturation in the cell cycle might also be of interest. Finally, a study of asters formed from simple sets of purified components [Hentrich and Surrey, 2010; Surrey et al., 2001] would allow a more quantitative reductionist approach in which mechanics could be related to the concentrations of components present. (For mitotic extract studies, complete depletion of a component and partial restoration of its concentration by exogenous addition might also be of interest.)

7.2.1.1 Technical considerations

To obtain stiffness and drag coefficient for any aster (as opposed to only those with fortuitous breakage events), it should be possible cause an exponential jump in position by abruptly changing the applied force. This would complement or replace the thermal noise approach.

An alternative protocol in which beads are attached to asters by mixing before addition to the experimental chamber should be considered. The advantage of such an

approach would be ease of assay execution and, therefore, increased data collection. The disadvantage would be inferior estimation of the equilibrium bead position in the trap and, therefore, of applied force.

7.2.2 Microtubule polymerization dynamics

The effect of buffer conditions, an isoform change, or the presence of a MAP or drug on $k_{\mathrm{on,MT}}$ and $k_{\mathrm{off,MT}}$, obtained from D_{p} and $\hat{v}_{\mathrm{g}}$, may yield information about its mechanism of action. (Also of interest would be its effect on surface roughness, related to its effect on $\Delta G_{\mathrm{Lateral}}$.) Considering that some differences between tubulin isoform sequences tend to be located in regions of lateral contact, it would be interesting to predict by analysis of sequence and structure, and also by computation [Mitra and Sept, 2008; Sept et al., 2003], which isoforms would have the strongest and weakest lateral interactions, and to assess experimentally whether these isoforms differ in their polymerization dynamics and their tip structure. The MAP doublecortin appears to have little effect on the mean or variance of $\hat{v}_{\mathrm{g}}$, which suggests it may not affect $k_{\mathrm{on,MT}}$ and $k_{\mathrm{off,MT}}$ [Moores et al., 2006]. In contrast, in one study, tau appears to have increased both the mean and the variance of $\hat{v}_{\mathrm{g}}$, which would seem to suggest an increase in both $k_{\mathrm{on,MT}}$ and $k_{\mathrm{off,MT}}$ Drechsel et al. [1992], though increasing the (presumably nearly diffusion limited) $k_{\mathrm{on,MT}}$ seems unlikely. In neither of these studies were the authors focusing on analysis of the variance of $\hat{v}_{\mathrm{g}}$, and precise estimation of $k_{\mathrm{on,MT}}$ and $k_{\mathrm{off,MT}}$ requires D_{p} and $\hat{v}_{\mathrm{g}}$ from root-mean-squared length increment analysis. Studies on the effects of microtubule-targeted drugs Jordan and Wilson [2004] may find that their mechanism of action includes, for instance, suppression of $k_{\mathrm{on,MT}}$ and $k_{\mathrm{off,MT}}$, which would suggest the importance to mitosis of rapid subunit exchange.

A natural extension of Chapter VI is to observe the evolution of tip structure over time by TIRF microscopy and attempt to correlate events in this evolution

with catastrophe. This has been done by cryoelectron microscopy [Chrétien et al., 1995] in a population-based approach that does not allow observation of a change in the structure of one tip that is followed by catastrophe. Catastrophe kinetics are consistent with a multistep process [Odde et al., 1995], so it would be reasonable to hypothesize that one of these steps involves evolution of tip structure. For instance, that blunting may be correlated with catastrophe, as suggested by Arnal et al. [2000], was contradicted by the simulations of VanBuren et al. [2005] and is inconsistent with the experiments of Höög et al. [2011]. Considering Fig. 4.9A and C (p. 4.9), it may be difficult to predict whether an initially blunt or tapered tip would be more stable as the tip structure develops over time. For the tapered tip (C), a large fraction of the GTP subunits have one lateral neighbor and, therefore, a high dissociation rate; on the other hand a large fraction of vacancies have a neighbor so that new subunit additions would be relatively stable, in contrast to the many futile additions to a blunt tip. The VanBuren et al. [2005] simulations indicate the blunt tip should be more stable (the authors suggested that the tips Arnal et al. identified as growing were actually rapidly shortening). Supporting this lack of correlation, the tips observed by Höög et al. [2011] were relatively blunt, but it is difficult to interpret these results because they were obtained in cells in which MAPs may be assumed to have had a pronounced effect. In the event that, in agreement with Arnal et al. [2000], blunting is correlated with catastrophe, it may be interesting to consider that the tips observed by Höög et al. [2011] were also curved. That curvature might reduce hydrolysis rate has been given some consideration [Howard, 2001], with indirect evidence obtained by Wang et al. [2007], and this might resolve the disagreement: blunting would be correlated with catastrophe because the subunits in a blunt tip cannot fully close the tip and simultaneously have outward curvature, whereas a tapered tip would contain subunits partially protected from hydrolysis due to their curvature. However, this is highly speculative.

Direct measurement of subunit exchange would be possible with an assay* similar to that of Needleman et al. [2010] combined with more conventional TIRF microscopy microtubule polymerization assays Gell et al. [2010], in which the fraction of subunits labeled is low enough to resolve individual association and dissociation events. Association and immediate dissociation of zero-neighbor subunits would probably not be observable, but a portion of the distribution of subunit lifetimes could be obtained, particularly for low [Tub] in the presence of GMPCPP. It might be useful to repeat observations at varying illumination intensity to assess the effects of photobleaching. An advantage of this assay is that it would provide one of the most direct possible observations of fast subunit exchange, independently verifying the conclusions of Chapter VI. The Oosawa 1D model would predict loss of signal due primarily to photobleaching, whereas the 2D model would predict a broad distribution of subunit lifetimes. This assay would also allow further validation of VanBuren-type simulations. Mirny and Needleman [2010] provide a biased-random-walk framework for subunit lifetime (here, the time for the random walker to return to the origin) that predicts mean lifetime given by $4D_{\mathrm{p}}/\hat{v}_{\mathrm{g}}^2$. In a related assay with a much higher labeling ratio, it might be possible to assess fluctuations in exchange rate based on fluorescence intensity.

A review of the literature will reveal studies in which conclusions are based on tubulin subunit exchange rates obtained using the Oosawa model. These conclusions may need to be revised. For instance, Caplow and Shanks [1996] base one of their arguments on the assumption the number of subunits added to the tip in an incubation should not be sufficiently variable to explain variability in cap lifetime, but a rough calculation suggests this argument may, based on the present work, not be valid.

*The possibility of this assay was described to me by Edgar Meyhöfer.

7.2.2.1 Technical considerations

A large fraction of the computational expense in VanBuren-type simulations is presumably due to futile zero-neighbor addition-loss events that shorten the variable-length timestep. It may be useful to reduce computational expense by replacing zero-neighbor additions with pair additions, the statistics of which would be determined by theory or by simulation. However, implementation, if valid, would be complicated and would make the model less elegant.

It may be advantageous to fabricate barriers entirely out of glass, making fine features by femtosecond-laser machining. The arbitrary geometry made possible by laser machining would allow a design in which a much shorter microtubule could be used, allowing the application of higher forces and, for experiments at lower forces, increasing success rate because a larger fraction of microtubule-linked beads found would be useable. In the case experiments in the presence of microtubule stabilizers, this would also increase the quantitity of data collected because one could start with the shortest possible microtubule and allow it to grow as long as practically possible. These all-glass barriers might also have longer shelf life and be reusable, whereas LOR3B/SU8 barriers seem to become sticky after 1.5 to 2 weeks, possibly due to delamination. A further advantage of glass is that adjustment of its surface chemistry is well established, and the barrier would be made of 1 material instead of 3. However, if gross features in the all-glass (or quartz) barriers are made by hydrofluoric acid etching, it might make the glass unsuitable for microscopy and trapping.

The mask presently used for barrier fabrication is the original mask from the earliest stages of development of the barrier assay. A redesign of the mask would be a cost-effective way to increase throughput. This mask current is patterned far more densely than is necessary, and this makes it more difficult to trap beads at depths of tens of µm, which likely increases the failure rate of experiments. Furthermore, the barriers are triangular, with a back wall that serves no purpose but tends complicate

positioning of a microtubule in the barrier; a diamond shape may be more appropriate.

Not entirely explicit in the present work are two recommended technical adjustments: The piezoelectric mirror that steers the trapping laser focus in the focal plane is provides analog strain gage sensor monitoring output. These have been recently connected so that mirror position changes can be recorded in all experiments. There are two advantages of doing so: it makes explicit to the user whether the mirror's dynamic response is adequate for the experiment being performed, and it may reveal failure of the piezo-controlled mirror or amplifier before resources are wasted attempting assays. For instance, a large data set was recently discarded due to noise issues, and it later became apparent that the piezo mirror was oscillating due to malfunction of its power supply. A second adjustment is the collection of raw video data rather than background-subtracted video data, allowing vastly superior automated drift-tracking in barrier experiments. Background-subtracted video allows visualization of the microtubule but because the barrier is part of the background image (this is likely unavoidable), its drift becomes difficult to track automatically in background-subtracted images.

This section has summarized a small sample of the possible avenues of future investigation and made technical recommendations.

APPENDICES

APPENDIX A

Mechanics of Mitotic Asters: supplementary data and discussion

A.1 A simple model of pole compliance and force transfer

Strictly speaking the data of Chapter III does not address flux, as the microtubules in the asters are not dynamic. However, it is useful to consider how the compliances we observe could influence flux, while recognizing that asters are a model system that does not capture all aspects of spindle poles (e.g., centrosomes and dynamic microtubules). We therefore restrict the following discussion to "order of magnitude" arguments. As depicted in Fig. 3.4A (p. 45), compliant cross-links spanning between microtubules fluxing poleward will distribute loads such that the speeds of microtubule movements become similar. However, the ability of fluxing microtubules to bear loads ultimately depends on transfer of these loads to the relatively stationary overall structure of the pole: the microtubules must be anchored to the pole, even if the anchors are dynamic, and the location of the pole within the cell is relatively immobile. To mediate force transfer between continuously fluxing microtubules and the relatively stationary pole, cross-links must periodically detach, rearrange to relieve

accumulated strain, and rebind. Moreover for the poles to maintain their structure in quasi-steady-state, the rate of detaching must approximately equal the rate of rebinding (see discussion of equation (A.1) below).

As discussed in section 3.2.5 (p. 43), for the compliance we observe the cross-links between a fluxing microtubule and relatively immobile components must detach after, on average, about one second (for flux at 10 nm/s) to avoid loads that would substantially slow a typical motor protein. To illustrate the importance of compliance for maintaining the structure of the pole, consider what happens if the compliance were abruptly decreased 10-fold, similar to an actomyosin cross-bridge. Stress would build more quickly, and the detachment rate would have to increase 10-fold to avoid slowing microtubule movements. This would in turn decrease the time that the cross-links are bound by a factor of 10, and similarly decrease the effectiveness of force distribution. Furthermore the large fraction of time that the cross-links are unbound will increase the likelihood that the microtubule can be pulled out of the pole altogether. Thus the stiffness must be matched to the other physical characteristics to maintain the polar architecture. Possibly a different compliance could be accommodated by changing the structure of the pole (e.g., such that the steady-state number of cross-links is restored), and this may in part explain pronounced changes in structure that accompany disruption of spindle components that cross-link microtubules [Gaglio et al., 1995, 1996, 1997; Mountain et al., 1999].

A more quantitative treatment of these arguments follows. To obtain an expression for the number of cross-links at steady state, suppose there are N possible cross-links, of which N_a are attached, and suppose attachments form at rate $(N - N_\mathrm{a})\, k_\mathrm{on}$ and detach at rate $N_\mathrm{a} k_\mathrm{off}$. At steady state, these rates are equal, so number of attachments, N_ss, is given by:

$$N_\mathrm{ss} = N k_\mathrm{on}/(k_\mathrm{on} + k_\mathrm{off}) \tag{A.1}$$

Initially we consider the behavior of a single cross-link to obtain expressions for how

transmitted force is affected by cross-link stiffness, κ; motor speed, v_1; maximum motor force, $F_{\max}$; and the maximum force cross-links can bear, $F_{s\max}$. Consider Fig. 3.4A (p. 45) without motor 2 and with microtubule 2 fixed. Motor 1 moves microtubule 1 at speed $v_1 > 0$ (so the x axis is inverted). We assume the cross-link is a Hookean spring with stiffness κ, stretched by a force F_s. Suppose that as microtubule 1 moves, the cross-link is stretched so F_s increases from 0 to $F_{s\max}$, at which point the cross-link detaches from one of the two microtubules, relaxes, and reattaches at a different position with F_s =0. The resulting F_s *vs.* time (or transmitted force *vs.* time) curve would consist of cycles (Fig. A.1) in which F_s rises, abruptly drops to zero, and rises again. The downward curvature reflects the motor(s) slowing as the force builds. The average amount of time the cross-link is attached in one cycle is given by $\tau_{\rm a} = 1/k_{\rm off}$, and $\tau_{\rm d} = 1/k_{\rm on}$ is the average time it is detached. If $\langle F_s \rangle_{\rm a}$ is the average stress on the cross-link when it is attached to both microtubules then the time-averaged force transmitted from one microtubule to the other is

$$F_T = \frac{\langle F_s \rangle_{\rm a}\, \tau_{\rm a}}{\tau_{\rm a} + \tau_{\rm d}} = \frac{\langle F_s \rangle_{\rm a}}{1 + \tau_{\rm d}/\tau_{\rm a}} \tag{A.2}$$

Following the approximately linear force versus speed relations that have been observed for single motor proteins, we assume motor speed decreases with force according to:

$$v_1 = v_{1\,\max} \left(1 - \frac{F_s}{F_{\max}}\right) \tag{A.3}$$

where $v_{1\max}$ is the unloaded motor speed, $F_{\max}$ is the force at which motor speed reaches zero, and $F_s \geq 0$ is the inhibitory load on the motor due to the cross-link (= $\kappa\xi$ where ξ is the strain of the cross-link). If a cross-link attaches at time $t = 0$ with strain $\xi = 0$, using $dx = v_1 dt$ and $dx = d\xi$, we have

$$\frac{d\xi}{dt} + \frac{v_{1\,\max}\kappa}{F_{\max}}\xi = v_{1\,\max} \tag{A.4}$$

Solving equation (A.4) and multiplying by κ to obtain the spring force yields

$$F_s(t) = F_{\max}\left(1 - e^{-v_{1\max}\kappa t/F_{\max}}\right) \tag{A.5}$$

The average spring force during the attached time τ_a is

$$\langle F_s \rangle_a = \frac{F_{\max}}{\tau_a}\int_0^{\tau_a}\left(1 - e^{-v_{1\max}\kappa t/F_{\max}}\right)\mathrm{d}t = F_{\max} + \frac{F_{s\max}}{\ln\left(1 - F_{s\max}/F_{\max}\right)} \tag{A.6}$$

From equation (A.6), the mean force stretching the cross-link while it is attached depends on the maximum force the motor can generate and on the force at which the cross-link detaches. Noting that $F_{s\max} = F_s(\tau_a)$, we obtain from equation (A.5) that

$$\tau_a = -\frac{F_{\max}}{v_{1\max}\kappa}\ln\left(1 - \frac{F_{s\max}}{F_{\max}}\right) \tag{A.7}$$

From equation (A.7), since $\tau_a \propto 1/\kappa$, an order of magnitude change in stiffness would cause an order of magnitude change in attachment time. This would result in either failed aster formation or aster formation at a new steady state. Thus the specific steady state structure of an aster depends on the values of $\kappa v_{1\max}$, $F_{s\max}$, and $F_{\max}$.

Consider a microtubule attached to the aster via one cross-link. From equation (A.7), assuming $F_{\max} = 7\,\mathrm{pN}$, $F_{s\max} = F_{\max}/2$, $\kappa = 0.025\,\mathrm{pN/nm}$, and $v_{1\max} = 30\,\mathrm{nm/s}$, we have $\tau_a \approx 6\,\mathrm{s}^{-1}$ *. This is long enough to allow the motor to move the microtubule a substantial distance, but short enough to allow rearrangements quickly relative to the timescale of mitosis. More consistent with our estimate of a handful of cross-links would be, say $N_{ss} = 5$, and the stiffness would be divided between these. Taking $k_{off} = 1/\tau_a$, the overall steady-state detachment rate is $k_{off}N_{ss} \cong 1\,\mathrm{s}^{-1}$, and new attachments must form at this same rate. To get a feeling for the sensitivity of the polar

*Here we assume $F_{\max}$ consistent with one or two motor proteins, in keeping with our estimate of a handful of cross-links total, including cross-links formed by motors. $F_{s\max}$ is taken as half this value since flux does not exhibit overt variations in speed, suggesting the load on the motors rarely approach the stall force. $v_{1\max}$ was chosen to be similar to the speed of flux or unloaded Eg5.

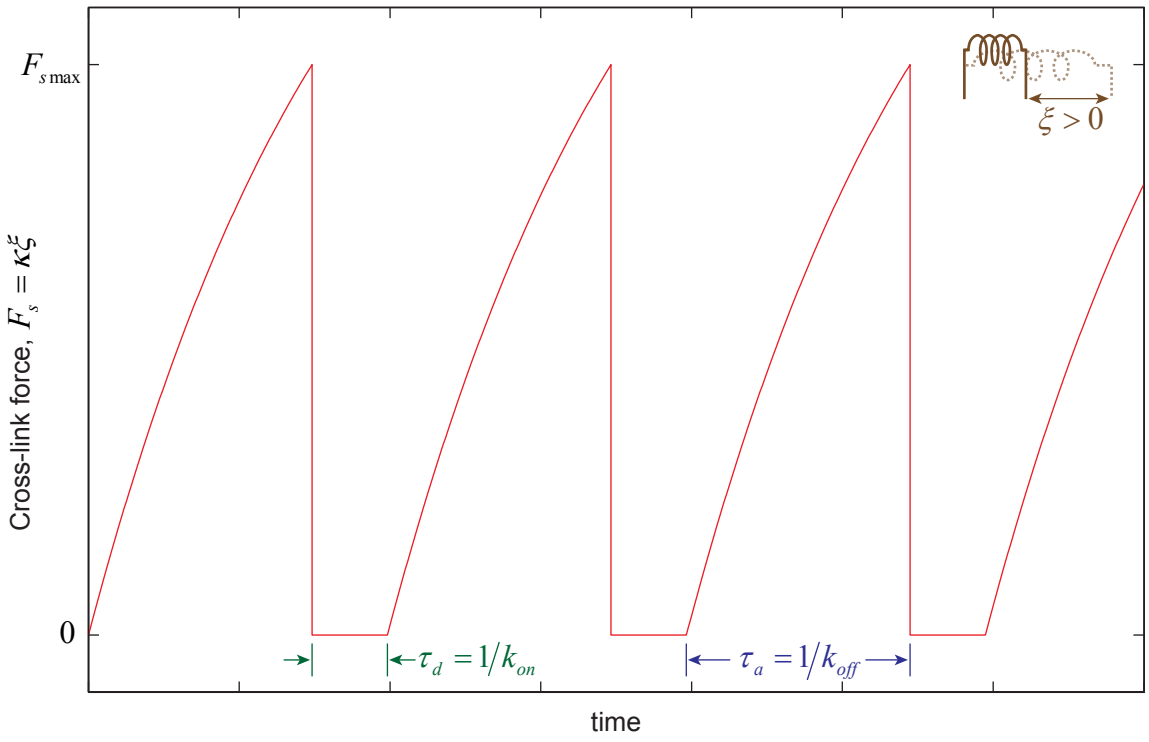

Figure A.1: Quantitative model of force transfer. Cross-link force, F_s, vs. time over cycles of detachment and reattachment based on the supplemental discussion of force transfer; see equations (A.5)-(A.7). As a motor moves one microtubule relative to the other, the inhibitory force, F_s, due to the cross-link between them slows the motor. When F_s reaches $F_{s\max}$, the cross-link detaches and, after time τ_{d}, reattaches. Inset: graphical depiction of ξ.

structure to cross-link stiffness, consider the effect of an order of magnitude change. An order of magnitude increase in stiffness would reduce τ_{a} and increase k_{off} such that the average number of cross-links N_{ss} would drop below one, severely compromising the transfer of loads between microtubules to the point where loaded microtubules would frequently detach from the pole, if the structure of pole could be maintained at all. Note however that the distribution of cross-links might shift so that the rate of attachment increases, or the microtubules might rearrange so that more microtubule lengths come in close proximity to accommodate more cross-links. Thus compliance changes might be accommodated by changing the structure of the pole, though it is not possible to predict the nature of such a structural change without more information on the spindle structure and the kinetic behaviors of the cross-links. An order of magnitude reduction in compliance would not compromise force transfer, but the attached time would increase to $\tau_{\mathrm{a}} \approx 60$ s, over which time the cross-link would be strained about 2 µm. It is difficult to envision that any of the known nanometer-scale cross-linking proteins could be strained this much, and such large distortions of the polar structure are not observed in our assays or during mitosis. Thus we conclude that the observed stiffness is well-matched to maintaining the structure of the pole – substantially different stiffness would either result in failure to form or maintain a microtubule focus, or produce substantial alterations of the overall structure and/or cross-link dynamics at the pole.

A.2 Supplemental data

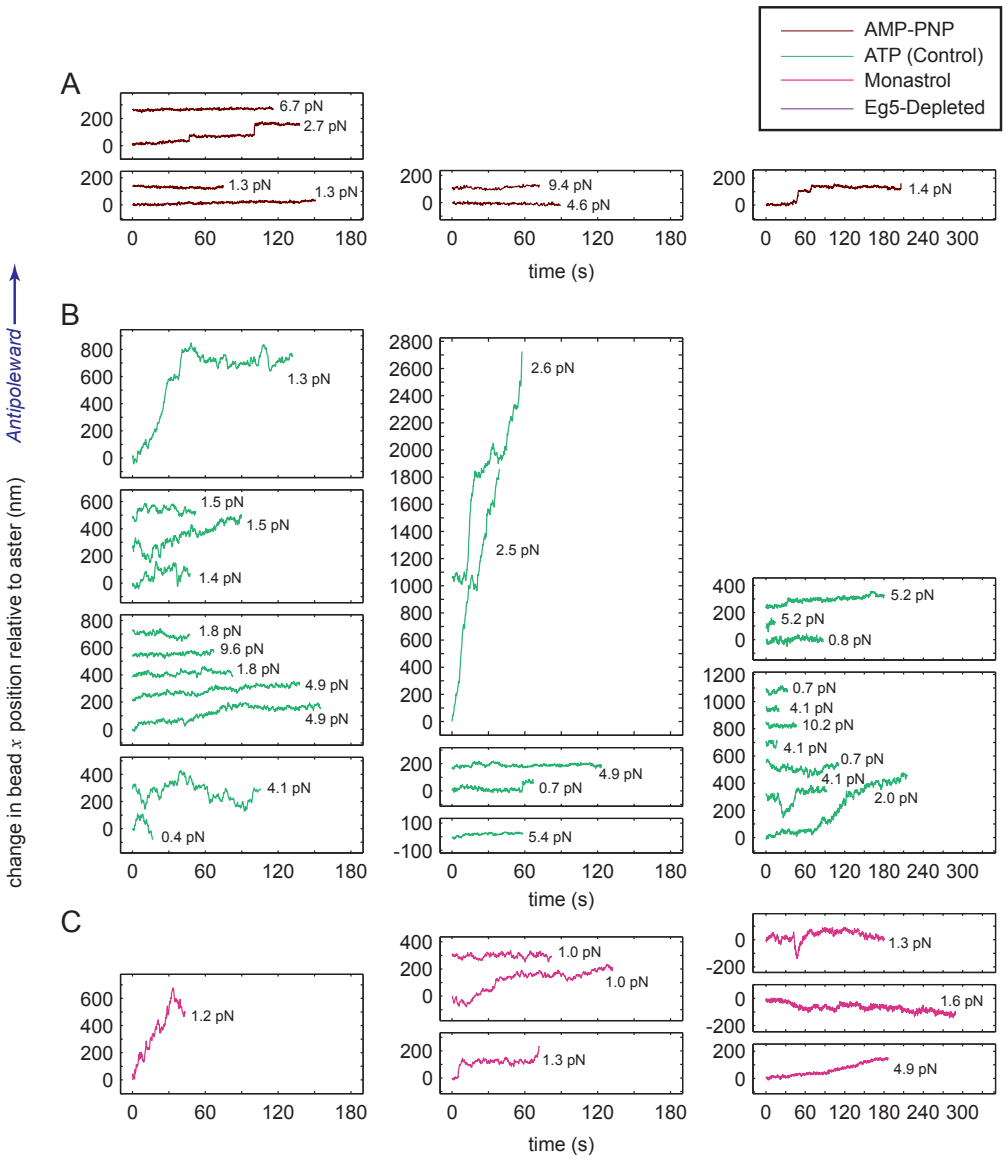

Figure A.2: Position *vs.* time traces for ATP, AMPPNP, monastrol. Color coding of experimental conditions as in Figs. 3.2 and 3.3A, p. 32 and 37. Position vs. time, formatted as Fig. 2a with each set of axes corresponding to one aster for (A) AMP-PNP, (B) ATP (control), (C) monastrol. Each set of axes contains a set of plots from one aster in sequence, beginning with the earliest trace at the bottom. These asters correspond to those used for stiffness analysis (Fig. 3.3A) except that 3 were not used for Fig. 3A because pre-attachment data were not available. The force applied by the optical trap for each is also marked. In some cases we changed the applied force between subtraces, but this did not have any obvious effects over the range of forces applied.

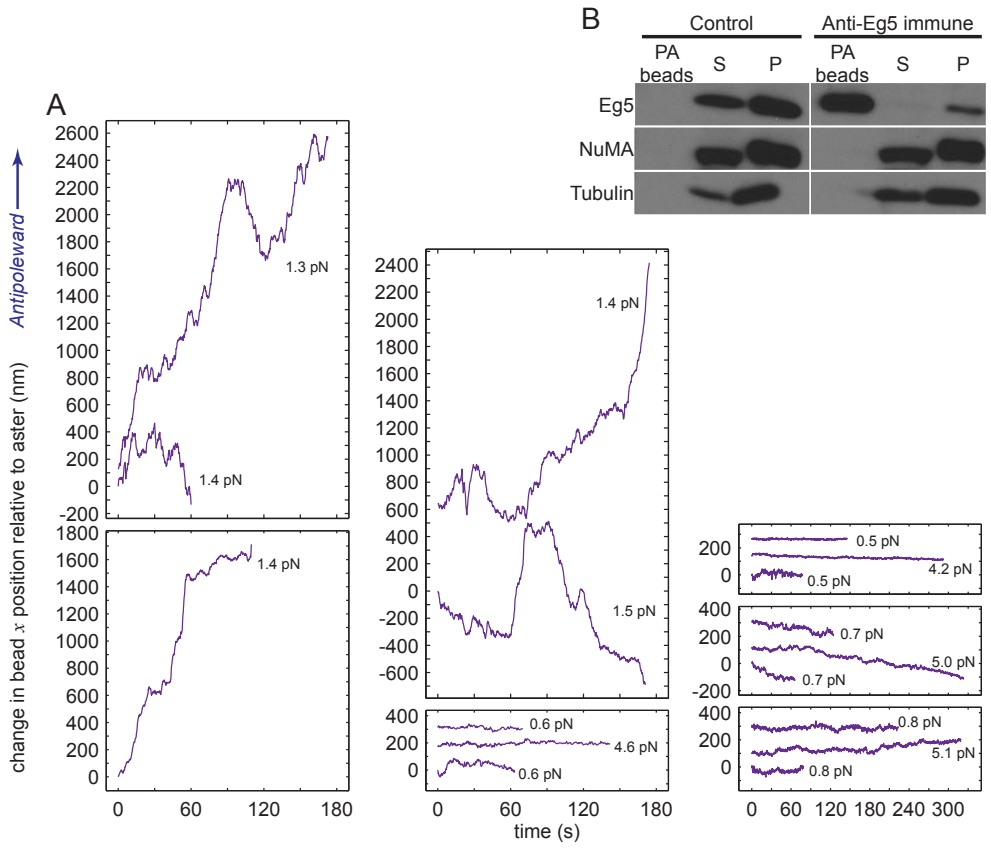

Figure A.3: Position *vs.* time traces for Eg5 depletion and assessment of Eg5 depletion. (A) Eg5 depletion plots formatted as Fig. A.2. (B) Immunoblot analysis of Eg5 in cell extracts. Following depletion of the extract, beads were recovered and the extract was separated into 10,000 g soluble (S) and insoluble (P) fractions after the induction of microtubule polymerization. PA beads refers to Protein-A agarose beads. These fractions were subjected to immunoblot analysis using antibodies against NuMA, Eg5 and tubulin as shown.

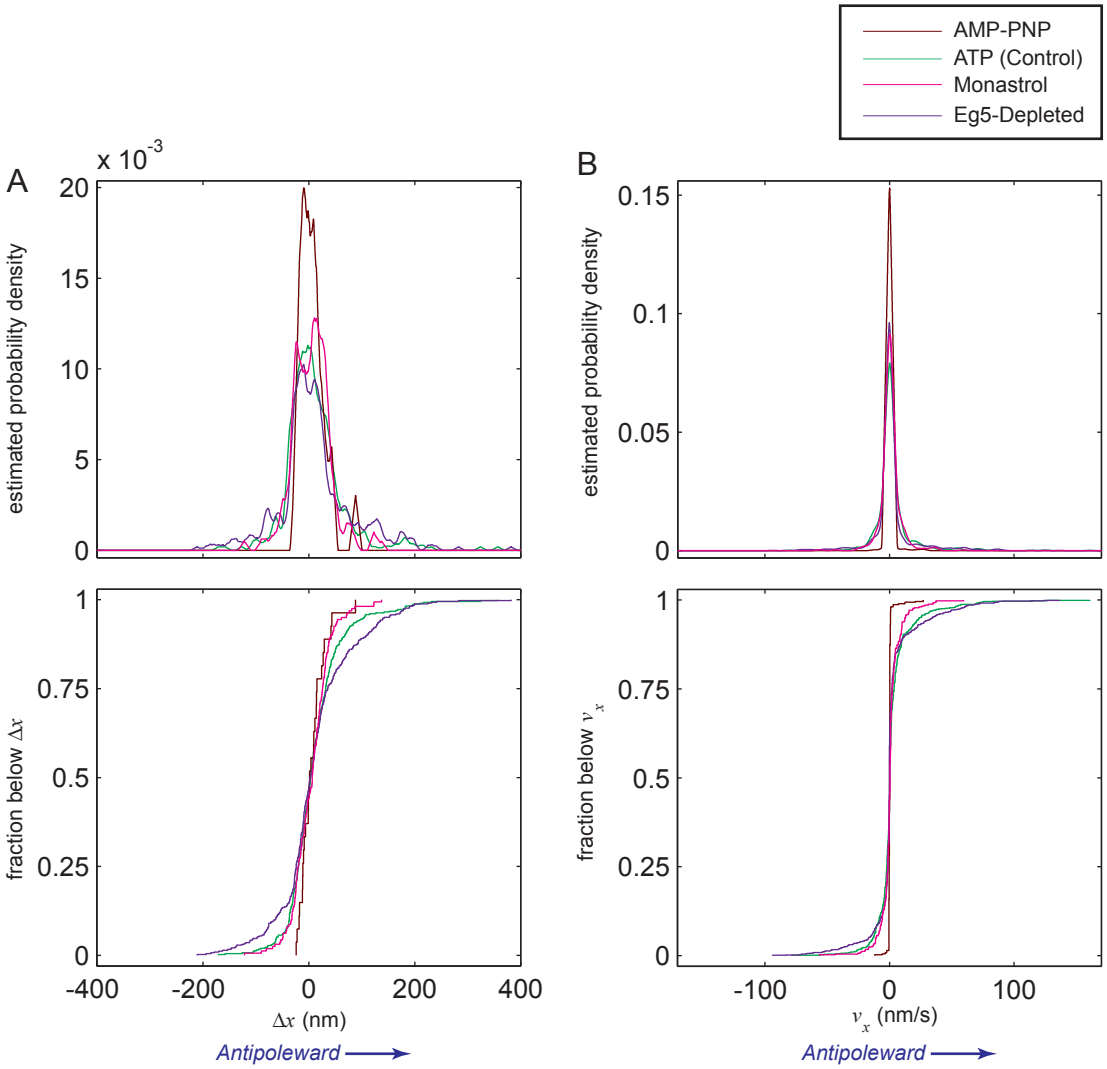

Figure A.4: Estimated Δx and v_x distributions. Estimated probability density (upper) and cumulative distribution (lower) functions for (A) Δx and (B) time-weighted v_x. For estimated probability density, the MATLAB ksdensity function was used with the triangle kernel and with width 2.5 nm/s for v_x and 5 nm for Δx.

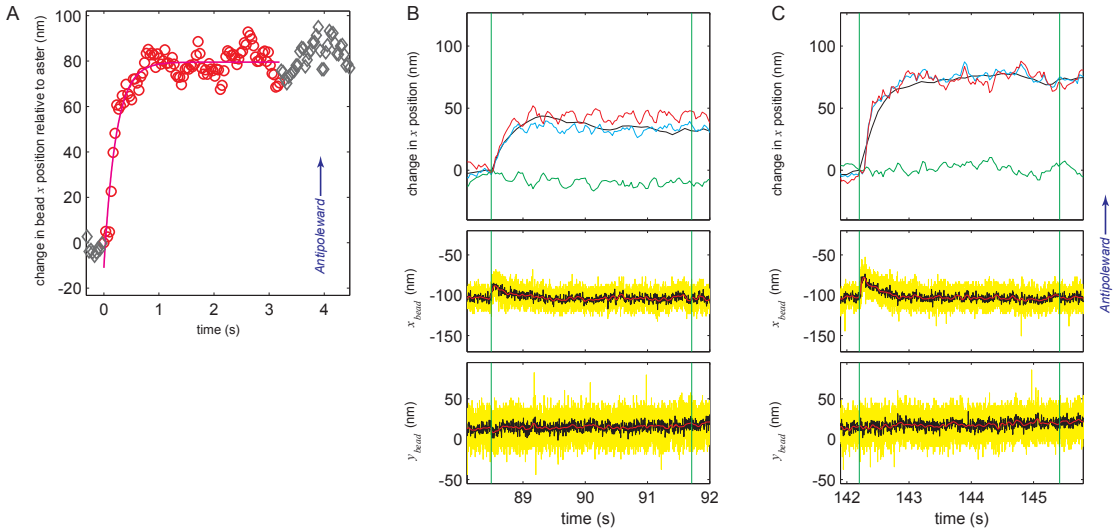

Figure A.5: Additional exponential jump data. (A) Second exponential jump observed in the AMP-PNP recording. Fit formatted as Fig. 3B showing the second jump of microtubule position in a pole in AMP-PNP. (B-C) Force clamp performance during exponential jumps. (B) Plots formatted as Fig. 1C-D but for the time interval used for the exponential fit of Fig. 3B. In the upper panels, each trace is shifted vertically such that they pass through the same point at the beginning of the interval. The aster (green) moves little. The middle plot (xbead vs. time) shows that the force clamp initially does not maintain constant force, with a 16.5-nm jump at 88.6 s. This had a small effect on the applied force and did not affect the measurement of changes in bead position relative to the aster. To minimize phase distortion in the filtered traces, forwardbackward filtering was used (MATLAB filtfilt function). (C) As (B), but corresponding to Figure S2A and with a 24.5-nm jump at 142.3 s.

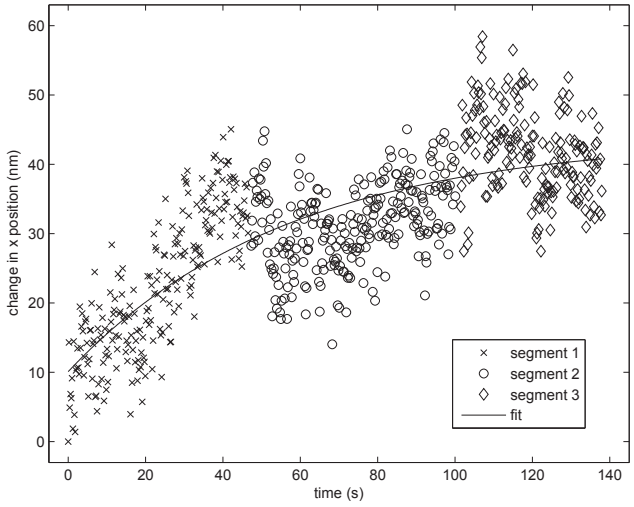

Figure A.6: Exponential fit to joined segments between jumps. From the trace in which the jumps occurred, segments (1, 2, 3) between jumps were extracted and aligned by forcing the x position at the end of one segment to match the mean of the first two points in the next segment. Selection of segment start and end points was arbitrary. The resulting curve was fit to an exponential representing another viscoelastic element in series with those that broke. This fit yielded values $\kappa_{\mathrm{a}} = 0.062 \pm 0.002$ pN nm^{-1} and $\gamma = 3.5 \pm 0.3$ pN s nm^{-1}.

APPENDIX B

The Hill 2D model

Further to section 4.3.1.2 (p. 64), this appendix summarizes, for a simple case, the 2D model of Hill [1986] and describes some of its implications. For reference, Table B.1 summarizes some of the key adaptations of Hill's nomenclature. Several symbols (e.g., v_g, $k_{on,MT}$) defined in Table 4.2 (p. 62) are used.

Table B.1: Comparison of Hill's nomenclature and that of the present work

Hill	Present work	Relationship
c	[Tub]	equal
s	N_{PF}	equal
w_h	$\Delta G_{Lateral}$	equal
i	j	equal
m_i	L_j	equal (Hill set the minimum L_j to 0, which is not explicit below)
α, β	$k_{on,PF}$, $k^{(1)}_{off,PF}$	similar depending on assumptions
x	Γ	$x = \Gamma^{-1}$
$a_{\lambda\nu}, b_{\nu\lambda}$	$\gamma_{off,q}$	similar?

Hill used $\Delta G_{Longitudinal}$ and $\Delta G_{Lateral}$, neglecting the entropic penalty of subunit immobilization, presumably implicitly recognizing that, as done by VanBuren, the penalty can be incorporated into the longitudinal term when considering subunit exchange at the tip. VanBuren used free energies under standard conditions (see erratum accompanying VanBuren et al. [2002]), but implicitly $\Delta G_{Lateral} = \Delta G^0_{Lateral}$.

We follow very closely the treatment of Hill [1986]. Early material provides some of the basis for the model of VanBuren et al. [2002] used in Chapter VI. Much of the remainder is a quantitative discussion of the fact that mean dissociation rate depends on tip structure, and tip structure depends on [Tub], so that dissociation rate depends on [Tub]. Chapter VI addresses whether these dependencies are of practical significance.

B.1 Surface free energy and roughness at equilibrium

Consider a hypothetical simplified N_{PF}-protofilament microtubule lattice, such as the that of Fig. B.1, in which the helix pitch is reduced to zero (a zero-start helix). If the bulk of the lattice had a vacant site, addition of a subunit at this position from infinity would involve a free energy change

$$\Delta G_{\mathrm{subunit}} = (2\Delta G_{\mathrm{Lateral}} + 2\Delta G_{\mathrm{Longitudinal}} + \Delta G_{\mathrm{Immobilization}}) \tag{B.1}$$

where these terms are, respectively, due to the two lateral interactions, two longitudinal interactions, and entropic penalty of immobilization. $\Delta G_{\mathrm{subunit}} < 0$.

If the microtubule were broken in two, the free energy change per newly formed end would be

$$\Delta G_{\mathrm{break}} = \left(-\frac{N_{\mathrm{PF}}}{2}\Delta G_{\mathrm{Longitudinal}} - m\Delta G_{\mathrm{Lateral}}\right) \tag{B.2}$$

where m, which Hill termed "an index of molecular roughness," is half the number of lateral interactions lost as a result of the breakage. m is only half of the lost interactions because the interaction energy is divided between the two subunits that lost the interaction. $\Delta G_{\mathrm{break}} > 0$ is the free surface energy. In equation B.2, the term $-\frac{N_{\mathrm{PF}}}{2}\Delta G_{\mathrm{Longitudinal}}$ is the same for any break. Fluctuations (due to subunit exchange) in the surface free energy of a microtubule tip are therefore independent of $\Delta G_{\mathrm{Longitudinal}}$. A subunit that associates with the tip may increase or decrease the

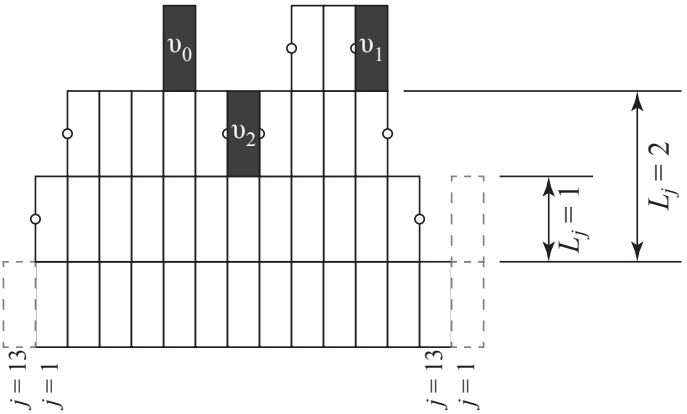

Figure B.1: Examples of subunit-addition transitions and definition of L_j. L_j, which appears in the expression for Hill's index of molecular roughness (equation B.3), is the length of protofilament j measured, in this case, relative to the shortest protofilaments (e.g., $L_1 = L_6 = 1$). Further to equation B.6, the state λ, shown as light subunits, could, by addition of 1 subunit (dark), undergo one of several $\lambda \to \nu_q$ transitions, of which 3 are shown. Circles and semi-circles indicate contributions to m_λ. Semi-circles indicate lost contributions. Gained contributions are not marked. This figure is based on Hill [1986].

number of lateral bonds available at the tip, but it creates a new longitidinal bond site that replaces the one it takes up.

m can be defined algebraically, letting the end of protofilament j be at a distance L_j along the microtubule measured in units of subunit length (Fig. B.1):

$$2m = |L_{N_{\mathrm{PF}}} - L_1| + \sum_{j=2}^{N_{\mathrm{PF}}} |L_j - L_{j-1}| \tag{B.3}$$

At the critical concentration, there is equilibrium between the microtubule and the free subunits. The microtubule tip "...will pass, stochastically, through (in principle) an infinite number of discrete surface structures [tip structures], each with a definite value of m..." [Hill, 1986] as determined by the Boltzmann distribution, so that the probability of a tip structure with m is proportional to $e^{m\Delta G_{\mathrm{Lateral}}/k_{\mathrm{B}}T}$, with larger m having lower weight and corresponding to a rougher tip. The distribution of m at $[\mathrm{Tub}] = C_{\mathrm{c}}$ depends entirely on lattice geometry and $\Delta G_{\mathrm{Lateral}}/k_{\mathrm{B}}T$.

B.2 Minimizing surface roughness

It would useful determine a value of $\Delta G_{\mathrm{Lateral}}$ that would result in predominantly low-roughness tips (as would be the case with helical/cozy-corner growth in the 3-start 13-protofilament lattice not considered here). Letting the degeneracy be $R(m)$ (the number of structures with m), the equilibrium probability, $P(\tilde{m})$, that $m = \tilde{m}$ is

$$P(\tilde{m}) = \frac{R(\tilde{m})\, e^{\tilde{m}\Delta G_{\mathrm{Lateral}}/k_{\mathrm{B}}T}}{\sum_m R(m)\, e^{m\Delta G_{\mathrm{Lateral}}/k_{\mathrm{B}}T}} \tag{B.4}$$

$$= \frac{R(\tilde{m})}{\sum_m R(m)\, e^{(m-\tilde{m})\Delta G_{\mathrm{Lateral}}/k_{\mathrm{B}}T}} \tag{B.5}$$

One would expect that for the lowest value of m to dominate would require

$$\Delta G_{\mathrm{Lateral}}/k_{\mathrm{B}}T \ll -1,$$

even ignoring the fact that the degeneracy of structures with the lowest m is relatively low. Away from equilibrium, this would presumably become more extreme. Hill [1986] computed mean m as a function of $\Delta G_{\mathrm{Lateral}}/k_{\mathrm{B}}T$ for several simple lattices that differ markedly from microtubules (small number of protofilaments, large stagger for lattice with largest number of protofilaments), finding perhaps $\Delta G_{\mathrm{Lateral}}/k_{\mathrm{B}}T < -3$ resulted in small mean m, but presumably a more realistic lattice would require a more extreme $\Delta G_{\mathrm{Lateral}}$ to force mean m to approach minimum m. Presumably computer enumeration of tip structures (following Hill) for a reasonable range of protofilament lengths would allow approximate evaluation of equation B.5 for limited N_{PF} and m.

B.3 Rate constants for a specific transition

Obtaining overall rate constants requires the consideration of transitions between the above-mentioned surface structures. Consider the association of one subunit to

the tip (Fig. B.1). Let the states of the tip before and after association be, respectively, λ and ν_q. As implicit in Fig. B.1, q is the number of lateral interactions made by the newly added subunit. For most states λ, there are multiple states ν_q for each value of q. The reaction is

$$\mathrm{MT}_{\lambda} + \mathrm{Tub} \underset{k_{\mathrm{off}}^{\lambda \leftarrow \nu_q}}{\overset{k_{\mathrm{on}}^{\lambda \rightarrow \nu_q}}{\rightleftharpoons}} \mathrm{MT}_{\nu_q} \tag{B.6}$$

where the rate constants marked are per-protofilament.

If states λ and ν_q have surface roughness indices m_λ and m_{ν_q}, the change in surface free energy is, from equation B.2,

$$\Delta G^{\lambda \rightarrow \nu_q} = (m_\lambda - m_\nu)\, \Delta G_{\mathrm{Lateral}} \tag{B.7}$$

$$\Delta G^{\lambda \rightarrow \nu_0} = -\Delta G_{\mathrm{Lateral}} > 0 \tag{B.8}$$

$$\Delta G^{\lambda \rightarrow \nu_1} = 0 \tag{B.9}$$

$$\Delta G^{\lambda \rightarrow \nu_2} = +\Delta G_{\mathrm{Lateral}} < 0. \tag{B.10}$$

Letting the equilibrium probability of states λ and ν_q be p_λ^{e} and $p_{\nu_q}^{\mathrm{e}}$, the ratio of probabilities for the two states is

$$\frac{p_{\nu_q}^{\mathrm{e}}}{p_\lambda^{\mathrm{e}}} = e^{-\Delta G^{\lambda \rightarrow \nu_q}/k_{\mathrm{B}}T} \tag{B.11}$$

The rates at which transitions occur is proportional to the probabilities of the states from which they occur. Invoking detailed balance,

$$k_{\mathrm{on}}^{\lambda \rightarrow \nu_q} C_{\mathrm{c}} p_\lambda^{\mathrm{e}} = k_{\mathrm{off}}^{\lambda \leftarrow \nu_q} p_{\nu_q}^{\mathrm{e}}. \tag{B.12}$$

Combining equations B.11 and B.12,

$$k_{\mathrm{on}}^{\lambda \rightarrow \nu_q} C_{\mathrm{c}} = k_{\mathrm{off}}^{\lambda \leftarrow \nu_q} e^{-\Delta G^{\lambda \rightarrow \nu_q}/k_{\mathrm{B}}T}. \tag{B.13}$$

For $q = 1$, equation B.9 yields

$$k_{\text{on}}^{\lambda\rightarrow\nu_1} C_{\text{c}} = k_{\text{off}}^{\lambda\leftarrow\nu_1} \tag{B.14}$$

For reasons described in section B.5 (p. 155), we assume association rate is independent of the number of neighbors,

$$k_{\text{on}}^{\lambda\rightarrow\nu_q} = k_{\text{on,PF}} \ \forall q, \tag{B.15}$$

and we make the change in notation $k_{\text{off}}^{\lambda\leftarrow\nu_q} \equiv k_{\text{off,PF}}^{(q)}$. Equation B.13 gives

$$k_{\text{off,PF}}^{(q)} = k_{\text{off,PF}}^{(1)} \left(e^{\Delta G^{\lambda\rightarrow\nu_q}/k_{\text{B}}T} \right) \tag{B.16}$$

which, combined with equation B.7, gives

$$k_{\text{off,PF}}^{(0)} = k_{\text{off,PF}}^{(1)} e^{-\Delta G_{\text{Lateral}}/k_{\text{B}}T} \tag{B.17}$$

$$k_{\text{off,PF}}^{(2)} = k_{\text{off,PF}}^{(1)} e^{\Delta G_{\text{Lateral}}/k_{\text{B}}T}. \tag{B.18}$$

The change in off rate with addition of a lateral interaction, $k_{\text{off,PF}}^{(q)}/k_{\text{off,PF}}^{(q+1)}$ ($q = 0$ or $q = 1$) is extremely sensitive to

$$\Gamma \equiv e^{-\Delta G_{\text{Lateral}}/k_{\text{B}}T} = \frac{k_{\text{off,PF}}^{(q)}}{k_{\text{off,PF}}^{(q+1)}}, q \in \{0, 1\}. \tag{B.19}$$

and may therefore be extremely sensitive to changes in temperature and $\Delta G_{\text{Lateral}}$.

B.4 Overall rate constants

To obtain the overall rate constants at equilibrium or steady state ([Tub] $\neq C_c$), consider the reaction of p. 152 but with ν_q replaced by a general state η:

$$\mathrm{MT}_\lambda + \mathrm{Tub} \rightleftharpoons \mathrm{MT}_\eta$$

For a given λ, each of the N_{PF} states η belongs to $\{\nu_0, \nu_1, \nu_2\}$ and corresponds to a subunit at the end of one of the N_{PF} protofilaments. η can be thought of as an index over the N_{PF} tip vacancies of λ, but also the η are states from which λ can be produced by subunit dissociation.

In a population of tips, the rate of $\lambda \leftarrow \eta$ transitions per instance of η is $k_{\mathrm{off}}^{\lambda\leftarrow\eta}$. Let η occur in this population with probability p_η. Consider one state λ and its corresponding η states, of which there are N_{PF}. The rate at which transitions to λ occur by dissociation is

$$\sum_\eta k_{\mathrm{off}}^{\lambda\leftarrow\eta} p_\eta,$$

where the sum is over the the N_{PF} η states. This is a rate per microtubule tip in the population. Taking into account all λ, the overall off rate per protofilament is

$$k_{\mathrm{off,PF}} = \frac{1}{N_{\mathrm{PF}}} \sum_\lambda \sum_\eta k_{\mathrm{off}}^{\lambda\leftarrow\eta} p_\eta. \tag{B.20}$$

The sum can be expanded and grouped into factors of $k_{\mathrm{off,PF}}^{(0)}$, $k_{\mathrm{off,PF}}^{(1)}$, and $k_{\mathrm{off,PF}}^{(2)}$, corresponding to equation 6.5 (p. 102).

Hill [1986] went on to conclude that, in general, neither the rate of subunit association nor the rate of subunit dissociation is necessarily expected to be proportional to [Tub]. Each rate (arguably only the dissociation rate) may be affected by changes in tip structure with [Tub], which appear as changes in the probabilities in equation B.20.

B.5 Aside: Rate perturbation factors

The assumption used in equation B.15 (p. 153) is important in that it may have a large effect on the rate constants, but it is not central to this appendix.

For $q \neq 1$, we define rate perturbation factors γ:

$$k_{\text{on}}^{\lambda \to \nu_q} \equiv \gamma_{\text{on},q} k_{\text{on}}^{\lambda \to \nu_1} \tag{B.21}$$

$$k_{\text{off}}^{\lambda \leftarrow \nu_q} \equiv \gamma_{\text{off},q} k_{\text{off}}^{\lambda \leftarrow \nu_1} \tag{B.22}$$

Equation B.13 becomes

$$\gamma_{\text{on},q} k_{\text{on}}^{\lambda \to \nu_1} C_{\text{c}} = \gamma_{\text{off},q} k_{\text{off}}^{\lambda \leftarrow \nu_1} e^{-\Delta G^{\lambda \to \nu_q}} \tag{B.23}$$

and, applying equation B.14, we have

$$\gamma_{\text{on},q} = \gamma_{\text{off},q} e^{-\Delta G^{\lambda \to \nu_q}}. \tag{B.24}$$

This implies that there are infinite ways that the $q \neq 1$ rate constants can be perturbed relative to $q = 1$. For instance, for $\lambda \to \nu_2$ transitions the association of subunits might be slowed by a steric barrier presented by the two neighbors already present. This same barrier would also reduce the off rate. Both these effects would be reflected in the $\gamma_{\text{on},2}$ and $\gamma_{\text{off},2}$. Hill noted that the "most realistic assumption is probably" $\gamma_{\text{off},q} = 1$, corresponding to diffusion-limited association events such that "the full effect of [the change in surface free energy] is felt by the off rate constants (neighbor interactions must be broken for a subunit to escape)." [Hill, 1986].

For a vacancy with two lateral neighbors, one could argue that the association rate should be lower due to steric limitations on accessibility of the vacancy by diffusion. Considering the geometry of the microtubule and the putative localization of binding surface area toward the lumen, it seems possible that subunits encountering

the tip might have a reduced probability, in terms of the description of Northrup and Erickson [1992], to achieve a nearly-correct orientation corresponding to a partial bond formation that stabilizes the subunit, making full bond formation likely. On the other hand, with 3 binding surfaces, the subunit might be more likely to form one of these partial bonds. Also, considering the possibility of A- and B-type joins, one might postulate that the subunit has an additional binding site roughly 4 nm away from the vacancy in which weak lateral interactions might stabilize the correct orientation of the subunit, and upon dissociation from this site it might diffuse to the correct location faster than its rotational diffusion would cause misorientation, forming a longitudinal bond in addition to lateral bonds.

BIBLIOGRAPHY

BIBLIOGRAPHY

B. Akiyoshi, K. K. Sarangapani, A. F. Powers, C. R. Nelson, S. L. Reichow, H. Arellano-Santoyo, T. Gonen, J. A. Ranish, C. L. Asbury, and S. Biggins. Tension directly stabilizes reconstituted kinetochore-microtubule attachments. *Nature*, 468(7323):576–579, Nov 2010. doi: 10.1038/nature09594. URL `http://dx.doi.org/10.1038/nature09594`. 19, 20

J. Al-Bassam, H. Kim, G. Brouhard, A. van Oijen, S. C. Harrison, and F. Chang. Clasp promotes microtubule rescue by recruiting tubulin dimers to the microtubule. *Dev Cell*, 19(2):245–258, Aug 2010. doi: 10.1016/j.devcel.2010.07.016. URL `http://dx.doi.org/10.1016/j.devcel.2010.07.016`. 49

L. A. Amos. Microtubule structure and its stabilisation. *Org Biomol Chem*, 2(15): 2153–2160, Aug 2004. doi: 10.1039/b403634d. URL `http://dx.doi.org/10.1039/b403634d`. 2, 50, 51, 71

L. A. Amos and D. Schlieper. Microtubules and maps. *Adv Protein Chem*, 71:257–298, 2005. doi: 10.1016/S0065-3233(04)71007-4. URL `http://dx.doi.org/10.1016/S0065-3233(04)71007-4`. 2, 48

I. Arnal, E. Karsenti, and A. Hyman. Structural transitions at microtubule ends correlate with their dynamic properties in xenopus egg extracts. *Journal of Cell Biology*, 149(4):767–774, 2000. 57, 58, 59, 61, 132

C. Asbury, D. Gestaut, A. Powers, A. Franck, and T. Davis. The dam1 kinetochore complex harnesses microtubule dynamics to produce force and movement. *Proceedings of the National Academy of Sciences of the United States of America*, 103(26): 9873–9878, 2006. 76

N. A. Baker, D. Sept, S. Joseph, M. J. Holst, and J. A. McCammon. Electrostatics of nanosystems: application to microtubules and the ribosome. *Proc Natl Acad Sci U S A*, 98(18):10037–10041, Aug 2001. doi: 10.1073/pnas.181342398. URL `http://dx.doi.org/10.1073/pnas.181342398`. 52

S. F. Bakhoum, G. Genovese, and D. A. Compton. Deviant kinetochore microtubule dynamics underlie chromosomal instability. *Curr Biol*, 19(22):1937–1942, Dec 2009a. doi: 10.1016/j.cub.2009.09.055. URL `http://dx.doi.org/10.1016/j.cub.2009.09.055`. 125

S. F. Bakhoum, S. L. Thompson, A. L. Manning, and D. A. Compton. Genome stability is ensured by temporal control of kinetochore-microtubule dynamics. *Nat Cell Biol*, 11(1):27–35, Jan 2009b. doi: 10.1038/ncb1809. URL `http://dx.doi.org/10.1038/ncb1809`. 125

R. Basto, J. Lau, T. Vinogradova, A. Gardiol, C. Woods, A. Khodjakov, and J. Raff. Flies without centrioles. *Cell*, 125(7):1375–1386, 2006. 15

D. Begg and G. Ellis. Micromanipulation studies of chromosome movement .2. birefringent chromosomal fibers and the mechanical attachment of chromosomes to the spindle. *Journal of Cell Biology*, 82(2):542–554, 1979a. 17

D. Begg and G. Ellis. Micromanipulation studies of chromosome movement .1. chromosome-spindle attachment and the mechanical-properties of chromosomal spindle fibers. *Journal of Cell Biology*, 82(2):528–541, 1979b. 17

L. Bergen and G. Borisy. Head-to-tail polymerization of microtubules invitro - electron-microscope analysis of seeded assembly. *Journal of Cell Biology*, 84(1): 141–150, 1980. 91

A. D. Bicek, E. Tüzel, A. Demtchouk, M. Uppalapati, W. O. Hancock, D. M. Kroll, and D. J. Odde. Anterograde microtubule transport drives microtubule bending in llc-pk1 epithelial cells. *Mol Biol Cell*, 20(12):2943–2953, Jun 2009. doi: 10.1091/mbc.E08-09-0909. URL `http://dx.doi.org/10.1091/mbc.E08-09-0909`. 95, 115

P. Bieling, L. Laan, H. Schek, E. Munteanu, L. Sandblad, M. Dogterom, D. Brunner, and T. Surrey. Reconstitution of a microtubule plus-end tracking system in vitro. *Nature*, 450(7172):1100–1105, 2007. 76

P. Bieling, I. Kronja, and T. Surrey. Microtubule motility on reconstituted meiotic chromatin. *Curr Biol*, 20(8):763–769, Apr 2010. doi: 10.1016/j.cub.2010.02.067. URL `http://dx.doi.org/10.1016/j.cub.2010.02.067`. 21

V. Bormuth, V. Varga, J. Howard, and E. Schaffer. Protein friction limits diffusive and directed movements of kinesin motors on microtubules. *Science*, 325(5942): 870–873, 2009. 41

G. Brouhard and A. Hunt. Microtubule movements on the arms of mitotic chromosomes: Polar ejection forces quantified in vitro. *Proceedings of the National Academy of Sciences of the United States of America*, 102(39):13903–13908, 2005. 20

G. Brouhard, H. Schek, and A. Hunt. Advanced optical tweezers for the study of cellular and molecular biomechanics. *Ieee Transactions on Biomedical Engineering*, 50(1):121–125, 2003. 26, 81

G. Brouhard, J. Stear, T. Noetzel, J. Al Bassam, K. Kinoshita, S. Harrison, J. Howard, and A. Hyman. XMAP215 is a processive microtubule polymerase. *Cell*, 132(1):79–88, 2008. 52, 70, 76, 91, 95, 124, 127

L. Cameron, G. Yang, D. Cimini, J. Canman, O. Evgenieva, A. Khodjakov, G. Danuser, and E. Salmon. Kinesin 5-independent poleward flux of kinetochore microtubules in ptk1 cells. *Journal of Cell Biology*, 173(2):173–179, 2006. 39

M. J. Cannon, A. D. Williams, R. Wetzel, and D. G. Myszka. Kinetic analysis of beta-amyloid fibril elongation. *Anal Biochem*, 328(1):67–75, May 2004. doi: 10.1016/j.ab.2004.01.014. URL `http://dx.doi.org/10.1016/j.ab.2004.01.014`. 127

M. Caplow and J. Shanks. Evidence that a single monolayer tubulin-gtp cap is both necessary and sufficient to stabilize microtubules. *Mol Biol Cell*, 7(4):663–675, Apr 1996. 72, 133

M. Carlier and D. Pantaloni. Kinetic-analysis of cooperativity in tubulin polymerization in presence of guanosine diphosphate or triphosphate nucleotides. *Biochemistry*, 17(10):1908–1915, 1978. 88

M. F. Carlier, T. L. Hill, and Y. Chen. Interference of gtp hydrolysis in the mechanism of microtubule assembly: an experimental study. *Proc Natl Acad Sci U S A*, 81(3):771–775, Feb 1984. 91

L. Cassimeris, N. K. Pryer, and E. D. Salmon. Real-time observations of microtubule dynamic instability in living cells. *J Cell Biol*, 107(6 Pt 1):2223–2231, Dec 1988. 124

A. Chakravarty, L. Howard, and D. Compton. A mechanistic model for the organization of microtubule asters by motor and non-motor proteins in a mammalian mitotic extract. *Molecular Biology of the Cell*, 15(5):2116–2132, 2004. 22, 23, 130

M. Chalfie and J. N. Thomson. Structural and functional diversity in the neuronal microtubules of caenorhabditis elegans. *J Cell Biol*, 93(1):15–23, Apr 1982. 55

R. Chambers. Some physical properties of the cell nucleus. *Science*, 40:824–827, 1914. 16

B. Charlebois, H. Schek, and A. Hunt. Nanometer-resolution microtubule polymerization assays using optical tweezers and microfabricated barriers. In J. Correia, editor, *Methods in Cell Biology*, number 12, pages 203–215. 2010. 26, 48, 75

B. D. Charlebois, S. Kollu, H. T. Schek, III, D. A. Compton, and A. J. Hunt. Spindle pole mechanics studied in mitotic asters: Dynamic distribution of spindle forces through compliant linkages. *Biophysical Journal*, 100(7):1756–1764, APR 6 2011. doi: 10.1016/j.bpj.2011.02.017. 11, 24

S. Charrasse, M. Schroeder, C. Gauthier-Rouviere, F. Ango, L. Cassimeris, D. L. Gard, and C. Larroque. The togp protein is a new human microtubule-associated protein homologous to the xenopus xmap215. *J Cell Sci*, 111 (Pt 10):1371–1383, May 1998. 124

I. M. Cheeseman and A. Desai. Molecular architecture of the kinetochore-microtubule interface. *Nat Rev Mol Cell Biol*, 9(1):33–46, Jan 2008. doi: 10.1038/nrm2310. URL http://dx.doi.org/10.1038/nrm2310. 13, 14, 20

I. M. Cheeseman, J. S. Chappie, E. M. Wilson-Kubalek, and A. Desai. The conserved kmn network constitutes the core microtubule-binding site of the kinetochore. *Cell*, 127(5):983–997, Dec 2006. doi: 10.1016/j.cell.2006.09.039. URL http://dx.doi.org/10.1016/j.cell.2006.09.039. 20

W. Chen and D. Zhang. Kinetochore fibre dynamics outside the context of the spindle during anaphase. *Nature Cell Biology*, 6(3):227–231, 2004. 46

Y. D. Chen and T. L. Hill. Monte carlo study of the gtp cap in a five-start helix model of a microtubule. *Proc Natl Acad Sci U S A*, 82(4):1131–1135, Feb 1985. 68

C. Choudhary, C. Kumar, F. Gnad, M. L. Nielsen, M. Rehman, T. C. Walther, J. V. Olsen, and M. Mann. Lysine acetylation targets protein complexes and co-regulates major cellular functions. *Science*, 325(5942):834–840, Aug 2009. doi: 10.1126/science.1175371. URL http://dx.doi.org/10.1126/science.1175371. 52

D. Chrétien and S. D. Fuller. Microtubules switch occasionally into unfavorable configurations during elongation. *J Mol Biol*, 298(4):663–676, May 2000. doi: 10.1006/jmbi.2000.3696. URL http://dx.doi.org/10.1006/jmbi.2000.3696. 55

D. Chrétien and R. Wade. New data on the microtubule surface lattice. *Biology of the Cell*, 71(1-2):161–174, 1991. 54, 55

D. Chrétien, F. Metoz, F. Verde, E. Karsenti, and R. H. Wade. Lattice defects in microtubules: protofilament numbers vary within individual microtubules. *J Cell Biol*, 117(5):1031–1040, Jun 1992. 122

D. Chrétien, S. Fuller, and E. Karsenti. Structure of growing microtubule ends - 2-dimensional sheets close into tubes at variable rates. *Journal of Cell Biology*, 129 (5):1311–1328, 1995. 9, 58, 59, 66, 76, 91, 113, 122, 132

J. Cochran, J. Gatial, T. Kapoor, and S. Gilbert. Monastrol inhibition of the mitotic kinesin Eg5. *Journal of Biological Chemistry*, 280(13):12658–12667, 2005. 42

S. R. Collins, A. Douglass, R. D. Vale, and J. S. Weissman. Mechanism of prion propagation: amyloid growth occurs by monomer addition. *PLoS Biol*, 2(10):e321, Oct 2004. doi: 10.1371/journal.pbio.0020321. URL http://dx.doi.org/10.1371/journal.pbio.0020321. 127

D. Compton. Focusing on spindle poles. *Journal of Cell Science*, 111:1477–1481, 1998. 15, 16, 22

L. J. Davis, D. J. Odde, S. M. Block, and S. P. Gross. The importance of lattice defects in katanin-mediated microtubule severing in vitro. *Biophys J*, 82(6):2916–2927, Jun 2002. doi: 10.1016/S0006-3495(02)75632-4. URL `http://dx.doi.org/10.1016/S0006-3495(02)75632-4`. 122

A. Demtchouk, M. Gardner, and D. Odde. Microtubule tip tracking and tip structures at the nanometer scale using digital fluorescence microscopy. *Cellular and Molecular Bioengineering*, 2011. 94, 95, 114, 117, 120, 124

A. Desai and T. Mitchison. Microtubule polymerization dynamics. *Annual Review of Cell and Developmental Biology*, 13:83–117, 1997. 2, 7, 53, 54

A. Dimitrov, M. Quesnoit, S. Moutel, I. Cantaloube, C. Poüs, and F. Perez. Detection of gtp-tubulin conformation in vivo reveals a role for gtp remnants in microtubule rescues. *Science*, 322(5906):1353–1356, Nov 2008. doi: 10.1126/science.1165401. URL `http://dx.doi.org/10.1126/science.1165401`. 74

M. Dionne, L. Howard, and D. Compton. Numa is a component of an insoluble matrix at mitotic spindle poles. *Cell Motility and the Cytoskeleton*, 42(3):189–203, 1999. 22, 23

C. G. dos Remedios, D. Chhabra, M. Kekic, I. V. Dedova, M. Tsubakihara, D. A. Berry, and N. J. Nosworthy. Actin binding proteins: regulation of cytoskeletal microfilaments. *Physiol Rev*, 83(2):433–473, Apr 2003. doi: 10.1152/physrev.00026.2002. URL `http://dx.doi.org/10.1152/physrev.00026.2002`. 57

D. N. Drechsel and M. W. Kirschner. The minimum gtp cap required to stabilize microtubules. *Curr Biol*, 4(12):1053–1061, Dec 1994. 72

D. N. Drechsel, A. A. Hyman, M. H. Cobb, and M. W. Kirschner. Modulation of the dynamic instability of tubulin assembly by the microtubule-associated protein tau. *Mol Biol Cell*, 3(10):1141–1154, Oct 1992. 49, 91, 125, 131

S. Dumont and T. Mitchison. Compression regulates mitotic spindle length by a mechanochemical switch at the poles. *Current Biology*, 19(13):1086–1095, 2009. 18

R. Dye and R. Williams. Assembly of microtubules from tubulin bearing the nonhydrolyzable guanosine triphosphate analogue GMPPCP [Guanylyl 5'-(beta,gamma-methylenediphosphonate)]: Variability of growth rates and the hydrolysis of GTP. *Biochemistry*, 35(45):14331–14339, 1996. 71, 76, 86, 105, 120

C. Elie-Caille, F. Severin, J. Helenius, J. Howard, D. J. Muller, and A. A. Hyman. Straight gdp-tubulin protofilaments form in the presence of taxol. *Curr Biol*, 17(20):1765–1770, Oct 2007. doi: 10.1016/j.cub.2007.08.063. URL `http://dx.doi.org/10.1016/j.cub.2007.08.063`. 58, 122

Y. Engelborghs, L. C. D. Maeyer, and N. Overbergh. A kinetic analysis of the assembly of microtubules in vitro. *FEBS Lett*, 80(1):81–85, Aug 1977. 91

K. Farrell and M. Jordan. A kinetic-analysis of assembly-disassembly at opposite microtubule ends. *Journal of Biological Chemistry*, 257(6):3131–3138, 1982. 91

K. Farrell, M. Jordan, H. Miller, and L. Wilson. Phase dynamics at microtubule ends - the coexistence of microtubule length changes and treadmilling. *Journal of Cell Biology*, 104(4):1035–1046, 1987. 83

H. Felgner, R. Frank, and M. Schliwa. Flexural rigidity of microtubules measured with the use of optical tweezers. *Journal of Cell Science*, 109:509–516, 1996. 36

N. P. Ferenz, A. Gable, and P. Wadsworth. Mitotic functions of kinesin-5. *Semin Cell Dev Biol*, 21(3):255–259, May 2010. doi: 10.1016/j.semcdb.2010.01.019. URL `http://dx.doi.org/10.1016/j.semcdb.2010.01.019`. 14

J. Finer, R. Simmons, and J. Spudich. Single myosin molecule mechanics - piconewton forces and nanometer steps. *Nature*, 368(6467):113–119, 1994. 85

D. Fygenson, H. Flyvbjerg, K. Sneppen, A. Libchaber, and S. Leibler. Spontaneous nucleation of microtubules. *Physical Review e*, 51(5):5058–5063, 1995. 88

S. Gadde and R. Heald. Mechanisms and molecules of the mitotic spindle. *Current Biology*, 14(18):R797–R805, 2004. 15, 16

T. Gaglio, A. Saredi, and D. Compton. NuMA is required for the organization of microtubules into aster-like mitotic arrays. *Journal of Cell Biology*, 131(3):693–708, 1995. 22, 25, 29, 138

T. Gaglio, A. Saredi, J. Bingham, M. Hasbani, S. Gill, T. Schroer, and D. Compton. Opposing motor activities are required for the organization of the mammalian mitotic spindle pole. *Journal of Cell Biology*, 135(2):399–414, 1996. 22, 25, 29, 36, 41, 138

T. Gaglio, M. Dionne, and D. Compton. Mitotic spindle poles are organized by structural and motor proteins in addition to centrosomes. *Journal of Cell Biology*, 138(5):1055–1066, 1997. 23, 29, 36, 138

D. L. Gard and M. W. Kirschner. A microtubule-associated protein from xenopus eggs that specifically promotes assembly at the plus-end. *J Cell Biol*, 105(5):2203–2215, Nov 1987. 91

M. Gardner, A. Hunt, H. Goodson, and D. Odde. Microtubule assembly dynamics: new insights at the nanoscale. *Current Opinion in Cell Biology*, 20(1):64–70, 2008a. 76

M. Gardner, B. Charlebois, I. Jánosi, J. Howard, A. Hunt, and D. Odde. Fluctuations in growth rate support a 2D model for microtubule self-assembly kinetics. *Cell*, 2011. 48, 90, 100, 115, 117

M. K. Gardner, D. C. Bouck, L. V. Paliulis, J. B. Meehl, E. T. O'Toole, J. Haase, A. Soubry, A. P. Joglekar, M. Winey, E. D. Salmon, K. Bloom, and D. J. Odde. Chromosome congression by kinesin-5 motor-mediated disassembly of longer kinetochore microtubules. *Cell*, 135(5):894–906, Nov 2008b. doi: 10.1016/j.cell.2008.09.046. URL `http://dx.doi.org/10.1016/j.cell.2008.09.046`. 125

J. Gatlin, A. Matov, G. Danuser, T. Mitchison, and E. Salmon. Directly probing the mechanical properties of the spindle and its matrix. *Journal of Cell Biology*, 188 (4):481–489, 2010. 17, 21, 46

J. C. Gatlin and K. Bloom. Microtubule motors in eukaryotic spindle assembly and maintenance. *Semin Cell Dev Biol*, 21(3):248–254, May 2010. doi: 10.1016/j.semcdb.2010.01.015. URL `http://dx.doi.org/10.1016/j.semcdb.2010.01.015`. 14

C. Gell, V. Bormuth, G. J. Brouhard, D. N. Cohen, S. Diez, C. T. Friel, J. Helenius, B. Nitzsche, H. Petzold, J. Ribbe, E. Schäffer, J. H. Stear, A. Trushko, V. Varga, P. O. Widlund, M. Zanic, and J. Howard. Microtubule dynamics reconstituted in vitro and imaged by single-molecule fluorescence microscopy. *Methods Cell Biol*, 95:221–245, 2010. doi: 10.1016/S0091-679X(10)95013-9. URL `http://dx.doi.org/10.1016/S0091-679X(10)95013-9`. 93, 128, 133

R. Gildersleeve, A. Cross, K. Cullen, A. Fagen, and R. Williams. Microtubules grow and shorten at intrinsically variable rates. *Journal of Biological Chemistry*, 267 (12):7995–8006, 1992. 71, 76, 120

F. Gittes and C. Schmidt. Signals and noise in micromechanical measurements. In M. Sheetz, editor, *Methods in cell biology*, number 55, pages 129–156. 1998a. 82, 85, 86, 87

F. Gittes and C. Schmidt. Interference model for back-focal-plane displacement detection in optical tweezers. *Optics Letters*, 23(1):7–9, 1998b. 81, 85

F. Gittes, B. Mickey, J. Nettleton, and J. Howard. Flexural rigidity of microtubules and actin-filaments measured from thermal fluctuations in shape. *Journal of Cell Biology*, 120(4):923–934, 1993. 36, 82

M. Gordon, L. Howard, and D. Compton. Chromosome movement in mitosis requires microtubule anchorage at spindle poles. *Journal of Cell Biology*, 152(3):425–434, 2001. 21

E. Grishchuk, M. Molodtsov, F. Ataullakhanov, and J. McIntosh. Force production by disassembling microtubules. *Nature*, 438(7066):384–388, 2005. 6, 76

K. Gupta, B. Paulson, E. Folker, B. Charlebois, A. Hunt, and H. Goodson. Minimal plus-end tracking unit of the cytoplasmic linker protein clip-170. *Journal of Biological Chemistry*, 284(11):6735–6742, 2009. 88

F. Gustafsson. Determining the initial states in forward-backward filtering. *Ieee Transactions on Signal Processing*, 44(4):988–992, 1996. 86

J. Happel and H. Brenner. *Low Reynolds Number Hydrodynamics: With Special Applications to Particulate Media*, volume 1. Kluwer, The Hague, Boston, Hingham Massachusetts, 1983. 40

J. Helenius, G. Brouhard, Y. Kalaidzidis, S. Diez, and J. Howard. The depolymerizing kinesin MCAK uses lattice diffusion to rapidly target microtubule ends. *Nature*, 441(7089):115–119, 2006. 52, 76

C. Hentrich and T. Surrey. Microtubule organization by the antagonistic mitotic motors kinesin-5 and kinesin-14. *Journal of Cell Biology*, 189(3):465–480, May 2010. 21, 130

H. Herrmann, H. Bär, L. Kreplak, S. V. Strelkov, and U. Aebi. Intermediate filaments: from cell architecture to nanomechanics. *Nat Rev Mol Cell Biol*, 8(7):562–573, Jul 2007. doi: 10.1038/nrm2197. URL `http://dx.doi.org/10.1038/nrm2197`. 2, 3

K. M. Hertzer and C. E. Walczak. The c-termini of tubulin and the specific geometry of tubulin substrates influence the depolymerization activity of mcak. *Cell Cycle*, 7(17):2727–2737, Sep 2008. 52

J. Höög, S. Huisman, Z. Sebo-Lemke, L. Sandblad, J. McIntosh, C. Antony, and D. Brunner. Electron tomography reveals a flared morphology on growing microtubule ends. *Journal of Cell Science*, 124(5):693–698, 2011. 57, 58, 59, 132

T. Hill. Theoretical problems related to the attachment of microtubules to kinetochores. *Proceedings of the National Academy of Sciences of the United States of America*, 82(13):4404–4408, 1985. 15

T. Hill. *Linear Aggregation Theory in Cell Biology*. Springer-Verlag, 1987. 64, 65

T. L. Hill. Effect of fluctuating surface structure and free energy on the growth of linear tubular aggregates. *Biophysical Journal*, 49(5):1017–1031, May 1986. doi: 10.1016/S0006-3495(86)83730-4. URL `http://dx.doi.org/10.1016/S0006-3495(86)83730-4`. 9, 64, 65, 67, 71, 90, 91, 104, 148, 149, 150, 151, 154, 155

T. Holy and S. Leibler. Dynamic instability of microtubules as an efficient way to search in-space. *Proceedings of the National Academy of Sciences of the United States of America*, 91(12):5682–5685, 1994. 15

T. Horio and H. Hotani. Visualization of the dynamic instability of individual microtubules by dark-field microscopy. *Nature*, 321(6070):605–607, 1986. 76

J. Howard. *Mechanics of Motor Proteins and the Cytoskeleton*. Sinauer Associates, Inc., Sunderland, Massachusetts, 2001. 1, 2, 40, 53, 54, 55, 57, 73, 132

J. Howard and A. Hyman. Dynamics and mechanics of the microtubule plus end. *Nature*, 422(6933):753–758, 2003. 2, 6

J. Howard and A. Hyman. Growth, fluctuation and switching at microtubule plus ends. *Nature Reviews Molecular Cell Biology*, 10(8):569–574, 2009. 2, 9, 63, 71, 86, 120

J. Howard and A. A. Hyman. Microtubule polymerases and depolymerases. *Current Opinion in Cell Biology*, 19(1):31–35, Feb. 2007. 7, 48

B. Howell, N. Larsson, M. Gullberg, and L. Cassimeris. Dissociation of the tubulin-sequestering and microtubule catastrophe-promoting activities of oncoprotein 18/stathmin. *Mol Biol Cell*, 10(1):105–118, Jan 1999. 49

A. Hunt and J. McIntosh. The dynamic behavior of individual microtubules associated with chromosomes in vitro. *Molecular Biology of the Cell*, 9(10):2857–2871, 1998. 19

A. W. Hunter, M. Caplow, D. L. Coy, W. O. Hancock, S. Diez, L. Wordeman, and J. Howard. The kinesin-related protein MCAK is a microtubule depolymerase that forms an atp-hydrolyzing complex at microtubule ends. *Molecular Cell*, 11(2): 445–457, Feb. 2003. 125

A. Hyman, S. Salser, D. Drechsel, N. Unwin, and T. Mitchison. Role of GTP hydrolysis in microtubule dynamics - information from a slowly hydrolyzable analog, gmpcpp. *Molecular Biology of the Cell*, 3(10):1155–1167, 1992. 83, 88, 91

T. Itabashi, J. Takagi, Y. Shimamoto, H. Onoe, K. Kuwana, I. Shimoyama, J. Gaetz, T. Kapoor, and S. Ishiwata. Probing the mechanical architecture of the vertebrate meiotic spindle. *Nature Methods*, 6(2):167–172, 2009. 18, 21, 38

C. Janke, K. Rogowski, and J. van Dijk. Polyglutamylation: a fine-regulator of protein function? 'protein modifications: beyond the usual suspects' review series. *EMBO Rep*, 9(7):636–641, Jul 2008. doi: 10.1038/embor.2008.114. URL `http://dx.doi.org/10.1038/embor.2008.114`. 52

D. Job, O. Valiron, and B. Oakley. Microtubule nucleation. *Current Opinion in Cell Biology*, 15(1):111–117, 2003. 88

A. P. Joglekar, K. Bloom, and E. D. Salmon. In vivo protein architecture of the eukaryotic kinetochore with nanometer scale accuracy. *Curr Biol*, 19(8):694–699, Apr 2009. doi: 10.1016/j.cub.2009.02.056. URL `http://dx.doi.org/10.1016/j.cub.2009.02.056`. 20

M. Jordan and L. Wilson. Microtubules as a target for anticancer drugs. *Nature Reviews Cancer*, 4(4):253–265, 2004. 49, 131

M. Jordan, R. Toso, D. Thrower, and L. Wilson. Mechanism of mitotic block and inhibition of cell-proliferation by taxol at low concentrations. *Proceedings of the National Academy of Sciences of the United States of America*, 90(20):9552–9556, 1993. 76

E. Karsenti and I. Vernos. Cell cycle - the mitotic spindle: A self-made machine. *Science*, 294(5542):543–547, 2001. 21

J. Kerssemakers, E. Munteanu, L. Laan, T. Noetzel, M. Janson, and M. Dogterom. Assembly dynamics of microtubules at molecular resolution. *Nature*, 442(7103): 709–712, 2006. 70, 72, 76, 77, 80, 85, 97, 120, 122

I. Khan and R. Luduena. Possible regulation of the invitro assembly of bovine brain tubulin by the bovine thioredoxin system. *Biochimica et Biophysica Acta*, 1076(2): 289–297, 1991. 81

A. Khodjakov, L. Copenagle, M. Gordon, D. Compton, and T. Kapoor. Minus-end capture of preformed kinetochore fibers contributes to spindle morphogenesis. *Journal of Cell Biology*, 160(5):671–683, 2003. 15

M. Kikumoto, M. Kurachi, V. Tosa, and H. Tashiro. Flexural rigidity of individual microtubules measured by a buckling force with optical traps. *Biophysical Journal*, 90(5):1687–1696, 2006. 82

K. Kinoshita, I. Arnal, A. Desai, D. N. Drechsel, and A. A. Hyman. Reconstitution of physiological microtubule dynamics using purified components. *Science*, 294(5545): 1340–1343, Nov 2001. doi: 10.1126/science.1064629. URL `http://dx.doi.org/10.1126/science.1064629`. 49

M. Kirschner and T. Mitchison. Beyond self-assembly - from microtubules to morphogenesis. *Cell*, 45(3):329–342, 1986. 15

M. Korneev, S. Lakamper, and C. Schmidt. Load-dependent release limits the processive stepping of the tetrameric Eg5. *European biophysics journal*, 36(6):675–681, 2007. 43

H. Y. Kueh and T. J. Mitchison. Structural plasticity in actin and tubulin polymer dynamics. *Science*, 325(5943):960–963, Aug 2009. doi: 10.1126/science.1168823. URL `http://dx.doi.org/10.1126/science.1168823`. 74

M. Kurachi, M. Hoshi, and H. Tashiro. Buckling of a single microtubule by optical trapping forces - direct measurement of microtubule rigidity. *Cell Motility and the Cytoskeleton*, 30(3):221–228, 1995. 82

B. Kwok, L. Kapitein, J. Kim, E. Peterman, C. Schmidt, and T. Kapoor. Allosteric inhibition of kinesin-5 modulates its processive directional motility. *Nature Chemical Biology*, 2(9):480–485, 2006. 42

S. Lakämper and E. Meyhöfer. The e-hook of tubulin interacts with kinesin's head to increase processivity and speed. *Biophys J*, 89(5):3223–3234, Nov 2005. doi: 10.1529/biophysj.104.057505. URL http://dx.doi.org/10.1529/biophysj.104.057505. 52

H. Li, D. DeRosier, W. Nicholson, E. Nogales, and K. Downing. Microtubule structure at 8 angstrom resolution. *Structure*, 10(10):1317–1328, 2002. 50, 52, 53

H. Lodish, A. Berk, P. Matsudaira, C. Kaiser, M. Krieger, M. Scott, S. Zipursky, and J. Darnell. *Molecular Cell Biology*, volume 5. W. H. Freeman and Company, New York, 2004. 1, 2, 5, 7, 12

R. Loughlin, B. Riggs, and R. Heald. Snapshot: motor proteins in spindle assembly. *Cell*, 134(3):548–548.e1, Aug 2008. doi: 10.1016/j.cell.2008.07.038. URL http://dx.doi.org/10.1016/j.cell.2008.07.038. 13

J. Lowe, H. Li, K. Downing, and E. Nogales. Refined structure of alpha beta-tubulin at 3.5 a resolution. *Journal of Molecular Biology*, 313(5):1045–1057, 2001. 50, 53, 67

L. A. Lowery and D. V. Vactor. The trip of the tip: understanding the growth cone machinery. *Nat Rev Mol Cell Biol*, 10(5):332–343, May 2009. doi: 10.1038/nrm2679. URL http://dx.doi.org/10.1038/nrm2679. 4

H. Maiato, C. Rieder, and A. Khodjakov. Kinetochore-driven formation of kinetochore fibers contributes to spindle assembly during animal mitosis. *Journal of Cell Biology*, 167(5):831–840, 2004. 15

E. Mandelkow, E. Mandelkow, and R. Milligan. Microtubule dynamics and microtubule caps - a time-resolved cryoelectron microscopy study. *Journal of Cell Biology*, 114(5):977–991, 1991. 57, 58, 59

D. Mastronarde, K. Mcdonald, R. Ding, and J. McIntosh. Interpolar spindle microtubules in ptk cells. *Journal of Cell Biology*, 123(6):1475–1489, 1993. 21

I. Matos, A. Pereira, M. Lince-Faria, L. Cameron, E. Salmon, and H. Maiato. Synchronizing chromosome segregation by flux-dependent force equalization at kinetochores. *Journal of Cell Biology*, 186(1):11–26, 2009. 44

R. Melki, I. Vainberg, R. Chow, and N. Cowan. Chaperonin-mediated folding of vertebrate actin-related protein and gamma-tubulin. *Journal of Cell Biology*, 122 (6):1301–1310, 1993. 83

A. Merdes, K. Ramyar, J. Vechio, and D. Cleveland. A complex of numa and cytoplasmic dynein is essential for mitotic spindle assembly. *Cell*, 87(3):447–458, 1996. 22

B. Mickey and J. Howard. Rigidity of microtubules is increased by stabilizing agents. *Journal of Cell Biology*, 130(4):909–917, 1995. 36, 81

H. Miki, Y. Okada, and N. Hirokawa. Analysis of the kinesin superfamily: insights into structure and function. *Trends in Cell Biology*, 15(9):467–476, 2005. 7

L. A. Mirny and D. J. Needleman. Quantitative characterization of filament dynamics by single-molecule lifetime measurements. *Methods Cell Biol*, 95:583–600, 2010. doi: 10.1016/S0091-679X(10)95029-2. URL `http://dx.doi.org/10.1016/S0091-679X(10)95029-2`. 70, 111, 133

T. Mitchison. Polewards microtubule flux in the mitotic spindle - evidence from photoactivation of fluorescence. *Journal of Cell Biology*, 109(2):637–652, 1989. 13

T. Mitchison and M. Kirschner. Dynamic instability of microtubule growth. *Nature*, 312(5991):237–242, 1984. 7, 8, 91

T. Mitchison, P. Maddox, J. Gaetz, A. Groen, M. Shirasu, A. Desai, E. Salmon, and T. Kapoor. Roles of polymerization dynamics, opposed motors, and a tensile element in governing the length of xenopus extract meiotic spindles. *Molecular Biology of the Cell*, 16(6):3064–3076, 2005. 42

T. J. Mitchison and M. W. Kirschner. Some thoughts on the partitioning of tubulin between monomer and polymer under conditions of dynamic instability. *Cell Biophys*, 11:35–55, Dec 1987. 126

A. Mitra and D. Sept. Taxol allosterically alters the dynamics of the tubulin dimer and increases the flexibility of microtubules. *Biophys J*, 95(7):3252–3258, Oct 2008. doi: 10.1529/biophysj.108.133884. URL `http://dx.doi.org/10.1529/biophysj.108.133884`. 53, 131

T. Müller-Reichert, D. Chrétien, F. Severin, and A. A. Hyman. Structural changes at microtubule ends accompanying gtp hydrolysis: information from a slowly hydrolyzable analogue of gtp, guanylyl (alpha,beta)methylenediphosphonate. *Proc Natl Acad Sci U S A*, 95(7):3661–3666, Mar 1998. 57

J. Moffitt, Y. Chemla, S. Smith, and C. Bustamante. Recent advances in optical tweezers. *Annual Review of Biochemistry*, 77:205–228, 2008. 87

A. Mogilner and E. Craig. Towards a quantitative understanding of mitotic spindle assembly and mechanics. *Journal of Cell Science*, 123(20):3435–3445, 2010. 14, 21

J. K. Moore and J. A. Cooper. Coordinating mitosis with cell polarity: Molecular motors at the cell cortex. *Semin Cell Dev Biol*, 21(3):283–289, May 2010. doi: 10.1016/j.semcdb.2010.01.020. URL `http://dx.doi.org/10.1016/j.semcdb.2010.01.020`. 14

C. Moores, M. Perderiset, C. Kappeler, S. Kain, D. Drummond, S. Perkins, J. Chelly, R. Cross, A. Houdusse, and F. Francis. Distinct roles of doublecortin modulating the microtubule cytoskeleton. *Embo Journal*, 25(19):4448–4457, 2006. 49, 76, 88, 131

V. Mountain, C. Simerly, L. Howard, A. Ando, G. Schatten, and D. Compton. The kinesin-related protein, HSET, opposes the activity of Eg5 and cross-links microtubules in the mammalian mitotic spindle. *Journal of Cell Biology*, 147(2):351–365, 1999. 22, 23, 29, 36, 138

D. B. Murphy, K. A. Johnson, and G. G. Borisy. Role of tubulin-associated proteins in microtubule nucleation and elongation. *J Mol Biol*, 117(1):33–52, Nov 1977. 127

D. J. Needleman, A. Groen, R. Ohi, T. Maresca, L. Mirny, and T. Mitchison. Fast microtubule dynamics in meiotic spindles measured by single molecule imaging: evidence that the spindle environment does not stabilize microtubules. *Mol Biol Cell*, 21(2):323–333, Jan 2010. doi: 10.1091/mbc.E09-09-0816. URL `http://dx.doi.org/10.1091/mbc.E09-09-0816`. 70, 133

R. Nicklas. Measurements of the force produced by the mitotic spindle in anaphase. *Journal of Cell Biology*, 97(2):542–548, 1983. 19, 46

R. Nicklas and C. Staehly. Chromosome micromanipulation I: Mechanics of chromosome attachment to spindle. *Chromosoma*, 21(1):1–16, 1967. 16

R. Nicklas, D. Kubai, and T. Hays. Spindle microtubules and their mechanical associations after micromanipulation in anaphase. *Journal of Cell Biology*, 95(1):91–104, 1982. 21

E. Nogales and H. Wang. Structural intermediates in microtubule assembly and disassembly: how and why? *Current Opinion in Cell Biology*, 18(2):179–184, 2006. 50, 57

E. Nogales, S. Wolf, and K. Downing. Structure of the alpha beta tubulin dimer by electron crystallography (vol 391, pg 199, 1998). *Nature*, 393(6681):191–191, 1998. 50

E. Nogales, M. Whittaker, R. Milligan, and K. Downing. High-resolution model of the microtubule. *Cell*, 96(1):79–88, 1999. 52

E. Nogales, H. Wang, and H. Niederstrasser. Tubulin rings: which way do they curve? *Current Opinion in Structural Biology*, 13(2):256–261, 2003. 57

S. H. Northrup and H. P. Erickson. Kinetics of protein-protein association explained by brownian dynamics computer simulation. *Proc Natl Acad Sci U S A*, 89(8): 3338–3342, Apr 1992. 70, 108, 126, 156

E. T. O'Brien, E. D. Salmon, R. A. Walker, and H. P. Erickson. Effects of magnesium on the dynamic instability of individual microtubules. *Biochemistry*, 29(28):6648–6656, Jul 1990. 49, 91

E. T. O'Brien, E. D. Salmon, and H. P. Erickson. How calcium causes microtubule depolymerization. *Cell Motil Cytoskeleton*, 36(2):125–135, 1997. doi: 3.0.CO;2-8. URL `http://dx.doi.org/3.0.CO;2-8`. 49

C. O'Connell and A. Khodjakov. Cooperative mechanisms of mitotic spindle formation. *Journal of Cell Science*, 120(10):1717–1722, 2007. 15, 16

D. Odde, L. Cassimeris, and H. Buettner. Kinetics of microtubule catastrophe assessed by probabilistic analysis. *Biophysical Journal*, 69(3):796–802, 1995. 49, 72, 132

D. Odde, H. Buettner, and L. Cassimeris. Spectral analysis of microtubule assembly dynamics. *Aiche Journal*, 42(5):1434–1442, 1996. 76, 86, 87, 120

T. Ohba, M. Nakamura, H. Nishitani, and T. Nishimoto. Self-organization of microtubule asters induced in xenopus egg extracts by gtp-bound ran. *Science*, 284 (5418):1356–1358, May 1999. 130

F. Oosawa. Size distribution of protein polymers. *Journal of Theoretical Biology*, 27 (1):69–&, 1970. 61, 63, 86, 90, 92, 111, 118

C. G. Pearson and M. Winey. Basal body assembly in ciliates: the power of numbers. *Traffic*, 10(5):461–471, May 2009. doi: 10.1111/j.1600-0854.2009.00885.x. URL `http://dx.doi.org/10.1111/j.1600-0854.2009.00885.x`. 2

C. G. Pearson, M. K. Gardner, L. V. Paliulis, E. D. Salmon, D. J. Odde, and K. Bloom. Measuring nanometer scale gradients in spindle microtubule dynamics using model convolution microscopy. *Mol Biol Cell*, 17(9):4069–4079, Sep 2006. doi: 10.1091/mbc.E06-04-0312. URL `http://dx.doi.org/10.1091/mbc.E06-04-0312`. 95

S. Pedigo and R. Williams. Concentration dependence of variability in growth rates of microtubules. *Biophysical Journal*, 83(4):1809–1819, 2002. 71, 76, 86, 120

M. Poirier, S. Eroglu, and J. Marko. The bending rigidity of mitotic chromosomes. *Molecular Biology of the Cell*, 13(6):2170–2179, 2002. 18, 38

T. D. Pollard. Rate constants for the reactions of atp- and adp-actin with the ends of actin filaments. *J Cell Biol*, 103(6 Pt 2):2747–2754, Dec 1986. 108

A. Powers, A. Franck, D. Gestaut, J. Cooper, B. Gracyzk, R. Wei, L. Wordeman, T. Davis, and C. Asbury. The ndc80 kinetochore complex forms load-bearing attachments to dynamic microtubule tips via biased diffusion. *Cell*, 136(5):865–875, 2009. 19, 20

N. K. Pryer, R. A. Walker, V. P. Skeen, B. D. Bourns, M. F. Soboeiro, and E. D. Salmon. Brain microtubule-associated proteins modulate microtubule dynamic instability in vitro. real-time observations using video microscopy. *J Cell Sci*, 103 (Pt 4):965–976, Dec 1992. 124, 125, 127

R. B. G. Ravelli, B. Gigant, P. A. Curmi, I. Jourdain, S. Lachkar, A. Sobel, and M. Knossow. Insight into tubulin regulation from a complex with colchicine and a stathmin-like domain. *Nature*, 428(6979):198–202, Mar 2004. doi: 10.1038/nature02393. URL `http://dx.doi.org/10.1038/nature02393`. 50

S. Ray, E. Meyhöfer, R. Milligan, and J. Howard. Kinesin follows the microtubules protofilament axis. *Journal of Cell Biology*, 121(5):1083–1093, 1993. 54, 55

V. Rezania, O. Azarenko, M. A. Jordan, H. Bolterauer, R. F. Ludueña, J. T. Huzil, and J. A. Tuszynski. Microtubule assembly of isotypically purified tubulin and its mixtures. *Biophys J*, 95(4):1993–2008, Aug 2008. doi: 10.1529/biophysj.108.132233. URL `http://dx.doi.org/10.1529/biophysj.108.132233`. 121

C. Rieder. Kinetochore fiber formation in animal somatic cells: dueling mechanisms come to a draw. *Chromosoma*, 114(5):310–318, 2005. 16

M. Rief, M. Gautel, F. Oesterhelt, J. Fernandez, and H. Gaub. Reversible unfolding of individual titin immunoglobulin domains by AFM. *Science*, 276(5315):1109–1112, 1997. 38

A. Roll-Mecak and F. J. McNally. Microtubule-severing enzymes. *Curr Opin Cell Biol*, 22(1):96–103, Feb 2010. doi: 10.1016/j.ceb.2009.11.001. URL `http://dx.doi.org/10.1016/j.ceb.2009.11.001`. 57

N. M. Rusan, C. J. Fagerstrom, A. M. Yvon, and P. Wadsworth. Cell cycle-dependent changes in microtubule dynamics in living cells expressing green fluorescent protein-alpha tubulin. *Mol Biol Cell*, 12(4):971–980, Apr 2001. 124

I. Sandoval and K. Weber. Guanosine 5'-(alpha,beta-methylene)triphosphate enhances specifically microtubule nucleation and stops the treadmill of tubulin protomers. *Journal of Biological Chemistry*, 255(14):6966–6974, 1980. 88

A. Saredi, L. Howard, and D. Compton. NuMA assembles into an extensive filamentous structure when expressed in the cell cytoplasm. *Journal of Cell Science*, 109: 619–630, 1996. 43

K. Sawin, K. Leguellec, M. Philippe, and T. Mitchison. Mitotic spindle organization by a plus-end-directed microtubule motor. *Nature*, 359(6395):540–543, 1992. 41

H. Schek and A. Hunt. Micropatterned structures for studying the mechanics of biological polymers. *Biomedical Microdevices*, 7(1):41–46, 2005. 77, 78, 82

H. Schek and A. Hunt. Optical tweezers. In J. Webster, editor, *Encyclopedia of Medical Devices and Instrumentation, Volume 5*, volume 2, pages 175–187. John Wiley & Sons, Hoboken, New Jersey, 2006. 81

H. Schek, M. Gardner, J. Cheng, D. Odde, and A. Hunt. Microtubule assembly dynamics at the nanoscale. *Current Biology*, 17(17):1445–1455, 2007. 26, 27, 69, 70, 72, 75, 76, 77, 78, 85, 87, 88, 89, 92, 96, 97, 103, 112, 114, 115, 116, 120, 122, 127, 128

P. Schiff, J. Fant, and S. Horwitz. Promotion of microtubule assembly invitro by taxol. *Nature*, 277(5698):665–667, 1979. 88

F. Schrader. *Mitosis: the movements of chromosomes in cell division.* Columbia University Press, 1953. 14

T. Schroer. Dynactin. *Annual Review of Cell and Developmental Biology*, 20:759–779, 2004. 7

D. Sept, N. A. Baker, and J. A. McCammon. The physical basis of microtubule structure and stability. *Protein Sci*, 12(10):2257–2261, Oct 2003. doi: 10.1110/ps.03187503. URL `http://dx.doi.org/10.1110/ps.03187503`. 53, 131

E. Shelden and P. Wadsworth. Observation and quantification of individual microtubule behavior in vivo: microtubule dynamics are cell-type specific. *J Cell Biol*, 120(4):935–945, Feb 1993. 117, 124

K. H. Siller and C. Q. Doe. Spindle orientation during asymmetric cell division. *Nat Cell Biol*, 11(4):365–374, Apr 2009. doi: 10.1038/ncb0409-365. URL `http://dx.doi.org/10.1038/ncb0409-365`. 14

J. G. Skellam. The frequency distribution of the difference between two poisson variates belonging to different populations. *J R Stat Soc Ser A*, 109(Pt 3):296, 1946. 111

R. Skibbens, V. Skeen, and E. Salmon. Directional instability of kinetochore motility during chromosome congression and segregation in mitotic newt lung-cells - a push-pull mechanism. *Journal of Cell Biology*, 122(4):859–875, 1993. 13

K. Slep and R. Vale. Structural basis of microtubule plus end tracking by xmap215, clip-170, and eb1. *Molecular Cell*, 27(6):976–991, 2007. 88

L. A. Stiffler, J. Y. Ji, S. Trautmann, C. Trusty, and G. Schubiger. Cyclin a and b functions in the early drosophila embryo. *Development*, 126(23):5505–5513, Dec 1999. 126

E. Stukalin and A. Kolomeisky. Simple growth models of rigid multifilament biopolymers. *Journal of Chemical Physics*, 121(2):1097–1104, 2004. 111

R. Subramanian, E. Wilson-Kubalek, C. Arthur, M. Bick, E. Campbell, S. Darst, R. Milligan, and T. Kapoor. Insights into antiparallel microtubule crosslinking by prc1, a conserved nonmotor microtubule binding protein. *Cell*, 142(3):433–443, 2010. 46

H. Sui and K. H. Downing. Structural basis of interprotofilament interaction and lateral deformation of microtubules. *Structure*, 18(8):1022–1031, Aug 2010. doi: 10.1016/j.str.2010.05.010. URL `http://dx.doi.org/10.1016/j.str.2010.05.010`. 52, 53, 54, 55, 56

T. Surrey, F. Nedelec, S. Leibler, and E. Karsenti. Physical properties determining self-organization of motors and microtubules. *Science*, 292(5519):1167–1171, 2001. 21, 130

K. Svoboda, C. Schmidt, B. Schnapp, and S. Block. Direct observation of kinesin stepping by optical trapping interferometry. *Nature*, 365(6448):721–727, 1993. 85, 87

K. Svoboda, P. Mitra, and S. Block. Fluctuation analysis of motor protein movement and single enzyme-kinetics. *Proceedings of the National Academy of Sciences of the United States of America*, 91(25):11782–11786, 1994. 87

L. Tao, A. Mogilner, G. Civelekogiu-Scholey, R. Wollman, J. Evans, H. Stahlberg, and J. Scholey. A homotetrameric kinesin-5, klp61f, bundles microtubles and antagonizes ncd in motility assays. *Current Biology*, 16(23):2293–2302, 2006. 36

M. Tirado and J. Garciadelatorre. Translational friction coefficients of rigid, symmetric top macromolecules - application to circular-cylinders. *Journal of Chemical Physics*, 71(6):2581–2587, 1979. 40

S. Toba, T. Watanabe, L. Yamaguchi-Okimoto, Y. Toyoshima, and H. Higuchi. Overlapping hand-over-hand mechanism of single molecular motility of cytoplasmic dynein. *Proceedings of the National Academy of Sciences of the United States of America*, 103(15):5741–5745, 2006. 33

B. Trinczek, A. Marx, E. M. Mandelkow, D. B. Murphy, and E. Mandelkow. Dynamics of microtubules from erythrocyte marginal bands. *Mol Biol Cell*, 4(3):323–335, Mar 1993. 91

J. Tuszynski, T. Luchko, S. Portet, and J. Dixon. Anisotropic elastic properties of microtubules. *European Physical Journal e*, 17(1):29–35, 2005. 36

M. Valentine, P. Fordyce, T. Krzysiak, S. Gilbert, and S. Block. Individual dimers of the mitotic kinesin motor Eg5 step processively and support substantial loads in vitro. *Nature Cell Biology*, 8(5):470–U89, 2006. 33, 43

O. Valiron, I. Arnal, N. Caudron, and D. Job. Gdp-tubulin incorporation into growing microtubules modulates polymer stability. *J Biol Chem*, 285(23):17507–17513, Jun 2010. doi: 10.1074/jbc.M109.099515. URL `http://dx.doi.org/10.1074/jbc.M109.099515`. 74

V. VanBuren, D. J. Odde, and L. Cassimeris. Estimates of lateral and longitudinal bond energies within the microtubule lattice. *Proc Natl Acad Sci U S A*, 99(9): 6035–6040, Apr 2002. doi: 10.1073/pnas.092504999. URL `http://dx.doi.org/10.1073/pnas.092504999`. 53, 67, 68, 69, 72, 90, 99, 122, 124, 127, 128, 148, 149

V. VanBuren, L. Cassimeris, and D. J. Odde. Mechanochemical model of microtubule structure and self-assembly kinetics. *Biophysical Journal*, 89(5):2911–2926, Nov 2005. doi: 10.1529/biophysj.105.060913. URL `http://dx.doi.org/10.1529/biophysj.105.060913`. 59, 69, 72, 127, 132

A. Vandecandelaere, S. R. Martin, and P. M. Bayley. Regulation of microtubule dynamic instability by tubulin-gdp. *Biochemistry*, 34(4):1332–1343, Jan 1995. 121

R. J. Vasquez, D. L. Gard, and L. Cassimeris. Xmap from xenopus eggs promotes rapid plus end assembly of microtubules and rapid microtubule polymer turnover. *J Cell Biol*, 127(4):985–993, Nov 1994. 124

C. Veigel, M. Bartoo, D. White, J. Sparrow, and J. Molloy. The stiffness of rabbit skeletal actomyosin cross-bridges determined with an optical tweezers transducer. *Biophysical Journal*, 75(3):1424–1438, 1998. 38

P. Venier, A. Maggs, M. Carlier, and D. Pantaloni. Analysis of microtubule rigidity using hydrodynamic flow and thermal fluctuations. *Journal of Biological Chemistry*, 269(18):13353–13360, 1994. 36

K. Visscher and S. Block. *Versatile optical traps with feedback control*. ACADEMIC PRESS INC, SAN DIEGO, 1998. 81, 85, 87

B. Vitre, F. Coquelle, C. Heichette, C. Garnier, D. Chretien, and I. Arnal. Eb1 regulates microtubule dynamics and tubulin sheet closure in vitro. *Nature Cell Biology*, 10(4):415–U81, 2008. 49, 55, 58, 59

W. Voter and H. Erickson. The kinetics of microtubule assembly - evidence for a 2-stage nucleation mechanism. *Journal of Biological Chemistry*, 259(16):430–438, 1984. 88

P. Wadsworth, A. Khodjakov, and scipline: Cell Biology. E pluribus unum: towards a universal mechanism for spindle assembly. *Trends in Cell Biology*, 14(8):413–419, 2004. 15, 16

C. E. Walczak, S. Cai, and A. Khodjakov. Mechanisms of chromosome behaviour during mitosis. *Nat Rev Mol Cell Biol*, 11(2):91–102, Feb 2010. doi: 10.1038/nrm2832. URL `http://dx.doi.org/10.1038/nrm2832`. 12, 13

R. Walker, E. Obrien, N. Pryer, M. Soboeiro, W. Voter, H. Erickson, and E. Salmon. Dynamic instability of individual microtubules analyzed by video light-microscopy - rate constants and transition frequencies. *Journal of Cell Biology*, 107(4):1437–1448, 1988. 76, 91, 126

X. Wan, R. P. O'Quinn, H. L. Pierce, A. P. Joglekar, W. E. Gall, J. G. DeLuca, C. W. Carroll, S.-T. Liu, T. J. Yen, B. F. McEwen, P. T. Stukenberg, A. Desai, and E. D. Salmon. Protein architecture of the human kinetochore microtubule attachment site. *Cell*, 137(4):672–684, May 2009. doi: 10.1016/j.cell.2009.03.035. URL `http://dx.doi.org/10.1016/j.cell.2009.03.035`. 95

C. Wang, A. Cormier, B. Gigant, and M. Knossow. Insight into the gtpase activity of tubulin from complexes with stathmin-like domains. *Biochemistry*, 46(37):10595–10602, Sep 2007. doi: 10.1021/bi701147f. URL `http://dx.doi.org/10.1021/bi701147f`. 73, 132

H. Wang and E. Nogales. Nucleotide-dependent bending flexibility of tubulin regulates microtubule assembly. *Nature*, 435(7044):911–915, 2005. 50, 58, 74

R. R. Wei, P. K. Sorger, and S. C. Harrison. Molecular organization of the ndc80 complex, an essential kinetochore component. *Proc Natl Acad Sci U S A*, 102(15): 5363–5367, Apr 2005. doi: 10.1073/pnas.0501168102. URL `http://dx.doi.org/10.1073/pnas.0501168102`. 20

S. Westermann and K. Weber. Post-translational modifications regulate microtubule function. *Nature Reviews Molecular Cell Biology*, 4(12):938–947, 2003. 52

R. Williams and L. Rone. End-to-end joining of taxol-stabilized gdp-containing microtubules. *Journal of Biological Chemistry*, 264(3):1663–1670, 1989. 83

M. Winey, C. L. Mamay, E. T. O'Toole, D. N. Mastronarde, T. H. Giddings, K. L. McDonald, and J. R. McIntosh. Three-dimensional ultrastructural analysis of the saccharomyces cerevisiae mitotic spindle. *J Cell Biol*, 129(6):1601–1615, Jun 1995. 125

R. Wollman, E. Cytrynbaum, J. Jones, T. Meyer, J. Scholey, and A. Mogilner. Efficient chromosome capture requires a bias in the 'search-and-capture' process during mitotic-spindle assembly. *Current Biology*, 15(9):828–832, 2005. 15

P. Yamauchi, G. Flynn, R. Marsh, and D. Purich. Reduction in microtubule dynamics invitro by brain microtubule-associated proteins and by a microtubule-associated protein-2 2nd repeated sequence analog. *Journal of Neurochemistry*, 60(3):817–826, 1993. 83

M. Yanagida. Clearing the way for mitosis: is cohesin a target? *Nat Rev Mol Cell Biol*, 10(7):489–496, Jul 2009. doi: 10.1038/nrm2712. URL `http://dx.doi.org/10.1038/nrm2712`. 12

C. Yuan, A. Chen, P. Kolb, and V. Moy. Energy landscape of streptavidin-biotin complexes measured by atomic force microscopy. *Biochemistry*, 39(33):10219–10223, August 2000. 38